Jordan Journal of Mechanical and Industrial Engineering (JJMIE)

JJMIE is a high-quality scientific journal devoted to fields of Mechanical and Industrial Engineering. It is published by The Jordanian Ministry of Higher Education and Scientific Research in corporation with the Hashemite University.

SUBMISSION ADDRESS:

Prof. **Mousa S. Mohsen**, Editor-in-Chief
Jordan Journal of Mechanical & Industrial Engineering,
Hashemite University, PO Box 330127, Zarqa, 13133 , Jordan
E-mail: jjmie@hu.edu.jo

Hashemite Kingdom of Jordan

Hashemite University

Jordan Journal of Mechanical and Industrial Engineering

JJMIE

An International Peer-Reviewed Scientific Journal

http://jjmie.hu.edu.jo/

ISSN 1995-6665

Jordan Journal of Mechanical and Industrial Engineering (JJMIE)

JJMIE is a high-quality scientific journal devoted to fields of Mechanical and Industrial Engineering. It is published by The Jordanian Ministry of Higher Education and Scientific Research in corporation with the Hashemite University.

Introduction: The Editorial Board is very committed to build the Journal as one of the leading international journals in mechanical and industrial engineering sciences in the next few years. With the support of the Ministry of Higher Education and Scientific Research and Jordanian Universities, it is expected that a heavy resource to be channeled into the Journal to establish its international reputation. The Journal's reputation will be enhanced from arrangements with several organizers of international conferences in publishing selected best papers of the conference proceedings.

Aims and Scope: Jordan Journal of Mechanical and Industrial Engineering (JJMIE) is a refereed international journal to be of interest and use to all those concerned with research in various fields of, or closely related to, mechanical and industrial engineering disciplines. Jordan Journal of Mechanical and Industrial Engineering aims to provide a highly readable and valuable addition to the literature which will serve as an indispensable reference tool for years to come. The coverage of the journal includes all new theoretical and experimental findings in the fields of mechanical and industrial engineering or any closely related fields. The journal also encourages the submission of critical review articles covering advances in recent research of such fields as well as technical notes.

Guide for Authors

Manuscript Submission

High-quality submissions to this new journal are welcome now and manuscripts may be either submitted online or mail.

Online: For online submission upload one copy of the full paper including graphics and all figures at the online submission site, accessed via E-mail: jjmie@hu.edu.jo. The manuscript must be written in MS Word Format. All correspondence, including notification of the Editor's decision and requests for revision, takes place by e-mail and via the Author's homepage, removing the need for a hard-copy paper trail.

By Mail: Manuscripts (1 original and 3 copies) accompanied by a covering letter may be sent to the Editor-in-Chief. However, a copy of the original manuscript, including original figures, and the electronic files should be sent to the Editor-in-Chief. Authors should also submit electronic files on disk (one disk for text material and a separate disk for graphics), retaining a backup copy for reference and safety.

Note that contributions may be either submitted online or sent by mail. Please do NOT submit via both routes. This will cause confusion and may lead to delay in article publication. Online submission is preferred.

Submission address and contact:

Prof. **Mousa S. Mohsen**, Editor-in-Chief
Jordan Journal of Mechanical & Industrial Engineering,
Hashemite University,
PO Box 330127, Zarqa, 13133 , Jordan
E-mail: jjmie@hu.edu.jo

Types of contributions: Original research papers

Corresponding author: Clearly indicate who is responsible for correspondence at all stages of refereeing and publication, including post-publication. Ensure that telephone and fax numbers (with country and area code) are provided in addition to the e-mail address and the complete postal address. Full postal addresses must be given for all co-authors.

Original material: Submission of an article implies that the work described has not been published previously (except in the form of an abstract or as part of a published lecture or academic thesis), that it is not under consideration for publication elsewhere, that its publication is approved by all authors and that, if accepted, it will not be published elsewhere in the same form, in English or in any other language, without the written consent of the Publisher. Authors found to be deliberately contravening the submission guidelines on originality and exclusivity shall not be considered for future publication in this journal.

Supplying Final Accepted Text on Disk: If online submission is not possible: Once the paper has been accepted by the editor, an electronic version of the text should be submitted together with the final hardcopy of the manuscript. The electronic version must match the hardcopy exactly. We accept MS Word format only. Always keep a backup copy of the electronic file for reference and safety. Label the disk with your name. Electronic files can be stored on CD.

Notification: Authors will be notified of the acceptance of their paper by the editor. The Publisher will also send a notification of receipt of the paper in production.

Copyright: All authors must sign the Transfer of Copyright agreement before the article can be published. This transfer agreement enables Jordan Journal of Mechanical and Industrial Engineering to protect the copyrighted material for the authors, but does not relinquish the authors' proprietary rights. The copyright transfer covers the exclusive rights to reproduce and distribute the article, including reprints, photographic reproductions, microfilm or any other reproductions of similar nature and translations.

PDF Proofs: One set of page proofs in PDF format will be sent by e-mail to the corresponding author, to be checked for typesetting/editing. The corrections should be returned within 48 hours. No changes in, or additions to, the accepted (and subsequently edited) manuscript will be allowed at this stage. Proofreading is solely the author's responsibility. Any queries should be answered in full. Please correct factual errors only, or errors introduced by typesetting. Please note that once your paper has been proofed we publish the identical paper online as in print.

Author Benefits

Page charge: Publication in this journal is free of charge.

Free off-prints: Three journal issues of which the article appears in along with twenty-five off-prints will be supplied free of charge to the corresponding author. Corresponding authors will be given the choice to buy extra off-prints before printing of the article.

Manuscript Preparation:

General: Editors reserve the right to adjust style to certain standards of uniformity. Original manuscripts are discarded after publication unless the Publisher is asked to return original material after use. If online submission is not possible, an electronic copy of the manuscript on disk should accompany the final accepted hardcopy version. Please use MS Word for the text of your manuscript.

Structure: Follow this order when typing manuscripts: Title, Authors, Affiliations, Abstract, Keywords, Introduction, Main text, Conclusions, Acknowledgements, Appendix, References, Figure Captions, Figures and then Tables. For submission in hardcopy, do not import figures into the text - see Illustrations. For online submission, please supply figures imported into the text AND also separately as original graphics files. Collate acknowledgements in a separate section at the end of the article and do not include them on the title page, as a footnote to the title or otherwise.

Text Layout: Use double spacing and wide (3 cm) margins. Ensure that each new paragraph is clearly indicated. Present tables and figure legends on separate pages at the end of the manuscript. If possible, consult a recent issue of the journal to become familiar with layout and conventions. All footnotes (except for table and corresponding author footnotes) should be identified with superscript Arabic numbers. To conserve space, authors are requested to mark the less important parts of the paper (such as records of experimental results) for printing in smaller type. For long papers (more that 4000 words) sections which could be deleted without destroying either the sense or the continuity of the paper should be indicated as a guide for the editor. Nomenclature should conform to that most frequently used in the scientific field concerned. Number all pages consecutively; use 12 or 10 pt font size and standard fonts. If submitting in hardcopy, print the entire manuscript on one side of the paper only.

Corresponding author: Clearly indicate who is responsible for correspondence at all stages of refereeing and publication, including post-publication. The corresponding author should be identified with an asterisk and footnote. Ensure that telephone and fax numbers (with country and area code) are provided in addition to the e-mail address and the complete postal address. Full postal addresses must be given for all co-authors. Please consult a recent journal paper for style if possible.

Abstract: A self-contained abstract outlining in a single paragraph the aims, scope and conclusions of the paper must be supplied.

Keywords: Immediately after the abstract, provide a maximum of six keywords (avoid, for example, 'and', 'of'). Be sparing with abbreviations: only abbreviations firmly established in the field may be eligible.

Symbols: All Greek letters and unusual symbols should be identified by name in the margin, the first time they are used.

Units: Follow internationally accepted rules and conventions: use the international system of units (SI). If other quantities are mentioned, give their equivalent in SI.

Maths: Number consecutively any equations that have to be displayed separately from the text (if referred to explicitly in the text).

References: All publications cited in the text should be presented in a list of references following the text of the manuscript.

Text: Indicate references by number(s) in square brackets in line with the text. The actual authors can be referred to, but the reference number(s) must always be given.

List: Number the references (numbers in square brackets) in the list in the order in which they appear in the text.

Examples:

Reference to a journal publication:

[1] M.S. Mohsen, B.A. Akash, “Evaluation of domestic solar water heating system in Jordan using analytic hierarchy process”. Energy Conversion & Management, Vol. 38, No. 9, 1997, 1815-1822.

Reference to a book:

[2] Strunk Jr W, White EB. The elements of style. 3rd ed. New York: Macmillan; 1979.

Reference to a conference proceeding:

[3] B. Akash, S. Odeh, S. Nijmeh, “Modeling of solar-assisted double-tube evaporator heat pump system under local climate conditions”. 5th Jordanian International Mechanical Engineering Conference, Amman, Jordan, 2004.

Reference to a chapter in an edited book:

[4] Mettam GR, Adams LB. How to prepare an electronic version of your article. In: Jones BS, Smith RZ, editors. Introduction to the electronic age, New York: E-Publishing Inc; 1999, p. 281-304

Free Online Color: If, together with your accepted article, you submit usable color and black/white figures then the journal will ensure that these figures will appear in color on the journal website electronic version.

Tables: Tables should be numbered consecutively and given suitable captions and each table should begin on a new page. No vertical rules should be used. Tables should not unnecessarily duplicate results presented elsewhere in the manuscript (for example, in graphs). Footnotes to tables should be typed below the table and should be referred to by superscript lowercase letters.

JJMIE
Volume 4, Number 3, June,2010
ISSN 1995-6665
Jordan Journal of Mechanical and Industrial Engineering

JJMIE
Jordan Journal of Mechanical and Industrial Engineering

Volume 4, Number 3, June,2010
ISSN 1995-6665
Pages 340 - 345

Aldehyde and BTX Emissions from a Light Duty Vehicle Fueled on Gasoline and Ethanol-Gasoline Blend, Operating with a Three-Way Catalytic Converter

Asad Naeem Shah[a, b,*], Ge Yun-shan[a] and Zhao Hong[a]

[a]*School of Mechanical and Vehicular Engineering, Beijing Institute of Technology Beijing 100081, P. R. China*

[b]*Department of Mechanical Engineering, University of Engineering and Technology Lahore 54000, Pakistan*

Abstract:

The current work is aimed at the experimental investigation of the aldehyde and BTX (benzene, toluene and Xylene) pollutants emitted from a light duty spark ignition (SI) vehicle fueled on gasoline and ethanol-gasoline blended fuel, operating with a three-way catalytic converter (TWC). At the same time, the specific reactivity (SR) of these pollutants has also been addressed in this paper. The experiments were performed on both transient as well as steady modes following the standard protocols recommended for light duty vehicles. Aldehyde and BTX species were analyzed using high performance liquid chromatography (HPLC) and gas chromatography/mass spectroscopy (GC/MS), respectively. During the transient cycle of operation, formaldehyde and BTX emissions were decreased, while acetaldehyde and acrolein+acetone pollutants were increased with (10% ethanol – 90% gasoline by volume), compared with E-0 (neat gasoline). During the steady modes, formaldehydes with E-0 were dominant to those with E-10 fuel. Acetaldehydes with E-10 showed dominancy to those with E-0, and were the most abundant components among the other aldehyde species. Formaldehydes were decreased with the increase in speed, and toluene was found to be the most abundant component of the BTX emissions with both the fuels. The BTX components displayed their maxima at lower speed mode and minima at medium speed mode for both the fuels, and were decreased in case of E-10, compared with E-0. The SR of the transient mode pollutants was lower as compared to that taken from the mean of the steady mode pollutants. In case of E-10, the SR of the pollutants was higher at both transient as well as steady modes, compare with E-0 fuel.

Keywords: Ethanol; Non-Regulated Emissions; Carbonyls; Three Way Catalytic Converter; Volatile Organic Compounds.

1. Introduction

The modern era of science and technology has changed the life style of human beings by facilitating them with increased fleet of buses, trucks, motor cars, aircrafts, ships, and agricultural and construction machinery. Consequently, the world has been forced to confront with the number of issues such as the energy crisis, global warming and environmental pollution leading to the harmful effects on human life. In order to meet the increasing energy needs, researchers are converging their attention to the alternative fuels like methanol, ethanol, liquefied petroleum gas (LPG), liquefied natural gas (LNG), compressed natural gas (CNG), vegetable oils and biodiesel.

Motor vehicle emissions are one of the major anthropogenic sources of air pollution and contribute to the deterioration of urban air quality [1]. When a new fuel is introduced in the market, a prerequisite is that pollutants emitted from a vehicle are not more toxic than those emanated when it is running on the standard market fuel [2]. Ethanol is an oxygenated, biodegradable, regenerative and promising alternative biofuel for vehicle engines with least adverse impacts on public health and environment. Carbon dioxide (CO_2) released by the burned ethanol can be fixed by growing plants and therefore makes less net greenhouse gas contribution to global warming, compared with fossil petroleum [3]. Ethanol is made up of a group of chemical compounds whose molecules contain a hydroxyl group (– OH) bounded to a carbon atom. So, its oxygen content favors the further combustion of gasoline blended with it [4].

Ethanol is considered to be an excellent fuel for spark ignition (SI) engines, having a high octane number and can be used without major engine modifications [2]. Its blend with gasoline has widely been used in many countries like USA, the European Union, Canada, Brazil and Thailand [5]. In China, the gasoline is being sold with an addition of 10% (v/v) ethanol in its nine provinces, with a primary motive to minimize the dependence on imported petroleum sources and to reduce the carbon monoxide

* Corresponding author. naeem_138@hotmail.com and anaeems@uet.edu.pk.

  - Volume 4, Number 3 (ISSN 1995-6665)

(CO) and particulate matter (PM) [6]. Since 2001, all gasoline sold in eastern Sweden contains approximately 5% ethanol [2].

In the current study, E-10 (a mixture known as gasohol) has been used as an alternative fuel to E-0 in a gasoline car. Although some studies have been reported on regulated emissions from ethanol-gasoline blended fuels, unregulated emissions still need to be addressed comprehensively particularly, when the vehicle is equipped with a TWC. This study is focused on the comparative analysis of aldehydes and BTX emissions from a spark ignition vehicle fuelled with gasoline and its blend with ethanol, operating with a TWC system both on transient as well as steady modes. Furthermore, the ozone forming potential of the pollutants has also been discussed in terms of their SR. So, this study would be helpful to investigate the emissions of compound playing a critical role on tropospheric chemistry, and are considered to be toxic, mutagenic, and even carcinogenic to humans

2. Material and Methods

2.1. Test Vehicle, Fuels and Experimental Conditions

The experiments were performed on a 4 cylinder, 1.3-liter displacement volume, 60 kW, multi port fuel injected (PFI), dual fuelled, recent model EURO – III compliant vehicle equipped with a TWC designed and developed for minimum optimized regulated pollutants with E-10 fuel. The test vehicle was run on a 1.0 m single roll DC electrical chassis dynamometer (ONO SOKKI Inc.), according to cycle shown in Figure 1. Part one of this cycle consists of four sub-cycles which simulate the urban regions; while the part two of the cycle simulates the main motor-way/highway out of the urban regions. The average speed of the vehicle during the test was 33.58 km/h. In order to investigate the pollutants in the steady mode, the vehicle was run at the speeds of 40, 80 and 120 km/h for 300 seconds. In order to avoid the possible interference caused by the residues in oil pipeline, a separate fuel tank was used in this study. The schematic diagram of the experimental setup is given in Figure 2.

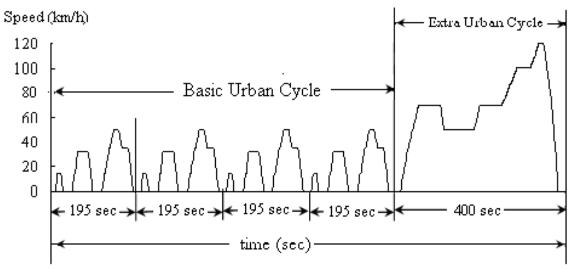

Figure 1. Operating cycle of test vehicle

The fuels used in this study are unleaded gasoline having research octane number (RON) 93 and gasoline-ethanol mixture containing 10% ethanol and 90% gasoline (v/v), with gasoline as a reference or baseline fuel. The properties of the fuels are listed in Table 1.

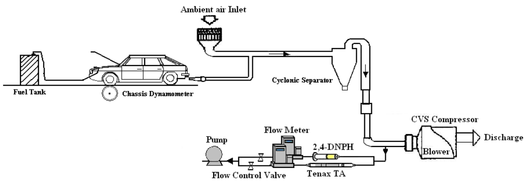

Figure 2. Experimental setup.

Table 1. Properties of the test fuels

Properties	Gasoline-ethanol blend	Gasoline
Density (Kg/L) at 20˚C	0.74	0.73
Gross heat content (MJ/kg)	42.2	46.0
Octane number	95.0	93.0
Oxygen content (wt %)	3.5	n/a
Carbonate content (wt %)	83.4	86.4
Hydrogen content (wt %)	13.1	13.6

2.2. Sampling Methodology

The sampling scheme is shown in Figure 1. In order to get a constant exhaust volume, a constant volume sampling (CVS) method consisting of a dilution tunnel of a standard critical flow venture was used. The exhaust from the vehicle was mixed with the fresh, filtered and low humidity atmospheric air to avoid the water condensation in the dilution tunnel. The atmospheric temperature and pressure were approximately 25°C and 100 kpa, respectively. The exhaust flow rate and the dilution ratio were 10 m^3/min and 15, respectively. The exhaust samples were taken in 2, 4-dinitrophenylhydrazine (DNPH) coated silica gel cartridges (Accustandard ® Inc.) and Tenax TA® tubes (Markes USA) for the aldehydes and BTX emissions, respectively. The DNPH inside the cartridges trapped the carbonyls to react with them and to form the corresponding stable 2, 4-dinitrophenylhydrazone derivatives. The sampling pumps were constant volume pumps (SKC USA, AirChek2000) and the sampling volume was 220 mL and it took 10 minutes to sample at every mode. Three samples of each E-0 and E-10 fuel were taken for the aldehyde and BTX species analyses. After sampling, the tubes were sealed with aluminum foil and were refrigerated at -10˚C.

2.3. Sample Extraction and Analysis

For the extraction of aldehydes trapped sample material, solid phase extraction (SPE) method was used, and the environment protection agency (EPA) standard method TO-11A [7] was used to analyze the aldehydes using HPLC (USA Agilent 1200LC) system with an automatic injector and an ultraviolet (UV) detector as discussed in detail elsewhere [8] .

In order to extract the species on Tenax TA®, automatic thermal desorber (TD), UNITY (Markes USA) was used in which Tenax tubes were first blown by the dry inert gases and then heated, and the EPA standard method TO-17 [9]

was used for the qualitative and quantitative analyses of the BTX emissions using GC/MS as discussed in detail elsewhere [10] however, Table 2 is given to show the scheme of thermal desorber, gas chromatograph and mass spectrometer (TD-GC/MS) system.

Table 2 .TD- GC/MS specifications [10]

Thermal desorber (TD)	Tube: 280°C (5 min); purge: 1 min; column pressure: 8.5 psi; split ratio: (75:1); cryotrap: from -10°C at 40°C/s to 280°C (3 min)
Gas chromatograph (GC)	Capillary column: HP-5MS (30m × 0.25 mm × 0.25 µm); column flux: 1mL/min; carrier gas: helium (99.999%); oven temperature program: from 35ºC (10 min) at 5ºC/min to 280ºC
Mass spectrometer (MS)	Transfer line to MS: 250ºC; ion source: electron impact (EI) 70 eV; ion source temperature: 200ºC; solvent cut time: 2.5 min; acquisition mode: SCAN; range of scan: 35-450 amu; electron multiplier voltage: 1.0 kV; NIST05 library

3. Results and Discussion

3.1. Transient Mode

3.1.1. Effect of Ethanol on Aldehydes Emissions

The aldehydes such as formaldehyde, acetaldehyde, acrolein + acetone, and aromatic aldehydes (benzaldehyde and tolualdehyde) have been selected in this study because of the three major reasons. Firstly, these species contribute maximum to the total aldehyde pollutants emanated from gasoline and gasoline-ethanol fuelled spark ignition engines [5 and references therein]. According to Pang et al. [6], formaldehyde, acetaldehyde, acrolein, and aromatic aldehydes are the dominant components which account for up to 82.2% and 85.1% of total carbonyl emissions from gasohol and gasoline fuels, respectively. Secondly, the presence of correctly operated TWC results in the oxidation of such pollutants leading to a negligible small or even zero magnitude for some of them. Thirdly and most importantly, pollutants like formaldehyde, acetaldehyde and acrolein have been declared as possible human carcinogens. According to US EPA [11], formaldehyde is a probable human carcinogen (Group B1); acetaldehyde is a possible human carcinogen (Group 2b); and acrolein is a probable human carcinogen (Group C). Moreover; Carlier et al. [12] has reported that aldehydes like formaldehyde, acetaldehyde, and acrolein are mutagenic, toxic, and even carcinogenic to human body. According to Poulopoulos et al. [13], acetaldehyde and acetone are involved in the photochemical smog generation cycle while acetaldehyde is also a toxic compound. Since, it was difficult to separate acrolein and acetone in the column because of their same retention time (almost same), so they have been discussed together in this study.

As shown in Figure 3 (a), formaldehyde decreases by 46% however, acetaldehyde and acrolein+acetone increase by about 3 times and 1.6 times, respectively in case of E-10 compared with E-0. Benzaldehyde and tolualdehyde show their significant appearance only in case of E-0 fuel.

This phenomenon of increase in acetaldehyde with a decrease in formaldehyde from E-10 as compared to E-0 is also supported by other literature [5-6]. The increase in acetaldehyde in case of E-10 is due to the oxidation of ethanol to acetaldehyde. On the other hand, the increase in formaldehyde in case of E-0 is attributed to the incomplete combustion of the gasoline fuel as compared to oxygenated gasohol fuel. According to Magnusson et al. [5], formaldehyde from the vehicle exhaust mainly comes from the inefficient combustion of saturated aliphatic and aromatic hydrocarbons frequently present in E-0. It has been reported that the presence of TWC augments the rate of oxidation of E-10 [13-14], thus results in reduced formaldehydes. The increase in acrolein+acetone in case of E-10, relative to E-0 may be ascribed to two factors. First to TWC which has shown comparatively a better efficiency in the oxidation of acrolein+acetone precursors with E0, and then to acrolein which comes mostly from the oxidation of glycerol and other residues present in the biofuels like gasohol. The absence of aromatic aldehydes (benzaldehyde and tolualdehyde) in case of E-10 is due to the less aromatic content in biofuels, relative to fossil fuels.

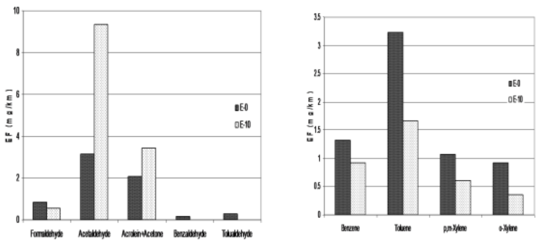

(a) (b)

Figure 3. Effect of Ethanol on (a) Aldehydes and (b) BTX Emissions in transient mode.

3.1.2. Effect of Ethanol on BTX Emissions

The BTX-components have been discussed in this study because of the health hazards associated with them. According to International chemical safety cards published by National Institute for Occupational Safety and Health (NIOSH) U.S.A., benzene is carcinogenic to humans and may affect the blood forming organs, liver and immune system; toluene may affect the central nervous system, resulting in decreased learning ability and psychological disorders; p,m-xylene may have effects on the central nervous system and may cause toxicity to human reproduction or development; and o-xylene may cause damage to central nervous and hearing systems [2]. It has also been reported that the exposure to benzene increases the risk of leukemia [11]. According to Poulopoulos et al. [13],benzene and toluene belong to aromatics– compounds accused of cancer generation. Furthermore, xylene isomers may convert significant amounts of NO to NO_2 [15].

As shown in Figure 3 (b), the decrease in emission factor (EF) of benzene, toluene, p,m-xylene and o-xylene is 37%, 48.3%, 43% and 71.8%, respectively.

consequently, there is a decrease of 54.4% in total BTX emissions in case of E-10 compared to E-0.

The reduction in BTX emissions is due to the oxygen enrichment in ethanol, contributing to the complete oxidation of BTX species in case of E-10, relative to E-0. According to Reuter et al. [16], benzene emissions were reduced by 10.5% with the oxygenated fuels. Besides this, physic-chemical properties like lower boiling point, faster flame propagation speed, and simple chemical structure help E-10 in the quicker development of temperature, relative to E-0. The higher temperature developed in the combustion chamber with E-10 is useful for the oxidation of BTX species. Moreover, the performance of TWC is further enhanced for the decomposition of BTX species in case of E-10, compared with E-0. This decrease in benzene and toluene with E-10 in the presence of TWC is also supported by other literature [13].

3.2. Steady Mode

3.2.1. Effect of Ethanol on Aldehydes Emissions

Figure 4 (a) shows the aldehyde emissions at three different modes of 40, 80, and 120 km/hr. Formaldehydes emitted with E-0 are dominant to those emanated with E-10 for all the steady modes. Acetaldehydes in case of E-10, on the other hand, do not show only the dominancy to those emitted with E-0, but are the most abundant components among the aldehyde species for all the steady modes. Acrolein+Acetone emissions are higher with E-10 compared to those with E-0 for the first two steady modes. However, the third mode reflects a decrease in the acrolein+acetone emissions with E-10, relative to E-0. The reasons for lower formaldehyde and higher acetaldehyde and acrolein+acetone emissions with E-10 compared to E-0 are the same as discussed earlier in the transient mode.

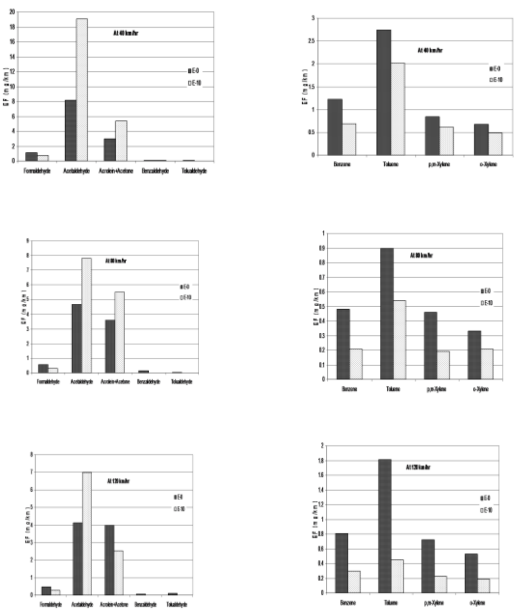

(a) (b)

Figure 4. Effect of Ethanol on (a)Aldehydes and (b) BTX Emissions in steady mode.

Table 3. EF of Total BTX emitted from the vehicle at different speed modes (mg/km)

Fuel	40 km/hr	80 km/hr	120 km/hr
E-0	5.49	2.17	3.87
E-10	3.80	1.15	1.17

3.2.2. Specific Reactivity

The specific reactivity is defined as the milligram (mg) ozone (O_3) potential per milligram non- methane organic gases (NMOG) emanated from the exhaust and can be evaluated as under [17]:

$$SR = \sum (NMOG_i \bullet MIR_i) / \sum NMOG_i \qquad (1)$$

The subscript i represents the certain pollutant emitted; NMOG is the sum of non-methane hydrocarbons and oxygenates, including aldehydes and BTX; and MIR is the maximum incremental reactivity. Carter and Lowi [17], examined air modeling based on ozone forming reactivates of species and proposed the MIR factor as an index for ozone formation given in appendix Table A. This index indicates the maximum increase in ozone formation

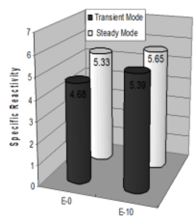

Figure 5. Specific reactivity of emissions from transient and steady modes.

Figure 5 shows the comparative SR of emissions from the vehicle at different working conditions in both transient as well as steady modes. For the steady mode, mean of the emissions at three different modes has been taken here. It is elucidated that pollutants in the transient mode of operation show less SR as compared to those emitted in steady mode. This is due to the fact that during the transient mode of operation, the total pollutants (sum of aldehydes and BTX) are less than the total mean (sum of mean) of the pollutants at steady modes as shown in Table 4. Relative to E-0, E-10 exhibits higher SR of pollutants for both transient as well as steady modes as shown in Figure 5. This higher SR in case of E-10 is ascribed to the higher acetaldehyde and acrolein+acetone emissions with gasohol, compared with gasoline.

Table 4. EF of Total pollutants at transient and mean steady state Modes (mg/km)

Fuel	Transient	Mean steady
E-0	13.13	13.90
E-10	16.90	18.28

4. Conclusions

Aldehyde and BTX emissions emanated from a TWC-retrofitted dual fuel light duty vehicle were studied in terms of their EF and SR. The vehicle was alternatively fueled with E-10 and, thus pollutants were compared with those emitted in case of baseline E-0 fuel. The experimental results showed that during the transient mode of operation, formaldehyde emissions were decreased by 46%, while acetaldehyde and acrolein+acetone emissions increased by about 3 times and 1.6 times respectively with E-10, compared with E-0. Benzaldehyde and tolualdehyde were significantly found only in case of E-0 fuel. Moreover, the benzene, toluene, p,m-xylene and o-xylene species with E-10 were decreased by 30.3%, 48.3%, 37% and 71.8% respectively, resulting in an overall decrease of 54.4% in the BTX emissions, compared with E-0.

During the steady modes, formaldehydes with E-0 were dominant to those with E-10 fuel. Acetaldehydes with E-10 showed dominancy to those with E-0, and were the most abundant components among the aldehyde species for all the steady modes. The acrolein+acetone emissions with E-10 were higher to those with E-0 for the first two modes. The formaldehyde emissions were decreased with the increase in speed in case of both E-0 and E-10 fuels. The toluene was found to be the most abundant component of the BTX emissions with both the fuels. The BTX emissions were decreased by 30.8%, 47% and 69.7% at 40, 80 and 120 km/hr respectively in case of E-10 compared to E-0. The total BTX emissions (sum of all the components) exhibited their maxima at lower speed mode and minima at medium speed mode for both the fuels.

The specific reactivity of the pollutants emitted intransient mode was less than that calculated from the mean of the three steady modes pollutants in case of both the fuels. Relative to E-0, E-10 fuel displayed the higher SR for both transient as well as steady modes of operation.

Acknowledgements

The authors acknowledge the financial support of National Laboratory of Auto Performance and Emission Test, Beijing Institute of Technology (BIT) Beijing, P. R China, under the National Natural Science Foundation Project No. 50576063.

References

[1] S.M. Correa, G. Arbilla, "Carbonyl emissions in diesel and biodiesel exhaust". Atmospheric Environment, Vol. 42, 2008 769-775.

[2] D. Haupt, K. Nord, K. Egeback, P. Ahlvic, "Hydrocarbons and aldehydes from a diesel engine running on ethanol and equipped with EGR, catalyst and DPF". Society of Auto motive Engineering (SAE) Technical Paper Series No. 2004-01-1882, 2004.

[3] B. He, J. Wang, J. Hao, X. Yan, J. Xiao, "A study on emission characteristics of an EFI engine with ethanol blended gasoline fuels". Atmospheric Environment, Vol. 37, 2002, 949-957.

[4] L. Jia, M. Shen, J. Wang, M. Lin, "Influence of ethanol-gasoline blended fuel on emission characteristics from a four-stroke motorcycle engine". Journal of Hazardous Materials A, Vol. 123, 2005, 29-34.

[5] R. Magnusson, C. Nilsson, B. Andersson, "Emissions of aldehydes and ketones from a two stroke engine using ethanol and ethanol-blended gasoline as fuel". Environmental Science and Technology, Vol. 36, 2002, 1656-1664.

[6] X. Pang, Y. Mu, J. Yuan, H. He, "Carbonyls emission from ethanol-diesel used in engines". Atmospheric environment, Vol. 42, 2008, 1349-1358.

[7] US. Environment Protection Agency (US EPA), "Determination of formaldehyde in ambient air using adsorbent cartridge followed by high performance liquid chromatography (HPLC)". Compendium method TO-11A, 1999.

[8] A.N. Shah, G. Yun-shan, T. Jian-wei, "Carbonyls emission comparison of a turbocharged diesel engine fuelled with diesel, biodiesel, and biodiesel-diesel blend". Jordan Journal of Mechanical and Industrial Engineering (JJMIE), Vol. 2, No. 3, 2009.

[9] US. Environment Protection Agency (US EPA), "Determination of volatile organic compounds in ambient air using active sampling onto sorbent tubes". Compendium method TO-17, 1999.

[10] A.N. Shah, G. Yun-shan, T. Jian-wei, L. Zhi-hua, "Experimental investigation of VOCs emitted from a DI-CI engine fuelled with biodiesel , diesel, and biodiesel-diesel". Pakistan Journal of Scientific and Industrial Research (PJSIR), Volume 52, No.3, 2009.

[11] US. Environment Protection Agency (US EPA), "Cancer risk from outdoor air toxics". Washington 1, 1990, 450-451.

[12] P. Carlier, H. Hannachi, G. Mouvier, "The chemistry of carbonyls in the atmosphere- a review". Atmospheric Environment, Vol. 20, 1986, 2079-2099.

[13] S.G. Poulopoulos, D.P. Samaras, C.J. Philippopoulos, "Regulated and unregulated emissions from an internal combustion engine operating on ethanol-containing fuels". Atmospheric Environment, Vol. 35, 2001, 4399-4406.

[14] E. Zervas, X. Montagne, J. Lahaye, "Emission of alcohols and carbonyl compounds from a spark ignition- influence of fuel and air/fuel equivalence ratio". Environmental Science and Technology, Vol. 36, 2002, 2414-2421.

[15] D. Simpson, "Hydrocarbon reactivity and ozone formation in Europe". Journal of Atmospheric Chemistry, Vol. 20, 1995, 163-177.

[16] R.M. Reuter, J.D. Benson, V.R. Burns, R.A. Gorse Jr., A.M. Hochhauser, W.J. Koehl, L.J. Painter, B.H. Rippon, J.A. Rutherford, "Effects of oxygenated fuels and RVP on automotive emissions, SAE Technical Paper Series No. 920326, 1992.

[17] W.P.L. Carter, A. Lowi, "Method for Evaluating the Atmospheric Ozone Impact of Actual Vehicle Emissions". SAE Technical Paper Series No. 900710, 1990.

Appendix

Table : MIR values for aldehyde and BTX emissions

BTX	MIR	Aldehydes	MIR
Benzene	0.42	Formaldehyde	7.15
Toluene	2.73	Acetaldehyde	5.52
p,m-Xylene	7.64	Acrolein+Acetone	6.77*,0.56**
o-Xylene	6.46	Benzaldehyde	-0.56
		Tolualdehyde	-0.56

6.77* is for acrolein and 0.56** is for acetone

JJMIE

Volume 4, Number 3, June. 2010
ISSN 1995-6665
Pages 346 - 351

Jordan Journal of Mechanical and Industrial Engineering

Simulation-Based Optimization for Performance Enhancement of Public Departments

Omar Bataineh*, Raid Al-Aomar, Ammar Abu-Shakra

Department of Industrial Engineering Jordan University of Science and Technology,Irbid 22110, Jordan

Abstract

This paper proposes an approach for enhancing the performance of public departments that are characterized by congestion and low efficiency. The proposed approach utilizes discrete-event simulation (DES) tools integrated with optimization, and employs the key performance indicator (KPI) concept. Applied to the citizen affairs and passports (CAP) department in Jordan as a case study, a DES model was developed with the aid of ARENA software. Optimization results using OptQuest showed that performance of the optimized CAP department was better in various aspects compared to the current department. Waiting time was reduced the most by 91.7% on average, while number of processed documents was increased by 8.2%. The total daily revenue for the optimized CAP department was higher by 19.7%.

Key words: Simulation; Optimization; Key Performance Indicator; Public Departments

1. Introduction

Enhancement of real-world production and business systems often entails solving complex and NP-hard optimization problems developed with noticeable formulation and modeling challenges. This is often attributed to three main characteristics of real-world performance; complexity, nonlinearity, and dynamic and stochastic behavior [1]. Hence, it is common among researchers to tackle real-world problems by developing representative mathematical and computer models and applying proper optimization and search methods. This applies to design problems of new systems as well as to enhancement problems of existing systems.

To compensate for the limitations of mathematical models in capturing the characteristics of real-world systems, simulation-based optimization methods were developed by applying a search algorithm on an optimization problem that is represented using a DES model [2]. In this representation, the complex structure of the often nonlinear, stochastic, and dynamic objective function and constraints are evaluated by computer simulation without the need to approximate a closed-form definition of the problem.

By utilizing computer capabilities in logical programming, random number generation, fast computations, and animation, DES is capable of capturing the characteristics of real world processes allowing analysts to estimate the performance measures of a system under a range of design parameter settings [3]. This performance is usually a complicated stochastic function of these parameters. To measure such performance, DES imitates the operation of the real-world system as it evolves over time and predicts the system's behavior without requiring a closed-form definition of the performance function. Such a capability makes DES superior to mathematical models, and more practical and less expensive than physical experimentation. Hence, the application of simulation studies in systems design and improvement has become common practice in the development of manufacturing systems, business operations, and the services sector [4-6].

Different approaches have been used in the literature to optimize or draw inferences from the output of a simulation model. Taguchi’s Experimental Design using Orthogonal Arrays (OA) was applied to many simulation studies to seek a system-level parameter settings based on certain response signal that is evaluated through simulation runs [7]. In addition to Taguchi's approach, some methods have utilized more efficient search engines from the field of Artificial Intelligence (AI). Common intelligent search methods in parameter design applications (combinatorial optimization) include genetic algorithms [8], Tabu search [9, 10], and neural networks [11]. A complete discussion of different simulation-based optimization methods is found in [12-14].

* Corresponding author. omarmdb@just.edu.jo.

As a reflection to these advancements in simulation-based optimization, simulation software vendors have integrated experimental design and optimization search modules into their simulation packages. Examples include AutoStat of AutoMod, Optimizer of Witness, and OptQuest of Arena.

The focus of this paper is on utilizing simulation-based optimization to enhance the performance of a real-world system as the citizen affairs and passports (CAP) department in Jordan. It presents an approach that employs the key performance indicator (KPI) concept to evaluate system performance. Arena simulation software is used to develop the DES model of the public service office and OptQuest is used for optimization.

2. Solution Approach

The proposed solution approach for simulation-based optimization is depicted in Figure 1. The developed framework comprises two parallel yet interrelated processes; the simulation process and the optimization process. The functionality of both processes eventually leads to obtaining a near-optimal solution (design changes) to enhance the performance of the underlying system. The implementation of this solution to the real-world system combined with the deployment of sustainability controls is expected to result in improving the KPI measures of system performance.

The simulation process starts from the definition of the enhancement or design problem at the selected production or business system. This includes a definition of the scope and objectives of the intended project. Specific problem definition results in correct problem formulation to start the optimization process. This includes defining decision variables (controls), objective function, constraints, and requirements. Problem definition also helps in directing the effort for collecting pertinent data. Collected data often includes system structure, logic, flow, cycle times, reliability of resources, etc. The collected data is used to set the parameters (coefficients and bounds) of the formulated optimization problem.

Using the environment (platform) of the selected simulation software, the DES model is built so that the realistic characteristic of the underlying system are captured using logical design and probabilistic models. The integrated optimization module is also developed using the variables and performance measures defined in the developed DES model. The behavior of the DES model is verified compared to the intended logical design and validated using actual performance data. Test runs are used to check the performance of the optimization module.

Finally, the optimization search engine is applied to the DES model to perform the optimization in iterations of developing controls combinations and simulation-evaluation until termination condition is reached. The optimal controls are validated using the DES model and set for implementation.

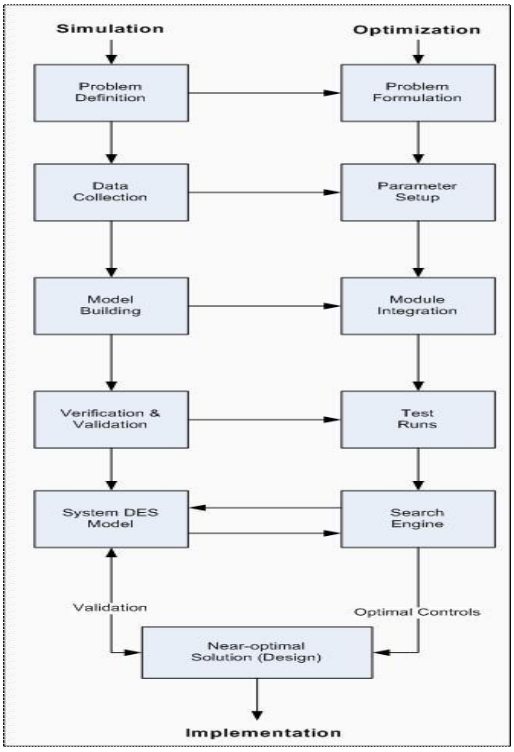

Figure 1. Framework for Simulation-based optimization

In this work, the proposed solution procedure depicted in Figure 1 is applied and demonstrated through a case study. The simulation aspect of the procedure is conducted with the aid of ARENA software. This includes data gathering and fitting, DES model building and model verification. Meanwhile, the optimization portion of this study is carried out with the aid of OptQuest optimizer. Relevant steps in this phase include determining system variables, defining objective function(s), and specifying linear constraints on system variables as well as certain performance measures (sometimes called goal functions). Then, a search algorithm is applied to search for the optimal solution. The last step occurs at the end of each run of the simulation model used for the evaluation of the objective and goal functions.

3. Case Study: Citizen Affairs and Passports Department

The citizen affairs and passports (CAP) department, which is adopted as the case study, issues four main documents to Jordanian citizens: Passports (PA), Birth Certificates (BC), Family Books (FB) and Identity Cards (ID). The floor layout for this department is represented in Figure 2. This figure shows the primary elements in the department (primary and secondary checking staff, cashiers, data entry staff and printers), which are used to issue the four documents, plus the queue lines and management

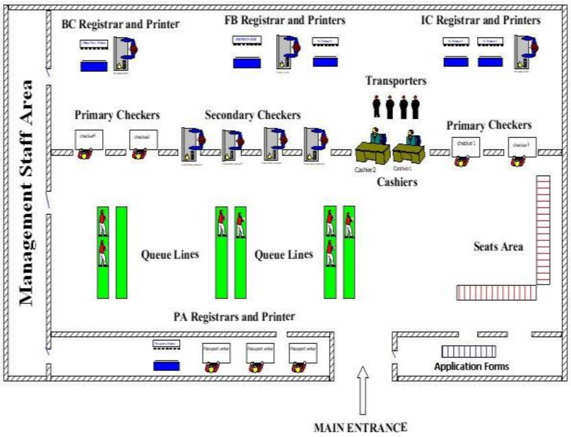

Figure 2. Floor layout of the actual CAP department

Customers who seek any of the four documents usually receive assistance from special preparers to complete the right application form outside the CAP department. Once the customer is in the department, several sequential steps must be taken to obtain the sought document, as shown in Figure 3. Firstly, the customer waits for one of the four primary checking staff to become available to get his application form checked for correctness and completeness and then stamped. If the application form was lacking correctness or completeness, the customer is asked to make the required changes and wait in line (or queue) again. Once the primary checking is complete, the customer turns to the secondary checking staff whom responsible for verification of the entered data through comparison with the supporting documents. The customer waits until one of the four secondary checking staff is available then gets the form verified and thus stamped. Then, the customer pays the fees required to issue the document at either of the two cashiers, whoever is available. The fee rates for the PA, IC, FB and BC documents are 20 JD, 2 JD, 2 JD and 1 JD, respectively.

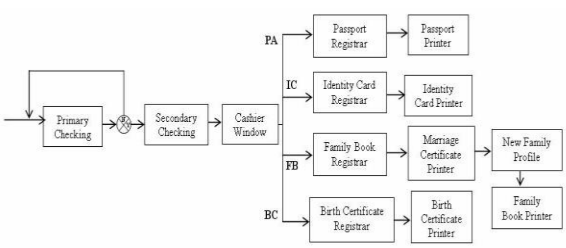

Figure 3. Schematic diagram for obtaining documents from CAP department

Up to this point, customers seeking one of the four documents go through the same steps of primary checking, secondary checking and paying fees at the cashiers. After paying the fees, the application forms are transferred by the four staff (transporters) responsible for delivering these forms to each of the four registrars, based on the type of the document required. As the passport registrars (three of them exist), identity card registrar, family book registrar and birth certificate registrar receive the application forms; they process these forms by entering the data into the computer and do the required editing. Finally, the PA, IC, FB and BC documents are printed and provided to the customer. However, in the case of the FB documents the family book registrar prompts printing a copy of the marriage certificate on a separate printer. The marriage certificate is then attached to create a new family record and the FB document is finally printed. One printer is available per each type of document except for the IC documents which have two printers.

3.1. Data Collection and Analysis

To simulate the operation of the CAP department, it is required to collect data to describe the arrival rates of the different customers at the department, the delay times at each stage within the department, and the times of transferring the application forms between the cashier and the four registrars through the transporters. Data were collected experimentally through observation of the various activities during the work hours of the CAP department. Data collected were then imported into Arena Input Analyzer to fit the probability distributions that will be used in the model in conjunction with random number generators (RNG) to simulate the stochastic operation of the CAP department. The results of data collection and analysis for the arrival rates of the customers at the CAP department and the delay times at each stage within the department are summarized in Table 1.

The transfer time of the application forms between the cashier and the four registrars was estimated based on the distances between the cashier and the registrars and the average transporter speed. The distances between the cashier and the PA, IC, FB and BC registrars were 20 m, 3 m, 6 m and 8 m, respectively. The average speed of the transporters is approximately 60 m/min. Therefore, the transfer time can be calculated as the distance to be traveled divided by the average transporter speed.

Table 1. Arrival rates and delay times at the CAP department

	Time (minute)	
Activity	Distribution	Parameters
PA arrival rate	Exponential	5.5
IC arrival rate	Exponential	13
FB arrival rate	Exponential	4.5
BC arrival rate	Exponential	8.5
PA primary checking	Triangular	(3,6,9)
IC primary checking	Triangular	(3,5,7)
FB primary checking	Triangular	(2,4,6)
BC primary checking	Uniform	(2,4)
PA secondary checking	Triangular	(4,6,10)
IC secondary checking	Triangular	(4,6,10)
FB secondary checking	Triangular	(4,6,10)
BC secondary checking	Triangular	(4,6,10)
PA fee payment	Uniform	(1,3)
IC fee payment	Uniform	(1,3)
FB fee payment	Uniform	(1,3)
BC fee payment	Uniform	(0.5,3)
PA data registering	Triangular	(15,18,25)
IC data registering	Uniform	(1,2)
FB data registering	Uniform	(4,6)
BC data registering	Triangular	(1,2,3)
Family profile registering	Triangular	(4,6,8)
PA printing	Triangular	(2,4,8)
IC printing	Triangular	(12,15,20)
FB printing	Uniform	(2,8)
BC printing	Triangular	(2,3,4)
Marriage cert. printing	Uniform	(2,8)

3.2. System Modeling

The system was modeled using Arena with various modules that represent the different aspects of the CAP department, as shown in Figure 4. For example, customer arrival rates were modeled using CREATE and STATION modules which carry the information about the arrival probability distributions, given in Table 1. Primary checkers, secondary checkers, cashiers and registrars were represented using STATION and PROCESS modules which provide the delay time distribution information to the modeler. The four staff responsible for transferring the application forms from the cashiers to the registrars were modeled using LEAVE and ENTER modules supplemented by the destination distances and the number of transporters available and the average speed. Other types of modules were also required in the model to fully describe the behavior of the system such as DECIDE and ROUTE modules.

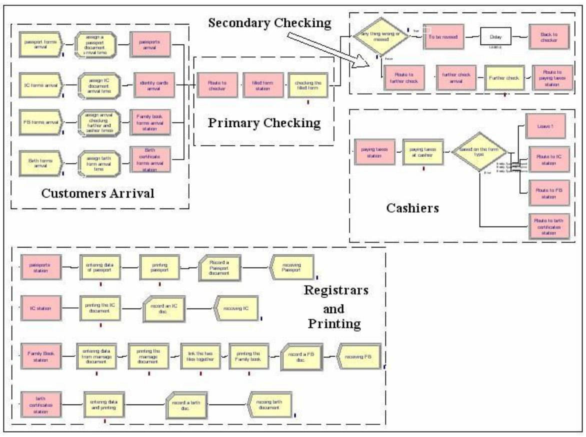

Figure 4. Arena Model structure of the CAP department

4. Simulation Results

4.1. Current System

Simulation of the current CAP department (shown in Figure 4) is useful for the validation of the developed system model and for evaluating the usefulness of any changes to be made to the current system. Due to the probabilistic nature of discrete-event simulation, the model was run 35 times, where each run represents one business day. Thus, all the simulation results presented in this study are based on the average of 35 runs. Unlike other systems characterized by continuous operation, the business day in the CAP department consists of a single shift starting from 8:00 AM and ending at 3:00 PM. Thus, the type of simulation used for this case is a terminating simulation.

Results of the model simulation for the present CAP department are presented for four selected key performance indices (KPIs), as shown in Table 2. A fifth KPI, which is the total daily revenue, is calculated by multiplying the number of processed documents by the fee per document for all document types and taking the total sum which gave 1,348 JD/day. Some of the results listed in Table 2 were compared to experimental data in terms of the total number of application forms processed and total time spent in the system. The simulation results were found in good agreement with the experimental data. Also, it can be seen in Table 2 that there are relatively significant amounts of incompletely processed application forms (Work-In-Process) remaining in the system at the end of the business day especially for passports. Also, it can be seen that a significant amount of the total system time that is required to issue a document (row 4) is due to non-productive waiting time (row 3). These two observations suggest a relatively poor performance for the present CAP department which requires some changes to be made to improve the system.

Table 2. Simulation results in terms of KPIs for the current CAP department

KPI	PA	IC	FB	BC
Work-In-Process	15.4	5	4.4	5.7
Number processed	57	42	28	68
Waiting time (min)	39.1	15	27.4	16
System time (min)	81.3	41.9	54.9	30

4.2. Optimized System

A group of changes in the current system are proposed by specifying a set of design variables that are iteratively varied until a feasible solution with the best system performance is achieved. Besides, a fixed change in the floor layout of the CAP department is proposed by relocating the PA registrars and printers to a new location which is closer to the cashiers. The design variables considered were in terms of the number of registrars, printers and cashiers, as shown in Table 3. This table also shows constraints on the lower and upper bound for each design variable within which the search algorithm attempts to find an optimal solution. These design constraints can be useful in increasing the efficiency of the search for optimal solutions.

Table 3. Defined design variables for optimization of CAP department

Design Variable	Lower Bound	Upper Bound
PA registrars	2	5
PA printers	1	3
BC registrars	1	3
BC printers	1	3
IC printers	1	5
FB registrars	1	3
Cashiers	1	3

In addition to the design constraints, another set of constraints was imposed on the waiting times of the four types of application forms, as shown in Table 4. These constraints are sometimes called response constraints because the waiting times are response variables in this case. Defining these response constraints is useful in ensuring customer satisfaction through less waiting times at the levels specified in Table 4.

Table 4. Bound constraints defined on the various waiting times

Response Variable	Constraint (min)
PA waiting time	< 10
IC waiting time	< 6
FB waiting time	< 6
BC waiting time	< 5

Improving the performance of the present CAP department requires also that an objective be defined as a measure of performance. This objective was defined as the maximum total daily revenue for the CAP department. This variable is considered as the most important KPI since it depends on all other KPIs. For example, the total daily revenue is directly proportional to the number of processed application forms per day, which is also influenced by the waiting time of each application form in the system. Waiting time itself contributes to the total time that an application form spends in the system.

Given the objective, design constraints and response constraints, OptQuest within ARENA was used to implement the optimization approach proposed in this study. This was done by firstly using the design variable values in the present system as an initial solution. The feasibility of this solution is determined by checking if the design constraints are satisfied, otherwise a new set of design variable values that satisfy the design constraints is searched at a given step size. After selecting appropriate values for the design variables, OptQuest must invoke Arena to run a simulation and determine whether or not the current trial solution is feasible with respect to the response constraints, otherwise a new solution that satisfies both the design and response constraints is searched. If a feasible solution is found, a new solution that yields better system performance results is sought. This process continues until all the design variable possibilities are exhausted or a predetermined time limit is reached. Ultimately, the best solution was reached when the values for the design variables listed in Table 3 were set at 5, 3, 3, 2, 4, 1 and 3.

Results of the model simulation for the optimized system given the new design variable values are presented for the four KPIs, as shown in Table 5. Comparing these results with the results of the current system listed previously in Table 2, the percentage improvement in each KPI value can be calculated for each type of document issued by the CAP department. A summary of these calculated percentages are listed in Table 6.

Table 5. Simulation results in terms of KPIs for the current CAP department

KPI	PA	IC	FB	BC
Work-In-Process	15.4	5	4.4	5.7
Number processed	57	42	29	68
Waiting time (min)	39.1	15	27.4	16
System time (min)	81.3	41.9	54.9	30

Table 6. Percentage improvement in KPI values for the optimized CAP department compared to the current department

KPI	PA	IC	FB	BC	Average
Work-In-Process	50.0%	34.0%	52.3%	50.9%	46.8%
Number processed	22.8%	4.8%	3.6%	1.5%	8.2%
Waiting time	90.0%	90.7%	96.0%	90.0%	91.7%
System time	49.4%	32.2%	48.1%	48.3%	44.5%

It can be seen from Table 6 that performance of the optimized CAP department has improved in all respects relative to the current CAP department. Work-in-process was reduced by 46.8% on average leading to an average increase by 8.2% in number of processed documents by CAP department. Waiting time and system time were significantly reduced by 91.7% and 44.5% on average, respectively. The total daily revenue for the optimized CAP department was also calculated as 1,614 JD/day. This translates to a 19.7% increase in total daily revenue compared to the current system.

Although the performance of the optimized system for the CAP department is expected to improve compared to the current system, this requires a new investment by inquiring five printers and hiring six more employees. The initial cost of the five printers can be considered negligible over a long period of time. Also, the average daily wage per CAP department employee in Jordan is about 10 JD, which totals 60 JD per day. Therefore, the proposed system can still be profitable compared to the current system since its estimated total daily revenue is higher by 266 JD than that of the current system.

5. Conclusions

This paper has presented an approach for enhancing the performance of public departments such as the citizen affairs and passports department in Jordan. The CAP department system was represented by a DES model developed with the aid of ARENA software and supplemented with the gathered and fitted experimental data. OptQuest of ARENA was used to implement the optimization for the selected design variables to improve performance of the current system in terms of the defined KPIs. The optimization process included defining a suitable objective function, i.e. maximum daily revenue, and imposing linear constraints on the design variables (the number of registrars, cashiers and printers) and response variables (the four waiting times).

Results of model simulation and optimization showed that performance of the optimized CAP department was better overall compared to the current department. Waiting time was reduced the most by 91.7% on average, while number of processed documents was increased by 8.2%. Consequently, the total daily revenue for the optimized CAP department was increased by 19.7%.

References

[1] Q. Wang, C.R. Chatwin, "Key issues and developments in modelling and simulation-based methodologies for manufacturing systems analysis, design and performance evaluation". International Journal of Advanced Manufacturing Technology, Vol. 25, No. 1, 2005, 1254-1265.

[2] Y. Hani, L. Amodeo, F. Yalaoui, H. Chen, "Simulation based optimization of a train maintenance facility". Journal of Intelligent Manufacturing, Vol. 19, No. 1, 2008, 293-300.

[3] Law A., Kelton D. Simulation Modeling and Analysis. 3rd edition. McGraw-Hill, Inc, Lewis, PA, USA, 2000.

[4] T. Yang, P. Chou, "Solving a multi response simulation-optimization problem with discrete variables using a multiple-attribute decision-making method". Mathematics and Computers in Simulation, Vol. 68, No. 1, 9-21.

[5] R. Al-Aomar, "A methodology for determining system and process-level manufacturing performance metrics". SAE Transactions - Journal of Materials and Manufacturing, Vol. 111, No. 5, 2002, 1043-1050.

[6] R. Marasini, N. Dawood, "Simulation modeling and optimization of stockyard layouts for precast concrete products". Proceedings of the 2002 Winter Simulation Conference, 2002, 1731-1736.

[7] C. Ying, L. Derong, "An orthogonal array optimization for the economic dispatch with nonsmooth cost functions". Proceedings of the 44th IEEE Conference on Decision and Control - European Control Conference, 2005, 1264-1269.

[8] S.G. Lee, L.P. Khoo, "Optimising an assembly line through simulation augmented by genetic algorithms". International Journal of Advanced Manufacturing Technology, Vol. 16, No. 1, 2000, 220-228.

[9] J. Bachut, P. Smith, "Tabu search optimization of externally pressurized barrels and domes". Engineering Optimization, Vol. 39, No. 8, 2007, 899-918.

[10] V.P. Eswaramurthy, A. Tamilarasi, "Tabu search strategies for solving job shop scheduling problems". Journal of Advanced Manufacturing Systems, Vol. 6, No. 1, 2007, 59-75.

[11] M. Ercsey-Ravasz, T. Roska, Z. Néda, "Cellular neural networks for NP-hard optimization". Eurasip Journal on Advances in Signal Processing, 2009, doi:10.1155/2009/646975.

[12] F. Azadivar, "Simulation-optimization methodologies". Proceedings of the 1999 Winter Simulation Conference, 1999, 93-100.

[13] J. Swisher, P. Hyden, S. Jacobson, L. Schruben, "A survey of simulation optimization techniques and procedures". Proceedings of the 2000 Winter Simulation Conference, 2000, 119-128.

[14] O. Bataineh, H. Abdulla, A. Abu-Saif, "Development and application of a metaheuristic optimization procedure integrated with simulation for a bus transit system". IEEE International Conference on Industrial Engineering and Engineering Management, Singapore, 2008, 1749-1753.

JJMIE

Volume 4, Number 3, June,2010
ISSN 1995-6665
Pages 352 - 357

Jordan Journal of Mechanical and Industrial Engineering

Combustion Oscillations Diagnostics in a Gas Turbine Using an Acoustic Emissions

Salem A. Farhat , Mohamed K. Al-Taleb*

Mechanical and industrial Engineering Department, Faculty of Engineering, University of Al-Fateh, Tripoli , Libya

Abstract

One of the most important areas of combustion research is the attempt to understand, and control, combustor oscillations, sometimes called “hum” or “noise.” The combustion at very lean mixture produced new problems; “lean” systems have proven to be subject to combustion thermo-acoustic instabilities which could lead to induced pressure oscillations or a “hum”, the humming can increase to howling and cause serious damage to the machines involved unless power output is reduced. In order to begin to understand what humming is, it was necessary to collect and analyze the acoustic signal produced during the humming process occurs in Gas Turbine. In this paper, acoustic signals have been measured in GT combustor of the power plant at Al Rouweas (Bharat Heavy Electricals Limited BHEL, V 94.2 GT power plant) and analyzed during the humming phenomenon. The chosen method for data collection was an acoustic data acquisition system, the acquired acoustic signal was then analyzed with LabVIEW software, the software’s main feature is that capable of defining the acoustic signal (the hum) in many parameters, the most important of which were: power spectrum, auto correlation and the acoustic wave shape produced by the thermo-acoustic instability. The power spectrum gave a concise presentation of the main frequencies which constituted the hum’s acoustic wave pattern, and their relative amplitudes, this was very helpful in determining the acoustic mode of the combustion chamber.

Keywords:Acoustic Signals; Thermo-Acoustic; Combustion Instability; Gas Turbine; Humming.

Abbreviation	Description
NO_x	Nitrogen Oxide
AIC	Active Instability Control
GT	Gas Turbine
LabVIEW	Laboratory Virtual Instrument Engineering Workbench
dB	Decibel
BHEL	Bharat Heavy Electricals Limited
DQA	Data Acquisition
Fig	Figure
et. al	Et alii (and others)
Hz	Hertz

1. Introduction

The objective of this article is to provide the reader with an understanding of the mechanisms and control of combustion driven oscillations, often referred to as “humming.” These instabilities are manifested by oscillations in pressure, rate of heat release and flow rate. Thermo-acoustic oscillations have become a key issue in modern combustion. Although the thermoacoustic phenomenon typically governs, other factors associated with flow dynamics, pressure drop, vortex formation, periodic flame extinction, etc., including fluid-structure interaction effects, may play a role in sustaining the oscillation. Combustion instability is inherently complicated. As a result of this serious problem, it is necessary to find ways of suppressing or reducing the high magnitude of these pressure oscillations. From Rayleigh’s criterion, the thermo-acoustic instability can only occur if the magnitude of the phase between the heat release oscillations and the pressure oscillations at the flame is less than ninety degrees. It should be reiterated that this discussion has primarily concerned itself with the phasing, or timing, aspects of combustion instability initiation. These timing aspects are necessary. The unsteady heat release processes must not only be phased in such a way that they add energy to the acoustic field, but they must be also adding it at a rate that exceeds the rate of damping. Thus, while the associated characteristic times of various combustor processes are important, both the magnitude and phase of the heat release response to pressure perturbations are important issues that determine the stability behaviour of a combustion system. One main gap

* Corresponding author. mktaleb@yahoo.com

in the diagnostics is the ability to obtain a reliable quantitative measure of unsteady heat-release rate.

Combustion instabilities occur in many practical systems such as power plants. It is well known, the control of NO_x has become extremely important in many combustion systems, to limit the production of NO_x the flame is kept as lean as possible. However, this leads to a more unstable flame, with oscillating heat-release that couples with the pressure acoustics of the chamber. This problem had been revisited earlier on in 1859 by Rayleigh [1]. Rayleigh's criterion has been used in combustion instability studies, which is the coupling between unsteady heat release and acoustic pressure. This criterion states that if the local unsteady heat release q' (z, t), is in-phase with local pressure fluctuation p' (z, t), the pressure wave associated with the fluctuation will be locally amplified. In 1954, Putnam and Dennis [2] put Lord Rayleigh's hypothesis for heat-driven oscillation into a formula, which is known as the Rayleigh integral form:

$$\int_0^T p'(t)q'(t)dt > 0$$

Where p is the pressure, q the heat release, T the time of one period of a cycle and the symbol $'$ denotes the fluctuating quantities. The equation above states that the product of the heat release and the sound pressure fluctuation is integral over a period of oscillation T. If the integral of state is positive, then the oscillation is amplified, if it is negative, damping occurs. In other words, the phase difference or time lag τ between the heat release rate and the pressure oscillation determine whether the instability grows or decays. This leads to the most popular combustion control strategy, a phase shift controller. It senses pressure from the combustion chamber and adds time delay (phase shift) to the signal before the feedback into the acoustic system by a pre-installed loud speaker used to control the dynamic system.

In fact, many industrial and academic institutes have carried out extensive research into combustion instabilities in the last few decades. To suppress or reduce this phenomenon, two methods have been widely used for alleviating or eliminating combustion instabilities, via, passive and active control systems.

A number of studies have been conducted to understand the mechanisms of the combustion instabilities and control strategies of combustion oscillations by using active instability control (AIC). Several experimental studies have been conducted for thermoacoustic interaction in unstable combustors by using conventional active control . It is necessary to have an effective and robust control of combustion. One of several aspects in an active control loop is the sensing technique such as the use of a microphone to pick up the acoustic pressure, and then to an actuator by using feed back close system. Active control has been proposed as a different approach to eliminate combustion oscillations.

The first successful demonstration of active combustion control occurred in 1984 when, using a Rijke tube, a loudspeaker and a microphone as an actuator-sensor pair. Researchers demonstrated that a 40-dB reduction can be achieved in the heat-induced noise. Since then, this technology has grown considerably and has been studied in the context of a number of laboratory-scale (1 to 100 kW), medium-scale (100 to 500 kW), and large-scale rigs (1 MW and above). Control has been achieved in many cases with variable degrees of success. Several experimental results have been reported over the past decade for controlling thermally driven acoustic oscillations using active methods [3-12]. The phase-shift control strategy, which is sometimes referred to as a phase-delay or a time delay strategy, for example Heckl, (1990)[13] successfully used active combustion control extensively from laboratory-scale rigs. Annaswamy et al., (2000)[14] have shown that the loudspeaker dynamics can be modified by the housing used. The housing typically encloses some volume and can act as a Helmholtz resonator making the task of designing a controller more difficult. Richards et al., (1997) [15] made an experimental investigation of a 20 kW atmospheric pressure natural gas combustor; it has been used to study the active control of combustion oscillations. Combustion oscillations arising from fuel/air variations in a premixing fuel nozzle are controlled by periodic injection of fuel in the premixing zone of the fuel nozzle. Specifically, a 300 Hz oscillation with 4.5 kPa *rms* pressure amplitude was reduced by a factor of 0.30 (-10 dB). Control was accomplished using 50 Hz open-loop injections of fourteen percent of the total fuel.

Passive control techniques have been widely used in industrial burners for many years. Their application typically involves modifications to the fuel injector or combustor hardware to eliminate the source of the variation in heat release or to increase the acoustic damping in the system and thereby reduce the amplitude of any pressure oscillations. Typically passive measures are detuning a system by modifying its burners or the acoustics of its combustion chamber, by disturbing the propagation of sound waves via baffles.

Hermann et al., (1999) [16] document further improvements to the control design of a 260-MW heavy-duty gas turbine developed by Siemens AG Power Generation. They used AIC during start-up or part load operations of the hybrid burners. There results showed that, by activating AIC for both dominant frequencies of the second and third harmonics were damped by 20 and 15 dB respectively..

Passive control strategies use devices which are not time-varying in order to eliminate the formation of instabilities. These devices require a thorough understanding or measurement of the system dynamics because they can not dynamically respond to any changes that may occur during operations. Many researchers have avoided passive control specifically for the reason that it can not adapt to changes in the system. Others assert that passive control has failed in the past due to a lack of understanding the fundamental physical phenomena. If a thorough understanding of the system can be attained, then various physical components such as injector geometry, acoustic resonators, liner design, and many other smaller components can be modified or added to remove the instability. Researchers have already experimented with adjusting various components. Gysling et al., (2000) [17] used a Helmholtz resonator side branch, which acts as a notch filter, to reduce the excitation of a predetermined instability frequency. Using these resonators requires a thorough understanding of the combustion system so that the instability frequency can be determined a priori. The resonator's practicality is limited by its inability to adapt to various operating conditions. Schadow et al., (1992) [18] reviewed and studied the combustion instability related to vortex shedding in dump combustors, and their passive control. They showed that the development of heat release, which, when in phase with pressure oscillation, can drive the oscillations as stated by the Rayleigh criterion.

Another passive control technique which has received much attention recently is how the fuel nozzle location affects the potential for instabilities. Many researchers including Steele, (1999)[19]; Straub and Richards, (1998) [20]; Smith and Cannon, (1999) [21] have reported that axial adjustments in the location of the fuel spokes have a positive impact in eliminating thermoacoustic instabilities.

Due to the fact that the use of gas turbines is a very important method of electrical power generation (especially in dry inland regions), and the fact that humming is a real threat to high output power plants, humming is now at the centre of very serious research being carried out by researchers at the top manufacturers of GT power plants across the world. However, this problem is also a local problem, as it occurs at the west mountain GT power -plant (in Al Rouweas Libya), and since this paper is focused at signal processing, it was decided to collect and process humming signals for analysis. The analysis was computer aided via the use of software, and it was decided to use the results of the signal analysis, to determine the combustion mode of GT chamber (the frequency at which humming occurred).

Acoustic emission is inherently linked to flows in which the frequencies of pressure oscillation are within the audible range. It is a known fact that every flow configuration has its unique sound characteristics. However the acoustic emission of a flow is not widely used as a diagnostic source. One of the main drawbacks of acoustic investigation is the lack of spatial resolution. The signals are an integration of the entire space exposed to the sensor. The observation may have significant applications for the monitoring and study of industrial flows. For example, many industrial devices (e.g. gas turbines, jet engines) are difficult to access both optically and electronically. With a proper sound guiding system, the acoustic signals can be collected without much difficulty. Monitoring the engine performance through its acoustic emissions provides a better understanding of the acoustic characteristics of the engine. As well as being aimed at the understanding of the acoustic characteristics of gas turbines, the most important of which being thermo-acoustic instability, this paper is aimed at the study of the methods employed as an attempt to effectively control or reduce instability, passive control is one of -these methods, as well as other significant methods of controlling thermo-acoustic instabilities.

2. Experimental Setup

In this paper the experimental setup and measurement techniques used in this project have been presented. In order to provide accurate measurements of acoustic pressure, and other relevant parameters, a fast sampling system is required. The data acquisition system is based on a fast computer. The Electricity condenser type of microphone has been used to pick up the acoustic signal, its specifications are; Frequency rang 30 ~ 16000 Hz, Polar pattern is Omni directional, and the Sensitivity is -58 ± 3 dB. The microphone is connected to a data acquisition system through a National Instrument DAQ card with a maximum sampling rate of 1.25 Ms/sec and LabVIEW 7 software has been used for the data acquisition, monitoring and analysis. The experimental rig was the combustion chamber of the GT power plant at Al Rouweas The power plant was manufactured by Bharat Heavy Electricals Limited BHEL, and was a V 94.2 GT power plant, Figure1 shows the BHEL power plan. BHEL gas turbines are single-shaft machines of single-casing design. They are suitable for driving generators in base-load and peak-load plants and for mechanical drive applications. They can be used in combined gas-steam cycles and for district heating. They can burn liquid fuels, such as light or heavy fuel oils, or gaseous fuels with different calorific values, such as natural gas or blast-furnace gas. The gas turbine unit consists of the principle components named in Figure 2

The gas turbine uses air as working fluid which is drawn in and compressed by the compressor, Fuel is added and burnt in the combustion chamber, and then hot gas is expanded to atmospheric pressure in the turbine. The exhaust gas leaves the turbine through the exhaust diffuser for discharge into the stack or to the downstream plant components in the case of combined-cycle power plants. The useful output power is available at the compressor-end coupling to drive the generator. After the installation of the necessary signal recording software, the apparatus was assembled as shown in Figure 2, the microphone was placed 2 meters away from the power plant's combustion chamber, samples were taken before, during, and after the humming phenomenon, to provide the necessary data for a complete analysis of the transition from premixed to diffusion flame.

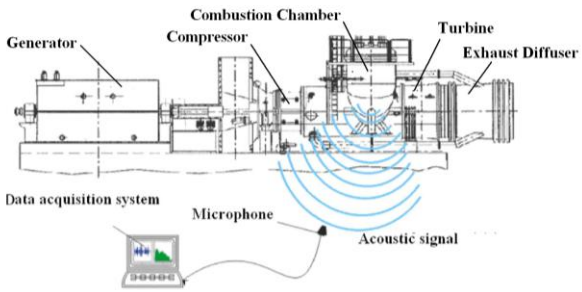

Figure 2.Bharat Heavy Electricals Limited BHEL, (V 94.2 GT power plant) and data acquisition system

3. Results and Discussions

Thermo-acoustic instability is a phenomenon which needs to be analyzed thoroughly when considering its effect on sensitive machines, such as gas turbines. This was taken into account when analyzing the 'humming' phenomenon that occurred at the Al Rouweas power plant, various methods of digital signal analysis were used to provide a clear rendition of the signal in terms of; power spectrum which displays the main dominant frequencies and their relative amplitudes, The correlation of signal (g) values at two instants of time is described by the autocorrelation function ($\Re_g$), which is defined in its most general form by:

Here the time difference, τ, is usually called delay or lag. The autocorrelation function can be determined from a

$$\Re_g(\tau) = \lim_{T\to\infty} \frac{1}{T} \int_{-T/2}^{T/2} g(t) g(t+\tau) dt$$

single sample signal. The function is even and it has its maximum value at τ = 0. With increasing τ, the function usually decreases towards the square of its mean value (the covariance function decreases towards zero). This may take place with damped oscillations. The autocorrelation function approaches zero at great lag values. The idea of autocorrelation function is to compare signal values at different instants of time, a positive $\Re_g$ means that the signal values have often the same sign, and a negative $\Re_g$ means that opposite signs are usually expected. If $\Re_g$ = 0, the relation of the signs is unpredictable. In addition to signs, the absolute values of the signals also contribute to the autocorrelation function. This implies that knowledge of the autocorrelation function, obtained from a measured signal, allows predictions to be made of the signal behaviour. The uncertainty of this prediction grows with time distance. Finally the acoustic wave form which shows the changes that occurs to the waveform during the stages of the transition.

The analysis of acoustic samples have been taken before, during, and after the transitory period (the transitory period is the time at which humming occurs), the actual ‘transition’ is a change in the type of flame used in the combustion chamber (from the premixed type flame to a diffusion type flame), the apparent cause of thermo-acoustic instability is applying very high loads to the power plant, while operating at a lean air fuel mixture and using a premixed flame, although operating at a lean air fuel mixture while using a premixed flame is both economic and environmentally friendly, as the load increases to very high loads humming occurs, since induced pressure oscillations are a result of humming, the resulting resonance could cause the turbine unit to fail and cause serious damage to the power plant, in order to avoid this, the combustion chamber switches to a diffusion flame type which is less economically and environmentally friendly, this ‘switch’ has the effect of preventing resonance by altering the frequency of combustion, this type of thermo-acoustic control is deemed as ‘passive control’, the switch is only temporary, in the sense that the diffusion flame will only be used until the load returns to its normal state. The whole process will be referred to as the ‘’transition’’, and the results of its analysis are as follows.

The acoustic signal that was recorded starts from about 2 minutes before the actual transition and continues to about 2 minutes after the transition, The sampling rate is 44100 s/sec and number of samples is 20000). a sample taken at the time before transition was analyzed, the results are as shown in figure 3, the power spectrum a shows that the dominant frequency is at approximately 50 Hz which is the frequency of the electricity produced by the power plant, the auto correlation shows that the signal is repetitive (is not merely noise), and the wave form also shows that it is a repetitive acoustic signal.

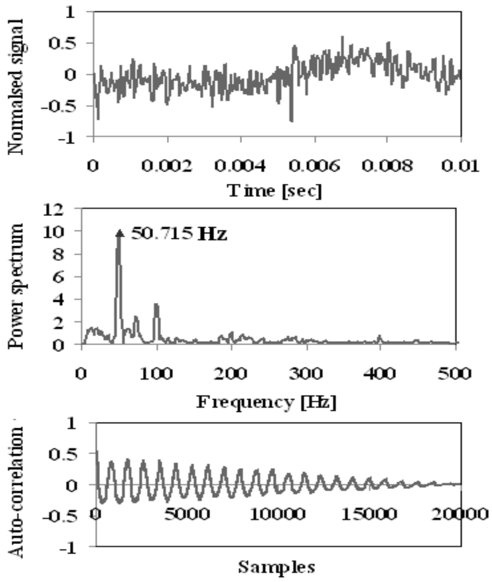

Figure 3.Power spectrum, Wave form, and Auto-correlation of sample taken before transition (premixed flame in use)

Another sample taken at the actual time of transition shows the changes that occur as resonance takes place, the power spectrum Figure 4 shows that the previous dominant frequency of 50 Hz has been dwarfed by a new dominant frequency of 72.765 Hz, which is the frequency at which resonance occurred i.e. the frequency at which the induced pressure oscillations matched the natural frequency of the combustion chamber. The transitory period is slightly noisier, the power spectrum also shows that the transitory period is slightly noisier, the auto-correlation Figure 4 shows an increase in the signals repetitiveness (correlation), this is due to the amplitude increase during the transitory period (from 9.852 volt (before transition) to 28.46 volt (during transition)) the increased amplitude of the dominant frequency means that the auto-correlation will be less affected by noise. The wave form Figure 4 also shows an increase in frequency and is slightly distorted by the increased noise level.

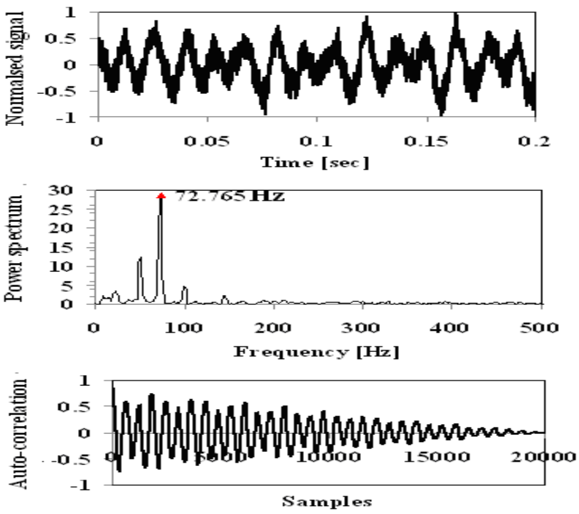

Figure 4.Power spectrum, wave form, and Auto correlation of sample taken at transition

Measurements taken using a sound pressure level meter confirm the increase in overall noise level; the measurements show a substantial increase in sound pressure level (from 98dB before transition to 123dB during transition).

The final sample was taken after the transition; the power spectrum Figure 5 shows that the dominant frequency has returned to the previous 50 Hz and that the noise level has decreased from what it was during the transition, the auto-correlation; Figure 5 shows a decrease in correlation due to the decrease in the dominant frequency's amplitude.

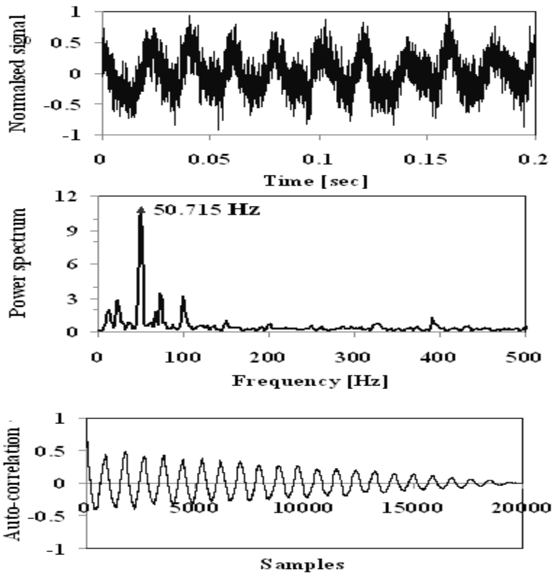

Figure 5.Power spectrum wave form, and Auto-correlation of sample taken after transition.

To compare between the general acoustic behaviour of premixed and diffusion flame, the power spectrum of the sample taken at the time when premixed flame was used, was superimposed on the power spectrum of the sample taken when diffusion flame was used. as shown in Figure 6.

From Figure 6 it is apparent that the power spectrum of the signal sample taken after humming has higher peaks, what this means is that the signal is more pure, or contains less noise than the signal taken before humming. From this it can be deduced that combustion at lean premixed conditions is noisier and less stable than combustion with a diffusion flame type.

Figure 6.Power spectra of samples taken after, before and at transition.

4. Conclusions

After the analysis of the results, a few conclusions were reached, the most important of which is the great effect thermo-acoustic instabilities have, on the performance and expected life span of turbo-machinery, this effect was encountered during the form of the humming phenomenon that occurred at the Al Rouweas GT power plant, the problems arising from the humming phenomenon that occurred when the combustion frequency matched the natural frequency of the power plant (experimentally found to be 72.765 Hz), were addressed via the application of passive control, which involved the switch from premixed to diffusion flame type.

Engineers at the power plant have found a solution that helped reduce the occurrence of the humming problem, since two of the fuel pre-heaters were offline the fuel's inlet temperature was lower than the design temperature of 20 ^{o}C, the offline fuel pre-heaters were repaired and reinstated, this increased the inlet fuel temperature back to 20 ^{o}C, the increased inlet fuel temperature caused a dramatic change in the repetitiveness of the humming phenomenon, from an almost daily occurrence, to a near weekly occurrence. The cause of this change is unknown and should be the centre of future research.

Acknowledgments

The authors wish to thank General Electric Company of Libya (GECOL) for their Help of this work, and also the contributions of Engineers Abouzeid. M. Nasser, Hisham. R. Abusorra from Al-Fateh University and Engineer Loutfi from Al Rouweas power plant.

Reference

[1] Rayleigh, Lord. "The explanation of certain acoustic phenomena," Natural, Vol. 18, 1878. 319-321.

[2] A. A. Putnam, and W. R. Dennis. "Burner Oscillation of the Gauze-Tone Type," *The* Journal of the Acoustical Society of America, Vol. 26 ,1954, 716-725.

[3] W. Lang,, T. Poinsot, and S. M. Candel. "Active Control of Combustion Instability." Combustion and Flame Vol. 70, 1987, 281-289.

[4] G. J. Bloxsidge, A. P.Dowling, N. Hooper, and P. J. Langhorne. "Active Control of an Acoustically Driven Combustion Instability." Journal of Theroetical and Applied Mechanics, vol. 6. 1987

[5] K. R. McManus, U. Vandsburger and C. T. Bowman. "Combustor Performance Enhancement through Direct Shear Layer Excitation." *Combustion and Flame* Vol. 82, 1990, 75–92.

[6] K. R. McManus, T. Poinsot and S. M. Candel. "A review of Active Control of Combustion Instabilities" Prog. Energy Combust. Sci. Vol. 19, 1993, 1-29.

[7] A. Gulati and R. Mani. "Active Control of Unsteady Combustion-induced Oscillations." Journal of Propulsion and Power Vol. 8(5), 1992, 1109–1115.

[8] S. Sivasegaram and H. W. Jhitelaw. "Active control of oscillations in combustors with several frequency modes." Proceedings of the ASME Winter Annual Meeting Anaheim, CA. 1992

[9] G. Billoud, M. A Galland, C. Huynh Huu and S. Candel. "Adaptive Active Control of Combustion Instabilities." Combust. Sci. and Tech. , Vol. 81, 1992, 257–283.

[10] E. Gutmark, T. P. Parr, K. J., Wilson, D. M. Hanson-Parr and K. C. Schadow. "Closed-Loop Control in a Flame and a Dump Combustor." IEEE Control Systems Vol. 13, 1993, 73–78.

[11] A. Kemal and C. T. wman. "Active Adaptive Control of Combustion." Proceedings of the IEEE Conference on Control Applications, Albany, NY, 1995, 667–672.

[12] T. Poinsot, F. Bourienne, S. Candel, and E. Esposito. "Suppression of Combustion Instabilities by Active Control." Journal of Propulsion and Power, Vol. 5(1), 1989, 14–20.

[13] M. A. Heckl. "Non-Linear Acoustic Effects in Rijke Tube", ACUSTICA Vol. 72, 1990, 63-71

[14] A. M. Annaswamyy, M. Fleifily, J. W. Rumseyz, R. Prasanthx, J. P. Hathouty and A. F. Ghoniemy. "Thermoacoustic Instability: Model-based Optimal Control Designs and Experimental Validation." IEEE Tans. Contr. Syst. Technol. Vol. 8, 2000, 905-918.

[15] G. A Richard,. M. J. Yip, E. Robey, L. Cowell, and D. Rawlins,. "Combustion Oscillation Control by Cyclic Fuel Injection," *Transactions of the ASME,* (1997) 119: 340-343.

[16] J. Hermann, A. Orthmann and S. Hoffmann. "Application of Active Combustion Control to Heavy-duty Gas Turbines." 14th Int. Symposium on Airbreathing Engines, Italy, 1999, 5-10.

[17] D. L. Gysling, G.S. Copeland, D. C. McCormick and W. M. Procia. "Combustion System Damping Augmentation With Helmholtz Resonators," Journal of Engineering for Gas Turbines and Power, Vol. 122(2), 2000, 269-274.

[18] K. C. Schadow and E. Gutmark. "Combustion Instability Related to the Vortex Shedding in Dump Combustors and their Passive Control," Progress in Energy and Combustion Science, Vol. 18, 1992, 117-132

[19] R.C. Steele. "Passive Control of Combustion Instability in Lean Premixed Combustors," ASME (99-GT-052). Indianapolis, IN, 1999.

[20] D.L. Straub and G.A. Richards. "Effect of Fuel Nozzle Configuration on Premix Combustion Dynamics," ASME 98-GT-492. Stockholm, Sweden, 1998.

[21] C.E. Smith and S.M. Cannon. "CFD Assessment of Passive and Active Control Strategies for Lean, Premixed Combustors." AIAA 99-0714. Reno, NV , 1999.

JJMIE
Volume 4, Number 3, June 2010
ISSN 1995-6665
Pages 358 - 363
Jordan Journal of Mechanical and Industrial Engineering

Theoretical Analyses of Energy Saving in Indirect Contact Evaporative Crystallization by Using Combined Cycle of Vapor Recompression Heat Pump and Throttling Valve

Adnan M. Al-Harahsheh*

Chemical Engineering Department, Mutah University, P.O. Box 7,Karak 61710,Jordan

Abstract

The installation of heat pumps in different chemical processes is considered as an important and prospective approach for energy saving. Various crystallization processes such as counter current crystallization, direct and indirect contact crystallization, evaporative crystallization and fractional crystallization from melts are used to be a promising chemical processes where heat pumps can be introduced for the purpose of energy saving. Usually in such processes, two zones are present; a cooling zone, where heat must be removed from the process and a heating zone, where heat must be added to the process. This work presents a theoretical analysis of the technical feasibility and the potential of heat pumps to be used in the process of indirect contact evaporative crystallization. Principle schemes of the process with heat pump and in combination with throttling valve are proposed and the corresponding calculations are performed. The Effect of temperature and initial feed concentration on the energy saving factor are investigated. The average value of this factor was estimated to be 49.6 % when a cooled feed solution enters (T =25 ^oC) to the crystallizer. This factor was found to be increased to 70.4 % when the feed solution inters at its boiling point (T=125 ^oC).The installation of throttling valve at the outlet of the condensate produces (based on feed conditions) an additional amount of vapor and as a result the saving factor increases from 17 % to 22 % .

Keywords: heat pumps; energy saving; crystallization

Nomenclature

F	Feed solution (kg/s)
K	Crystal phase(kg/s)
M	Mother liquor(kg/s)
D	Suspension phase(kg/s)
V_o	Produced vapor(kg/s)
X_F	Salt concentration in feed solution (%)
X_K	Salt concentration in crystal phase (%)
X_M	Salt concentration in mother liquor (%)
X_D	Salt concentration in suspension phase (%)
Xv_o	Salt concentration in vapor phase (%)
φ_{Vo}	Yield of vapor phase (%)
φ_D	Yield of suspension phase (%)
$h_F, h_{Vo}, h_D, h_K, h_M$	Specific enthalpy of feed, primary vapor , suspension, crystal & mother liquor phases (kJ/kg)
h_{Kf}	Specific latent heat of crystallization. (kJ/kg)
Q_C	Heat required for heating the feed solution (kJ/s)
Q_s	heat introduced to the system by heating steam (kJ/s)
T_F	Feed temperature (^oC)
T_b	Solution boiling point temperature(^oC)
S	Input heating steam of crystallizer (kJ/s)
C_F	Heat capacity of feed solution (kJ/kg ^oC)
S_o	Fresh make up steam (kJ/s)
H_{Vo}	Specific latent heat of vaporization(kJ/kg)
H_{in}	Specific enthalpy of heating steam at the inlet of crystallizer (kJ/kg)
H_{out}	Specific enthalpy of heating steam at the outlet of crystallizer (kJ/kg)
P_a	Actual power required for heat pump (kJ/s)
h_o, h_i	Specific enthalpy of vapor, at the inlet and out let of heat pump compressor (kJ/s)
η	Overall efficiency coefficient (%)
α	Ratio of salts concentrations in both feed & suspension phase (%)
V_{th}	Vapor produced as a result of throttling process (kJ/s)
L	Water produced as a result of throttling process (kJ/s)
h_L	Enthalpy of water produced as a result of throttling process
E_e	Cost for recompression ($/h)
E_s	Cost of ordinary process ($/h)
E_{So}	Cost of heating steam (so) ($/h)
Saving factor	(%)

* Corresponding author e-mail: Adnan@Mutah.edu.jo

1. Introduction

Chemical processes are generally characterized as high energy consuming processes; therefore, the operating cost becomes a huge burden on different industries, particularly with the recent soaring prices of oil. Therefore the reduction of energy consumption in these processes is considered a very important factor in determining the economical feasibility of the whole process.

A significant saving in energy consumption can be achieved using heat pumps for various processes in chemical industry [1,2]. The concept of heat pumps depends on increasing the potential (temperature) of operating fluid to the value that would fit to be used in the given chemical process. In vapor recompression heat pump the consumption of electrical energy goes to convert the low potential vapor phase by means of pressurizing into vapor with high potential [3,4]. This operation requires approximately energy in one order less than that for production of the same high potential vapor from its initial liquid phase.

Heat pumps can be potentially used to reduce energy consumption in evaporation, distillation, rectification, and in various methods of crystallization. This can be achieved by using different means of pressurizing low potential operating fluids. Introduction of different types of heat pumps to such as processes reduces the energy consumption considerably. Verk et al [5] and Bsharat [6] reported that saving on energy consumption up to 47 % was obtained when Vapor recompression heat pump was introduced to distillation and water desalination processes. Saving of 34 % to 45 % was also achieved by introducing mechanical heat pump to counter current crystallization process [7]. Energy saving was also achieved by using heat pumps in direct contact evaporative crystallization [8,9].

The aim of the this work is to study the possibility of reducing energy demand for the process of continuous indirect contact evaporative crystallization by using a combined vapor recompression heat pump cycle and throttling valve.

2. Theoretical Background

A schematic diagram, as shown in Figure1 presents a flow diagram of indirect contact evaporative crystallization process using saturated steam as a heating agent. This process is used on a large scale in crystallization and separation of mineral salts from their aqueous solutions such as KCl , K_2CO_3, NaCl and $NaNO_3$, [10,11].The process is carried out in a single-effect crystallizer. Steam, with a flow rate of (S), heats the solution through a contact surface. The enthalpy of the steam is then changed from H_{in} at the inlet to H_{out} at the outlet. vapor amount (V_o) is then produced and directed to a condenser where it condensed and pure water is obtained. A suspension (D) consisting of a crystal phase (K) and mother liquor (M) are formed and separated in a separator at the end of the process.

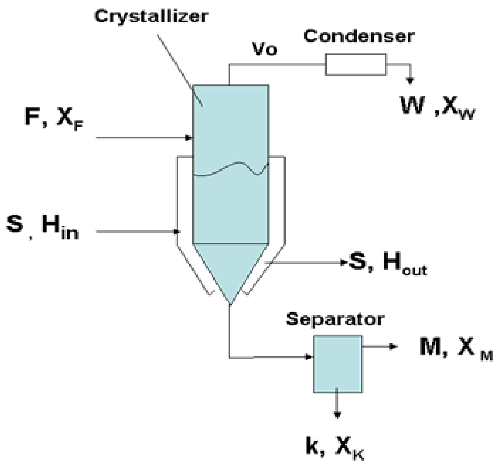

Figure 1: Principle scheme for indirect evaporative crystallization.

The overall material balance around crystallizer can be expressed as:

$$F = D + V_o \tag{1}$$

and

$$D = K + M \tag{2}$$

Balance on solute can be represented as:

$$FX_F = DX_D + V_o X_{Vo} \tag{3}$$

By substituting Eq . (2), in Eq.(3), Eq. (1) can be rewritten as:

$$FX_F = KX_K + MX_M + V_o X_{Vo} \tag{4}$$

Where $X_F, X_D, X_K, X_M, X_{Vo}$ are the salts concentrations in the feed solution (F), suspension (D), crystal (K), Mother liquor (M) and condensate (V_o) phases respectively.

Taking into account that the evaporated water contains zero amount of solute ($X_{Vo} = 0$) Then Eq. (4) became:

$$FX_F = KX_K + MX_M \tag{5}$$

The yield of vapor phase (condensate) and suspension phase can be calculated by solving Eq (1) and Eq. (2) simultaneously as follows:

$$\varphi_{Vo} = \frac{V}{F} = \frac{X_F - X_D}{X_{V_o} - X_D} \tag{6}$$

$$\varphi_D = \frac{D}{F} = 1 - \varphi_{Vo} = \frac{X_{Vo} - X_F}{X_{V_o} - X_D} \tag{7}$$

or

$$X_D = \frac{X_F - X_{Vo}\varphi_{Vo}}{1 - \varphi_{Vo}} \tag{8}$$

If the volatility of solute is assumed to be zero or $X_{Vo} = 0$, then Eq. (6, 7 and 8) became as follows:

$$\varphi_{Vo} = \frac{X_F}{1 - X_D} \tag{9}$$

$$X_D = \frac{X_F}{1-\varphi_{Vo}} \tag{10}$$

$$\varphi_D = \frac{X_F}{X_D} \tag{11}$$

The energy balance around crystallizer is calculated by**:**

$$Fh_F + Q_s = Vo.h_{Vo} + Dh_D + Kh_{K\,f} \tag{12}$$

Where, h_F, h_{Vo}, h_D are the enthalpies of feed solution, primary vapor, and the suspension respectively. $h_{K\,f}$ is the latent heat of crystallization and Q_s is the introduced heat to the system by heating steam. The heat content of the suspension can be represented as:

$$Dh_D = Kh_K + Mh_M \tag{13}$$

The heat required for heating feed solution Q_C from its feed temperature T_F to its boiling point temperature inside the crystallizer T_b is estimated by the following equation:

$$Q_C = C_F F(T_b - T_F) \tag{14}$$

Where C_F is the heat capacity of the feed solution. The amount of heating steam for Heating and evaporating stages is calculated by:

$$S = \frac{V_o H_{Vo} + Q_C}{H_{in} - H_{out}} \tag{15}$$

Where H_{Vo} is the latent heat of vaporization.

3. Application and Calculations

3.1. Indirect evaporative crystallization with vapor recompression heat pump:

In order to minimize the amount of the energy required to carry out the above mentioned crystallization process, a heat pump is proposed to be used as shown in Figure 2. The stream of the primarily formed vapor is directed to a heating chamber after enhancing its potential by increasing its pressure from P_1 to P_2 by using vapor recompression heat pump.

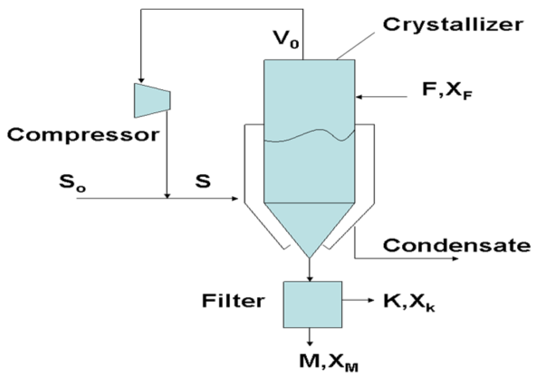

Figure 2: Principle scheme for indirect evaporative crystallization with heat pump.

Thus the required hot fresh steam will be decreased. The amount of this steam can be estimated as:

$$S_o = S - V_o \tag{16}$$

Taking into account Eq (1) & Eq (3) and Solving for V_o:

$$V_o = F(1-\alpha) \tag{17}$$

Where,

$$\alpha = \frac{X_F}{X_D} \tag{18}$$

The actual power P_a (kW) required for heat pump:

$$P_a = \frac{Vo(h_1 - h_o)}{1000\eta} \tag{19}$$

Where and are the enthalpies of vapor, before and after recompression respectively is the overall efficiency coefficient of the compressor.

In order to examine the efficiency of using a heat pump in the indirect evaporative crystallization, a sample of calculation was carried out for a single effect crystallizer with continuous concentration of K2CO3 solution. The rate of the initial solution was 1000 kg/hr, concentration 10 % (mass), and the final concentration was 60 % (mass). The temperature of the heating steam was 150 ^oC, the pressure inside the crystallizer 1 atm and the final boiling temperature of the solution in the crystallizer was 125 ^oC. Calculations were performed for the following three variants:

- The solution is fed to crystallization process at an initial temperature of 25 ^oC.
- The solution is fed to crystallization process at its boiling point.
- The solution is fed to crystallization process superheated to 135 ^oC

The process of crystallization, was assumed to be ideal, therefore the crystal phase forms according to the theoretical phase diagram of the feed solution.

3.2. Indirect evaporative crystallization with a combined cycle of Vapor recompression and throttling valve:

A modified scheme of the process is shown in Figure 3, where a throttling valve is introduced at the outlet of condensate in order to obtain additional vapor V_{th} by directing the condensate through this valve. As a result, part of this condensate will be changed into vapor. Then, this vapor is mixed with the primary vapor and directed after recompression to the heating chamber.

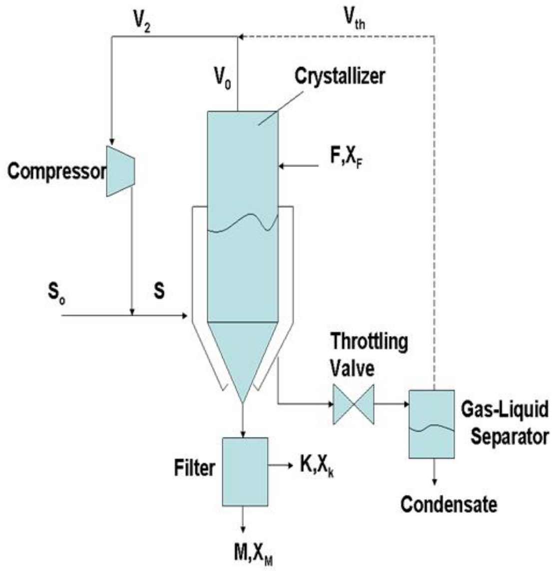

Figure 3: Principle scheme for indirect evaporative crystallization with heat pump and throttling valve.

The amount of V_{th} can be estimated by calculating the energy balance around a throttling valve as follows:

$$SH_{out} = V_{th}h_{th} + Lh_L \tag{20}$$

$$L = S - V_{th} \tag{21}$$

Solving for V_{th}:

$$V_{th} = S\frac{(H_{out} - h_L)}{(h_{th} - h_L)} \tag{22}$$

Where H_{out} is the enthalpy of condensate at the outlet of crystallizer, h_L and h_{th} , are the enthalpies of liquid condensate and vapor after passing through a throttling valve respectively. In this case and as a result of the additional amount of stream of vapor V_{th} produced by a throttling valve, the required amount of make up of fresh steam will be reduced to the amount of:

$$S_o = S - V_o - V_{th} \tag{23}$$

4. Results and Discussions

To evaluate the efficiency of using a heat pump and a throttling valve in the proposed processes, the consumption of energy for the ordinary crystallization process (without heat pump) was calculated and compared to that with a heat pump. Calculation was performed based on the average cost of electrical energy (0.05 \$/k.W.h) and low pressure steam (3.17x 10-6 \$/kJ) Europe prices [12].

The consumption of electrical energy E_e was estimated according to the operating conditions of vapor recompression process as shown in Fig. 4. The saving factor is defined according to [7] as:

$$Saving\ factor = \left(1 - \frac{Cost\ of\ energy\,consumption\ with\ heat\ pump}{Cost\ of\ energy\,consumption\ without\ heat\ pump}\right) \times 100\% \tag{24}$$

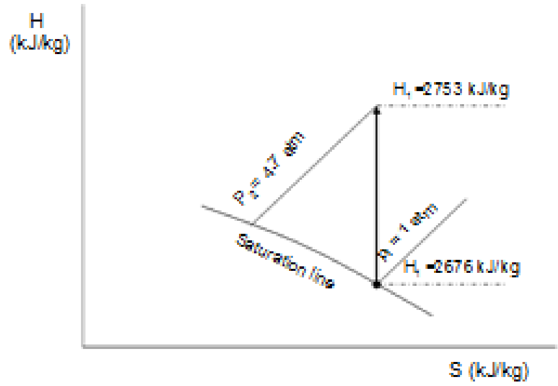

Figure 4: S-H diagram for vapor recompression process.

This factor depends on some of the process variables such as: feed temperature and concentration. The value of this factor was found to be 49.6 %, 70.4 % and 69.7 % for the variants when the feed inters at 25 ^oC, 125 ^oC (boiling point) and 135 ^oC (superheated), respectively.

The maximum saving factor was achieved when the feed enters at its boiling point as illustrated in Figure 5. This can be explained due to the fact that, additional amount of heating steam is needed when the feed solution is cooled. However, when the feed was superheated, an extra amount of vapor was produced.

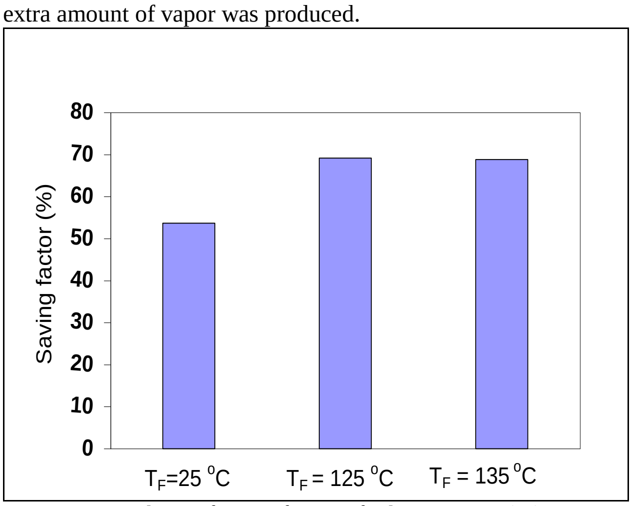

Figure 5: Dependency of saving factor at feed temperature (T_F).

The effect of initial feed concentration on saving factor and on other process variables was also studied. Table.1 show a selected results of calculation for a process when feed concentration was varied from 10 to 60 (wt %), at fixed feed temperature of 25 ^oC. The obtained data show a slightly decrease in saving factor when the initial feed concentration increases from 10 to 50 %, followed by a sharp decrease and reaches its zero value when the feed concentration reaches 60 % (Figure 6).This decrease is expected and can be explained based on the fact that the increase of feed concentration leads to a decrease in the production of primary vapor V_o which is directed to the heat pump. The value of this vapor goes to zero when the feed inters at concentration closed to saturation point 60 % (Figure 7).

Table 1: Selected results of calculations for K_2CO_3 solution (K_2CO_3 solution, F = 1000 kg/h , TF = 25 °C , Tb =125 °C).

X_F (%)	10 %	20 %	30 %	40 %	50 %	60 %
V_o (kg/h)	833.3	666.7	500.0	333.3	166.6	0
S_o (kg/h)	426.7	364.7	298.9	233.2	167.5	101.6
S (kg/h)	1260.0	1031.4	798,9	566.5	334.1	101.6
E_{so} ($/h)	3.05	2.60	2.14	1.66	1.19	0.72
E_e ($/h)	1.13	0.87	0.615	0.36	0.15	0
E_s ($/h)	9.01	7.37	5.71	4.05	2.38	0.72
Saving ($/h)	4.83	3,89	2.96	2.01	1.03	0
Saving factor (%)	53.6	52.8	51.8	49.8	43.5	0

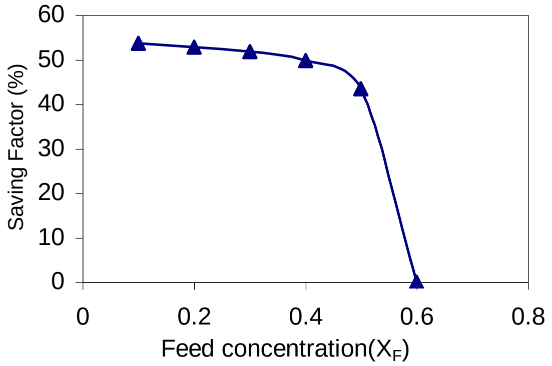

Figure 6: Dependency of saving factor on feed concentration (X_F).

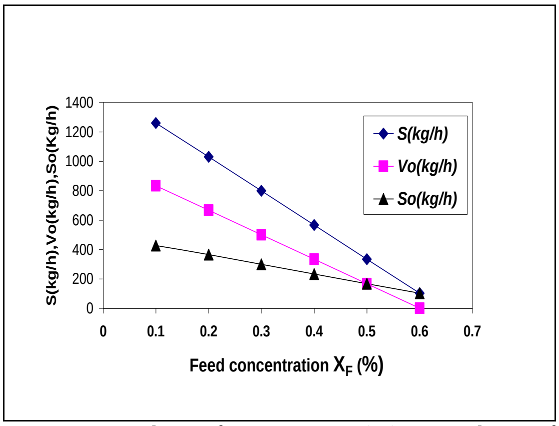

Figure 7: Dependency of primary vapor (V_o), required steam for ordinary process (S) and for a process with heat pump (S_o) on feed concentration (X_F).

Furthermore data illustrated in Figure 7 show that the total required steam for the process with heat pump (S_o) comparing to that without heat pump (S), was reduced by the value equal to the amount of the produced primary vapor. Calculations show that when a throttling valve was installed in combination with a heat pump, an additional saving of 17-22 % (based on initial feed concentration) was achieved.

5. Conclusions

Installation of vapor recompression heat pump in indirect evaporative crystallization process can save energy. The principle schemes and analysis of such process are illustrated in this study. The effect of feed temperature and concentration are analyzed and the energy saving factor was determined. This factor, was found to be in the range of 43 to 71 % based on the entrance feed conditions (temperature & concentration).The combination between vapor recompression heat pump and throttling valve (installed at the outlet of condensate), was found to be produced (based on feed conditions) an additional saving of 17 to 22 %.

References

[1] W. Wongsuwan, S. Kumar, P. Neveu, F. Meunier, "A review of chemical heat pump technology and applications". Applied Thermal Engineering, Vol. 21, Issue 15, 2001, 1489-151.

[2] A.Hepbasli, Y. Kalinci, "A review of heat pump water heating systems" Renewable and Sustainable Energy Reviews, Vol. 13, Issues 6-7, 2009, 1211-1229.

[3] S. Chaturvedi, T. Abdel-Salam, S. Sreedharan, F.B. Gorozabel, "Two-stage direct expansion solar-assisted heat pump for high temperature applications".Applied Thermal Engineering, Vol. 29, Issue 10, 2009, 2093-2099.

[4] C. Zamfirescu, I. Dincer, "Performance investigation of high-temperature heat pumps with various BZT working fluids". Thermochimica Acta, Vol. 488, Issues 1-2, 2009, 66-77.

[5] G. S.Virk , M. Ford, B. Dennes, A. Ridett, and A. Hunter, "Ambient Energy For Low-Cost Water Desalination ". Desalination, Vol.137, 2001,149-156.

[6] G. Bsharat, "Vapor Recompression Can Save Energy in Distillation". mu'tah lil-buhuth wa- derasat, vol.18,issue1, 2003,117-129.

[7] A. Al-Harahsheh, "A heat pump in a countercurrent crystallization process", Applied Thermal Engineering, Vol.25, issue 4, 2005, 545-555.

[8] Al-harahsheh, "A heat pump in a direct contact evaporative crystallization can save energy". heat-Set 2005 conference, Grenoble France ,2005.

[9] A. Al-harahsheh "Theoretical analyses of energy saving in a direct contact evaporative crystallization through the installation of heat pump ". Desalination, corrected proof, 2009

[10] J. Mullin. Crystallization, Ltd.3rd Ed . MPG Book, London.2000.

[11] N. Gelparen, G. Nosov. Fundamentals of fractional crystallization techniques, Chemistry publisher, 1st Ed., Moscow (in Russian),1986.

[12] L. Ying and P. Flynn, "Deregulated power price comparison of diurnal patterns", Energy policy, Vol. 23,2004, 657-672.

JJMIE

Volume 4, Number 3, June, 2010
ISSN 1995-6665
Pages 364 - 371

Jordan Journal of Mechanical and Industrial Engineering

Studies On $\overline{X}$ - Control Chart With Pareto In-Control Times for Non Normal Variates

Neelufur [a,*], K.Srinivasa Rao [b], K. Venkata Subbaiah[c]

[a] Department of Industrial Production Engg., GITAM University, Visakhapatnam-45, INDIA

[b] Department of Statistics, Andhra University,Visakhapatnam-03, INDIA

[c] Department of Mechanical Engg., Andhra University,Visakhapatnam-03, INDIA

Abstract:

In this paper we develop and analyse economic statistical design of $\overline{X}$ control chart with the assumption that the sample average of the quality characteristic (follows a Johnson distribution and the process in-control times follow Pareto distribution. The Johnson distribution is generally taken for all types of skewed and kurtic variables. Here, the Pareto distribution is chosen since in many production processes at places like Fertilisers, chemicals, etc., the in-control times are having long upper tail and suits to the Pareto distribution. The expected cost per a unit time is derived with the use of the cost model developed for the $\overline{X}$ control chart. Minimizing the expected cost per a unit time, the optimal design parameters like sample size and the time interval between two successive samples are derived for given Type I and Type II errors associated with the control chart. The sensitivity of the model with respect to the parameters and costs are also studied. This design is extended to the case when the time to search for an assignable cause and time to repair are also random and follow a Weibull distribution. The effect of randomness on these times is also investigated.

Keywords: $\overline{X}$ Control Chart;In-Control Times;Out Of Control Times;Johnson Distribution;Expected Cost Per Unit Time.

Notations:

S = Expected number of samples taken during the in-control state.
ARL_0= Average run length when process is in control
ARL_1= Average run length when process is out of control
h = Time interval between successive samples
k = Number of standard deviations from control limits to centre line
Δ = Number of standard deviations slip when out of control
n = Sample size
E = Expected sampling time for one observation
δ_1= Indicator variable to indicate whether production continues or not during the assignable cause search, $\delta_1=1$ if production continues and $\delta_1=0$, otherwise
δ_2= Indicator variable to indicate whether production continues or not during the repair process, $\delta_2=1$ if production continues and $\delta_2=0$, otherwise
T_0= Expected assignable cause search time for a false alarm
T_1= Expected time to identify the assignable cause
T_2 = Expected time to repair the process
a = Fixed cost per sample
b = Variable cost per sample
C_0 = Hourly cost due to nonconformities produced while the process is in control
C_1 = Hourly cost due to nonconformities produced while the process is out of control ($C_1 > C_0$)
C_2 = Cost per false alarm
W = Cost for locating and repairing the assignable cause
α = Probability that $\overline{X}$ falls outside the control limits when the process is in control
β= Probability that $\overline{X}$ falls within the control limits when the process is out of control
E(C) = Expected Cycle cost
E(T) = Expected Cycle time

* Corresponding author. neelufur2000@yahoo.com.

1. Introduction:

For the excellence in productivity, one has to concentrate on the quality improvement programs. The major issue of achieving excellence in quality depends on Quality control. One of the important techniques adopted for process control is $\bar{X}$ control chart. With the help of Central limit theorem, many researchers considered that the sample mean of the quality characteristic follows normal distribution[1]. However, this assumption is suitable only when the sample size is large. But in many practical situations, the sample size of the quality character is small and the normal assumption leads to error. Taking this concept into consideration several researchers developed $\bar{X}$ control charts and statistical economic design with various distributions [2-6].

Recently Huifen Chen and Yuyen Cheng [7] have considered the economic statistical design of $\bar{X}$ chart with the assumption that the sample average, $\bar{X}$ of the quality character follows Johnson distribution. Their cost model was based on the model proposed by Mc Williams [8], which is an extension of the work of Lorenzen and Vance [9]. They emphasised the need of utilising Johnson distribution as $\bar{X}$ distribution. They have also assumed that the in-control times of the process follow a Weibull distribution. One of the major drawbacks of the two parameter Weibull distribution is that it considers the failure starts from zeroth time. In many practical situations once the process is put in control it may take a minimum period to failure. Hence it is reasonable to consider a distribution for the process in-control times which characterize this property. One such distribution often used in reliability and life testing is Pareto distribution.

The Pareto distribution also characterizes a limiting distribution of the waiting time (time to exceed a specific value of the process character). This distribution is named after an Italian, Vilfredo Pareto (1848-1923). It is also empirically observed that in Chemical industries, the in-control times of the process are having left – skewed with long upper tail depicting the frequency distribution of Pareto. Very little work has been reported in literature regarding the Economic design of $\bar{X}$ control chart with Pareto in-control times even though this distribution is quite common in many Manufacturing and Production processes. Hence in this article , we develop and analyze the Economic statistical design of the $\bar{X}$ control chart with the assumption that the quality characteristic $\bar{X}$ follows Johnson distribution with mean 'μ' and variance 'σ^2' and the in control times of the process are random and follows a Pareto distribution with probability density function of the form,

$$f(t) = \{c.\theta^c.t^{-(c+1)}\}, (\theta > 0,\ c > 0,\ t \geq \theta) \quad (1)$$

The Pareto Cumulative distribution function is

$$F(T) = \left\{1 - \left(\frac{\theta}{t}\right)^c\right\}, (\theta > 0,\ c > 0,\ t \geq \theta) \quad (2)$$

where, 't' is the in-control time, 'θ' is the parameter of Pareto distribution, 'c' is the shape parameter and its mean is $\left(\frac{c.\theta}{c-1}\right)$ [10]. The various shapes of the Pareto distribution frequency curves for different values of the parameter, 'c' are shown in Figure1.

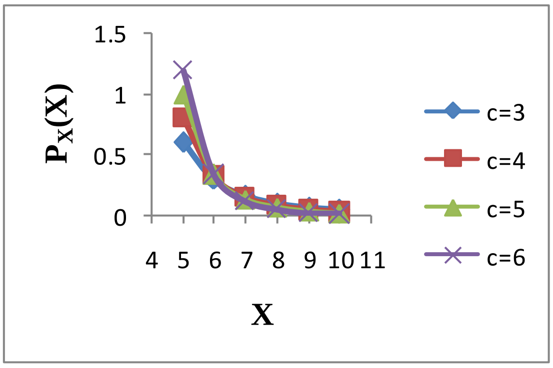

Figure 1. Pareto Distribution Frequency curves (Θ=5)

The expected hourly cost equals the ratio of the expected cycle cost to the expected cycle time. The schematic diagram of a Production cycle is shown in Figure2 as given by Lorenzen and Vance [9].

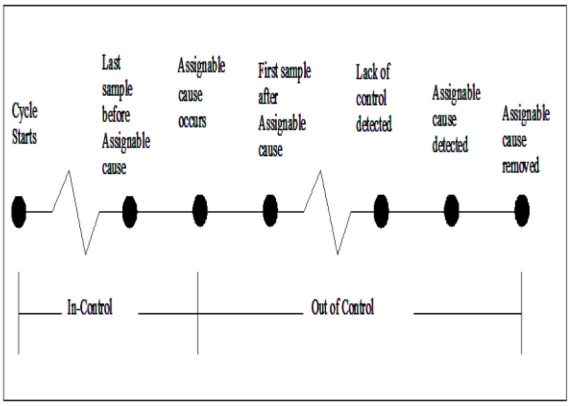

Figure 2. Production Cycle

The optimal design parameters of the $\bar{X}$ control chart namely, the Sample size (n) and the Sampling interval (h) are derived by minimizing the expected cost per unit time. The sensitivity of the model with respect to the parameters and costs is also studied. This model is extended to the case when the out of control times (the time to identify assignable causes and time to repair) are also random and follows Weibull distribution.

2. Cost Model

The production process is assumed to start in an in-control state. In order to detect a shift in the process mean, a sample of 'n' independent quality characteristic measurements $X_1, X_2, X_3 \ldots X_n$ is taken at intervals of 'h' hours. The sample average $\bar{X}$ is assumed to have Johnson distribution. Johnson family, proposed by Normanl Johnson [10], includes three transformations of the standard normal distribution. Let Y and X denote the Johnson and standard normal variables, respectively. We use the transformation

$$X = \gamma + \delta \ln\left(\frac{Y-\xi}{\xi+\eta-Y}\right), 0 \leq (Y-\xi) \leq \eta, \quad (3)$$

The constants 'ξ' and 'η' are location and scale parameters, 'γ' and 'δ' are the shape parameters. To compute the Johnson cumulative probability F(y) = P{Y ≤ y}, we transform Y to X using Equation (3) and then let F(y) = Φ(x), where 'Φ' is the standard normal cumulative distribution function. Here, Y is taken as a bounded normal distribution. Hence,

$$F_{\mu}(y) = \Phi\left[\gamma + \delta \ln\left(\frac{Y-\xi}{\xi+\eta-Y}\right)\right] \quad (4)$$

where, $F_{\mu}(\,.\,)$ is the Johnson cumulative distribution function with mean, 'μ' and standard deviation, $\frac{\sigma}{\sqrt{n}}$.

For independent observations , average run lengths when the process is in control and out of control i.e., ARL_0 and ARL_1 respectively are related to Type I and Type II error probabilities, 'α' and 'β' as follows :

$$ARL_0 = 1 / \alpha$$

where,

$$\alpha = P\{\bar{X} < \mu_0 - k\sigma/\sqrt{n} \text{ or } \bar{X} > \mu_0 + k\sigma/\sqrt{n} \mid \mu = \mu_0\}$$

$$= 1 + F_{\mu_0}\left(\mu_0 - \frac{K\sigma}{\sqrt{n}}\right) - F_{\mu_0}\left(\mu_0 + \frac{K\sigma}{\sqrt{n}}\right) \quad (5)$$

and $ARL_1 = 1 / (1-\beta)$

where,

$$\beta = P\{\mu_0 - k\sigma/\sqrt{n} \le \bar{X} \le \mu_0 + k\sigma/\sqrt{n} \mid \mu = \mu_0 + \Delta\sigma\}$$

$$= F_{\mu_0+\Delta\sigma}\left(\mu_0 + \frac{K\sigma}{\sqrt{n}}\right) - F_{\mu_0+\Delta\sigma}\left(\mu_0 - \frac{K\sigma}{\sqrt{n}}\right) \quad (6)$$

The $\bar{X}$ control chart is designed to detect whether the process is out of control or not.

The design parameters 'n' and 'h' are chosen to minimize the expected cost per a unit time i.e., E(C)/E(T). A quality cycle is defined as the time until the next in - control period. The in-control times in each cycle are identically and independently distributed. Hence, the expected hourly cost E(C/T) equals the ratio of the expected cycle cost to the expected cycle time.

From Figure2, the expected cycle time consists of 4 parts namely, (1) Expected time elapsed before assignable cause occurs , (2) Expected time between the occurrence of the assignable cause and the next out of control signal, (3) Expected time 'T_1' to identify the assignable cause and (4) Expected time 'T_2' to repair the process. In this model it is assumed that the process in-control times follow Pareto distribution with mean, $\left(\frac{c.\theta}{c-1}\right)$ and the in-control times in each cycle are independently identically distributed with probability density function of the form given in Equation (1). Therefore, the expected time elapsed before the assignable cause occurs, when the production ceases during the search for an assignable cause, is the mean of the in-control times plus the time spent searching during false alarms.

The expected time spent during false alarms is 'T_0' times the expected number of false alarms

$$= \frac{T_0.S}{ARL_0} \quad (7)$$

where, 'T_0' is the expected search time for a false alarm,

'S' is the expected number of samples taken while in control and

'ARL_0' is the average run length while in control.

We have,

$$S = \sum_{i=0}^{\infty} i * pr(\text{assignable cause occurs between the } i^{th} \text{ and } (i+1)^{th} \text{samples})$$

$$= \sum_{i=0}^{\infty} i\left[\left(\frac{\theta}{i.h}\right)^c - \left(\frac{\theta}{(1+i).h}\right)^c\right] \quad (8)$$

where, $\left\{1 - \left(\frac{\theta}{t}\right)^c\right\}$ is the cumulative distribution function of Pareto distribution (in-control time) as given in Equation (2).

If the process is shut down during searches, the expected time equals to

$$\left(\frac{c.\theta}{c-1}\right) + \frac{T_0.S}{ARL_0}$$

Let δ_1=1 if production continues during searches and δ_1=0 if production ceases during searches.

Hence, the expected time until the assignable cause occurs is

$$\left(\frac{c.\theta}{c-1}\right) + \frac{[(1-\delta_1).T_0.S]}{ARL_0}$$

$$= \left(\frac{c.\theta}{c-1}\right) + (1-\delta_1).T_0.S.\alpha \quad (9)$$

The total number of samples taken is the sum of expected number of samples taken during the in control time (S), plus the number of samples when the process has gone out of control (ARL_1)

$$= (S + ARL_1)$$

The time interval between sampling is 'h'. Hence, the total time period for taking ($S+ARL_1$) samples is

$$= (S + ARL_1).h$$

But, the samples are being taken out every 'h' hours irrespective of whether the process is in or out of control. Here, we require only the time period between the occurrence of assignable cause and the next out of control signal which is simply the total time period minus the mean time of in control state.

It is assumed that the in control times follow Pareto distribution with mean $\left(\frac{c.\theta}{c-1}\right)$.

Hence, the required time is

$$(S + ARL_1).h - \left(\frac{c.\theta}{c-1}\right)$$

As 'E' is the expected time for measuring each observation, for a sample of 'n' items, the time to analyze the sample and chart the result is 'nE'. Hence the total expected time between the occurrence of assignable cause and the next out of control signal is

$$(S + ARL_1).h - \left(\frac{c.\theta}{c-1}\right) + n.E$$

$$= \left(S + \frac{1}{(1-\beta)}\right).h - \left(\frac{c.\theta}{c-1}\right) + n.E \quad (10)$$

As 'T_1' is the expected time to identify the assignable cause and 'T_2' is the expected time to repair the process, the total time required when the process is out of control is

$$\left(S + \frac{1}{(1-\beta)}\right).h - \left(\frac{c.\theta}{c-1}\right) + n.E + T_1 + T_2 \quad (11)$$

Therefore, from Equations (9) & (11) the expected cycle time is

$$E(T) = \left(\frac{c.\theta}{c-1}\right) + (1-\delta_1).T_0.S.\alpha + \left(S + \frac{1}{(1-\beta)}\right).h - \left(\frac{c.\theta}{c-1}\right) + n.E + T_1 + T_2$$
$$= (1-\delta_1).T_0.S.\alpha + \left(S + \frac{1}{(1-\beta)}\right).h + n.E + T_1 + T_2 \quad (12)$$

The cost of the entire cycle includes (1) Cost of non conformities, (2) Cost of false alarms, (3) Expected cost for sampling and charting the result and (4) Cost of repairs, 'W'.

Let C_0 = Hourly cost due to nonconformities produced while the process is in control and

C_1 = Hourly cost due to nonconformities produced while the process is out of control ($C_1 > C_0$)

Assuming that the production continues during both search and repair, the expected cost per cycle due to non conformities

$$= C_0\ (\text{Mean in control time}) + C_1\ (\text{Total time required when the process is out of control})$$
$$= C_0\left(\frac{c.\theta}{c-1}\right) + C_1\left\{\left(S + \frac{1}{(1-\beta)}\right).h - \left(\frac{c.\theta}{c-1}\right) + n.E + T_1 + T_2\right\}$$
$$= C_0\left(\frac{c.\theta}{c-1}\right) + C_1\left\{\left(S + \frac{1}{(1-\beta)}\right).h - \left(\frac{c.\theta}{c-1}\right) + n.E + \delta_1 T_1 + \delta_2 T_2\right\} \quad (13)$$

where, 'δ_1' and 'δ_2' are as defined earlier.

The expected number of false alarms $= \dfrac{S}{ARL_0}$

The expected cost of false alarms

$$= C_2.\left(\frac{S}{ARL_0}\right) = C_2.S.\alpha \quad (14)$$

where, 'C_2' is the cost per false alarm.

Since the fixed cost per sample (a) and the variable cost per sample (b) are considered to effect the total cost, the expected cost for sampling and charting the result is given by (a+b.n) times the total time producing divided by the time interval between sampling

$$= \frac{(a+b.n)}{h}.\left\{\left(S + \frac{1}{(1-\beta)}\right).h + n.E + \delta_1.T_1 + \delta_2.T_2\right\} \quad (15)$$

From Equations (13), (14) and (15), we have,

The Expected cycle cost is,

$$E(C) = C_0\left(\frac{c\theta}{c-1}\right) + C_1\left\{\left(S + \frac{1}{(1-\beta)}\right).h - \left(\frac{c\theta}{c-1}\right) + n.E + \delta_1.T_1 + \delta_2.T_2\right\} + C_2.S.\alpha + \frac{(a+b.n)}{h}.\left\{\left(S + \frac{1}{(1-\beta)}\right).h + n.E + \delta_1.T_1 + \delta_2.T_2\right\} + W \quad (16)$$

in the design of $\bar{X}$ chart , the design parameters 'n' and 'h' are chosen to minimize the expected cost per hour 'Z' for a quality cycle where,

$$Z = E(C)/E(T) \quad (17)$$

Substituting the Equations (12) and (16) in Equation (17), we get,

$$Z = \left\{C_0\left(\frac{c\theta}{c-1}\right) + C_1\left\{\left(S + \frac{1}{(1-\beta)}\right).h - \left(\frac{c\theta}{c-1}\right) + n.E + \delta_1.T_1 + \delta_2.T_2\right\} + C_2.S.\alpha + \frac{(a+b.n)}{h}.\left\{\left(S + \frac{1}{(1-\beta)}\right).h + n.E + \delta_1.T_1 + \delta_2.T_2\right\} + W\right\} \Big/ \left\{(1-\delta_1).T_0.S.\alpha + \left(S + \frac{1}{(1-\beta)}\right).h + n.E + T_1 + T_2\right\} \quad (18)$$

Where, 'α' and 'β' are as defined in Equations (5) and (6) respectively.

The optimum values for 'h' and 'n' are obtained by differentiating 'Z' with respect to 'h' and 'n' and equating them to zero.

Let

$$R = \frac{\partial s}{\partial h} = \frac{\partial}{\partial h}\left\{\sum_{i=0}^{\infty} i\left[\left(\frac{\theta}{i.h}\right)^c - \left(\frac{\theta}{(1+i).h}\right)^c\right]\right\}$$
$$= \sum_{i=0}^{\infty} \frac{\partial}{\partial h}\left\{i\left[\left(\frac{\theta}{i.h}\right)^c - \left(\frac{\theta}{(1+i).h}\right)^c\right]\right\}$$
$$= \sum_{i=0}^{\infty}\left[i.c.\theta^c.h^{-(c+1)}.\left(\frac{1}{(1+i)^c} - \frac{1}{i^c}\right)\right] \quad (19)$$

we have,

$$\frac{\partial[E(C)]}{\partial h} = C_1.\left[S + \frac{1}{(1-\beta)} + h.R\right] + C_2.\alpha.R + \frac{(a+b.n)}{h}.\left\{S + \frac{1}{(1-\beta)} + h.R\right\} - \frac{(a+b.n)}{h^2}.\left\{\left(S + \frac{1}{(1-\beta)}\right).h + n.E + \delta_1.T_1 + \delta_2.T_2\right\} \quad (20)$$

$$\frac{\partial[E(T)]}{\partial h} = S + \frac{1}{(1-\beta)} + h.R + (1-\delta_1).T_0.S.\alpha.R \quad (21)$$

Therefore, $\dfrac{\partial z}{\partial h} = 0$ implies,

$$\left\{E(T).\left\{C_1.\left[S + \frac{1}{(1-\beta)} + h.R\right] + C_2.\alpha.R + \frac{(a+b.n)}{h}.\left\{S + \frac{1}{(1-\beta)} + h.R\right\} - \frac{(a+b.n)}{h^2}.\left\{\left(S + \frac{1}{(1-\beta)}\right).h + n.E + \delta_1.T_1 + \delta_2.T_2\right\} - E(C).\left\{S + \frac{1}{(1-\beta)} + h.R + (1-\delta_1).T_0.S.\alpha.R\right\}\right\} \Big/ [E(T)]^2 = 0$$

This implies,

$$\left\{\left\{(1-\delta_1).T_0.S.\alpha + \left(S + \frac{1}{1-\beta}\right).h + n.E + T_1 + T_2\right\}.\left\{C_1.\left[S + \frac{1}{(1-\beta)} + h.R\right] + C_2.\alpha.R + \frac{(a+b.n)}{h}.\left\{S + \frac{1}{(1-\beta)} + h.R\right\} - \frac{(a+b.n)}{h^2}.\left\{\left(S + \frac{1}{(1-\beta)}\right).h + n.E + \delta_1.T_1 + \delta_2.T_2\right\}\right\} - \left\{C_0\left(\frac{c.\theta}{c-1}\right) + C_1\left\{\left(S + \frac{1}{(1-\beta)}\right).h - \left(\frac{c.\theta}{c-1}\right) + n.E + \delta_1.T_1 + \delta_2.T_2\right\} + C_2.S.\alpha + \frac{(a+b.n)}{h}.\left\{\left(S + \frac{1}{(1-\beta)}\right).h + n.E + \delta_1.T_1 + \delta_2.T_2\right\} + W\right\}.\left\{S + \frac{1}{(1-\beta)} + h.R + (1-\delta_1).T_0.S.\alpha.R\right\}\right\} \Big/ \left\{(1-\delta_1).T_0.S.\alpha + \left(S + \frac{1}{(1-\beta)}\right).h + n.E + T_1 + T_2\right\}^2 = 0 \quad (22)$$

Where, 'α' and 'β' are as defined in Equations (5) and (6) respectively.

And for optimal 'n',

$$\frac{\partial[E(C)]}{\partial n} = C_1.E + \frac{(a+b.n)}{h}.E + \left(\frac{b}{h}\right).\left[\left(S + \frac{1}{(1-\beta)}\right).h + n.E + \delta_1.T_1 + \delta_2.T_2\right] \quad (23)$$

$$\frac{\partial[E(T)]}{\partial n} = E \quad (24)$$

Therefore, $\dfrac{\partial z}{\partial n} = 0$ implies,

$$\left\{E(T).\left\{C_1.E + \frac{(a+b.n)}{h}.E + \left(\frac{b}{h}\right).\left[\left(S + \frac{1}{(1-\beta)}\right).h + n.E + \delta_1.T_1 + \delta_2.T_2\right]\right\} - E(C).E\right\} \Big/ [E(T)]^2 = 0$$

This implies,

$$\left\{\left\{(1-\delta_1).T_0.S.\alpha + \left(S + \frac{1}{(1-\beta)}\right).h + n.E + T_1 + T_2\right\}.\left\{C_1.E + \frac{(a+b.n)}{h}.E + \left(\frac{b}{h}\right).\left\{\left(S + \frac{1}{(1-\beta)}\right).h + n.E + \delta_1.T_1 + \delta_2.T_2\right\}\right\} - \left\{C_0\left(\frac{c.\theta}{c-1}\right) + C_1\left\{\left(S + \frac{1}{(1-\beta)}\right).h - \left(\frac{c.\theta}{c-1}\right) + n.E + \delta_1.T_1 + \delta_2.T_2\right\} + C_2.S.\alpha + \frac{(a+b.n)}{h}.\left\{\left(S + \frac{1}{(1-\beta)}\right).h + n.E + \delta_1.T_1 + \delta_2.T_2\right\} + W\right\}.E\right\} \Big/ \left\{(1-\delta_1).T_0.S.\alpha + \left(S + \frac{1}{(1-\beta)}\right).h + n.E + T_1 + T_2\right\}^2 = 0 \quad (25)$$

Where, 'α' and 'β' are as defined in Equations (5) and (6) respectively.

Solving the Equations (22) and (25) iteratively using numerical method the optimal sampling interval (h^*) and the optimal sample size (n^*) can be obtained for the given values of the model parameters and cost parameters

3. Sensitivity Analysis:

The sensitivity of the cost model is studied with respect to all the cost parameters involved in the model. The initial parameters of the cost model are set as follows:

c =2, θ = 5, $\delta_1 = \delta_2$=1, E= 0.01, a = 3, b = 0.01, T_0=1, T_1=2, T_2=1, C_2=5, W = 90,
C_0=10, C_1=20, ξ=0.05, η=2, γ=2, δ=1, μ=2.5, σ=1, k=3, Δ=0.5

Using the Equations (22) and (25) and the initial values of the parameters as given above, the optimal interval between the successive samples (h^*) and the optimal sample size (n^*) are obtained. Substituting these values in the total cost, 'Z', the optimal total cost Z^* is computed and all these values are presented inTable-1and Table-2.

Table 1. Optimal values of n, h and Z for various values of c, θ, ξ, η, γ and δ

C	θ	ξ	η	γ	δ	h*	n*	Z*
1.890	5	0.05	2	2	1	12.048	146	19.819
1.895	5	0.05	2	2	1	12.020	139	19.823
1.990	5	0.05	2	2	1	11.683	15	19.887
1.995	5	0.05	2	2	1	11.677	9	19.890
2	5.05	0.05	2	2	1	11.709	27	19.881
2	5.10	0.05	2	2	1	11.766	51	19.869
2	5.15	0.05	2	2	1	11.838	75	19.857
2	5.20	0.05	2	2	1	11.922	99	19.845
2	5	0.01	2	2	1	11.949	6	19.893
2	5	0.02	2	2	1	11.882	5	19.893
2	5	0.03	2	2	1	11.814	4	19.893
2	5	0.04	2	2	1	11.744	3	19.893
2	5	0.05	1.80	2	1	13.357	90	19.922
2	5	0.05	1.85	2	1	12.878	67	19.916
2	5	0.05	1.90	2	1	12.437	45	19.910
2	5	0.05	1.95	2	1	12.035	23	19.902
2	5	0.05	2	1.92	1	13.343	114	19.933
2	5	0.05	2	1.94	1	12.801	84	19.926
2	5	0.05	2	1.96	1	12.343	55	19.916
2	5	0.05	2	1.98	1	11.968	27	19.905
2	5	0.05	2	2	0.96	15.266	68	19.856
2	5	0.05	2	2	0.97	14.504	55	19.863
2	5	0.05	2	2	0.98	13.658	40	19.871
2	5	0.05	2	2	0.99	12.405	22	19.881

Table 2. Optimal values of n, h and Z for various values of C_0, C_1, C_2, W, a, b and Δ

C_0	C_1	C_2	W	a	b	Δ	h*	n*	Z*
9.80	20	5	90	3	0.01	0.5	11.562	51	19.866
9.85	20	5	90	3	0.01	0.5	11.582	39	19.873
9.90	20	5	90	3	0.01	0.5	11.606	27	19.880
9.95	20	5	90	3	0.01	0.5	11.636	15	19.887
10	20.05	5	90	3	0.01	0.5	11.636	15	19.937
10	20.10	5	90	3	0.01	0.5	11.606	27	19.980
10	20.15	5	90	3	0.01	0.5	11.582	39	20.023
10	20.20	5	90	3	0.01	0.5	11.562	51	20.066
10	20	10	90	3	0.01	0.5	13.446	28	19.919
10	20	15	90	3	0.01	0.5	14.933	44	19.934
10	20	20	90	3	0.01	0.5	16.243	56	19.944
10	20	25	90	3	0.01	0.5	17.426	66	19.951
10	20	5	87	3	0.01	0.5	11.535	74	19.853
10	20	5	88	3	0.01	0.5	11.562	51	19.866
10	20	5	89	3	0.01	0.5	11.606	27	19.880
10	20	5	90	3	0.01	0.5	11.672	3	19.894
10	20	5	90	2	0.01	0.5	12.079	95	19.895
10	20	5	90	2.25	0.01	0.5	11.977	72	19.895
10	20	5	90	2.5	0.01	0.5	11.875	49	19.894
10	20	5	90	2.75	0.01	0.5	11.773	26	19.894
10	20	5	90	3	0.001	0.5	11.702	13	19.893
10	20	5	90	3	0.003	0.5	11.675	6	19.893
10	20	5	90	3	0.005	0.5	11.669	4	19.893
10	20	5	90	3	0.007	0.5	11.668	3	19.893
10	20	5	90	3	0.01	0.75	12.192	33	19.892
10	20	5	90	3	0.01	1	12.616	60	19.893
10	20	5	90	3	0.01	1.25	13.042	85	19.895
10	20	5	90	3	0.01	1.5	13.495	109	19.897

From Table 1 , it is observed that as the shape parameter, ‘c’ increases , the optimal values of ‘n’ is decreasing, the optimal values of ‘h’ is decreasing and the expected cost per hour decreases for fixed values of the other parameters. If the parameter, ‘ϴ’ increases, the optimal values of ‘n’ are increasing, the optimal values of ‘h’ is increasing and the expected cost per hour decreases for fixed values of the other parameters. Regarding the Johnson distribution parameters, it is observed that as the parameter ‘ξ’ increases, the optimal values of ‘n’ is decreasing, the optimal values of ‘h’ is decreasing and the expected cost per hour remains constant for fixed values of the other parameters. When the parameter ‘η’ increases , the optimal values of ‘n’ is decreasing, the optimal values of ‘h’ is decreasing and the expected cost per hour decreases for fixed values of the other parameters. With respect to the parameter ‘γ’ , if it increases , the optimal values of ‘n’ is decreasing, the optimal values of ‘h’ is decreasing and the expected cost per hour decreases for fixed values of the other parameters. As the parameter ‘δ’ increases , the optimal values of ‘n’ is decreasing, the optimal values of ‘h’ is decreasing and the expected cost per hour increases for fixed values of the other parameters.

1The variation in optimal design parameters for various values of ‘c’ and ‘ϴ’ are shown in Figures 3 and 4 respectively.

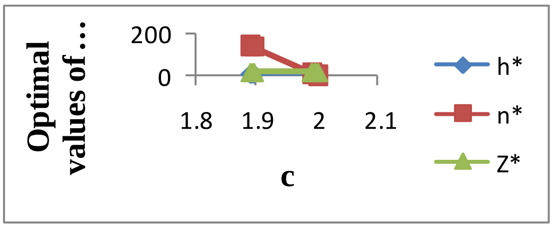

Figure 3. ‘c’ Vs Optimal values of h, n and Z

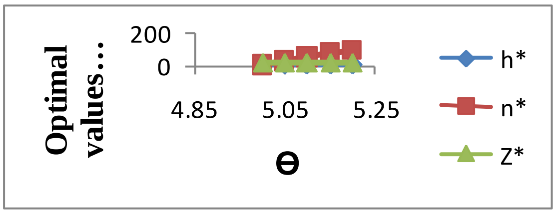

Figure 4. ‘ϴ’ Vs Optimal values of h, n, Z

From Table 2, it is observed that as the parameter ‘C_0’ increases, the optimal values of ‘n’ is decreasing, the optimal values of ‘h’ is increasing and the expected cost per hour increases for fixed values of the other parameters. When the parameter ‘C_1’ increases, the optimal values of ‘n’ is increasing, the optimal values of ‘h’ is decreasing and the expected cost per hour increases for fixed values of the other parameters .With regard to the parameter ‘C_2’, if it increases, the optimal values of ‘n’ is increasing, the optimal values of ‘h’ is increasing and the expected cost per hour increases for fixed values of the other parameters. As the parameter ‘W’ increases , the optimal values of ‘n’ is decreasing, the optimal values of ‘h’ is increasing and the expected cost per hour increases for fixed values of the other parameters. With reference to the parameter ‘a’, as it increases, the optimal values of ‘n’ is decreasing, the optimal values of ‘h’ are decreasing and the expected cost per hour decreases for fixed values of the other parameters. As the parameter ‘b’ increases, the optimal values of ‘n’ is decreasing, the optimal values of ‘h’ is decreasing and the expected cost per hour remains constant for fixed values of the other parameters. When the parameter ‘Δ’ increases , the optimal values of ‘n’ is increasing, the optimal values of ‘h’ is increasing and the expected cost per hour increases for fixed values of the other parameters

4. Optimal Design Parameters When the Process Out of Control Times are Random:

the earlier sections 3 and 4, we assumed that the time to identify the assignable causes for process out of control (T_1) and the time to repair or eliminate the assignable cause (T_2) are fixed and known. But in many production processes there are multiple assignable causes like defective raw materials, faulty setup, untrained operators, the cumulative effect of heat, vibration, shocks, power fluctuations, etc., when the process is governed by multiple assignable causes, ‘T_1’ and ‘T_2’ are also random and follows a probability distribution. A suitable distribution for ‘T_1’ and ‘T_2’ is a Weibull distribution since it accommodates constant, increasing and decreasing hazard rates. Hence, here we assume that ‘T_1’ and ‘T_2’ follow Weibull distributions with parameters (λ_1, ν_1) and (λ_2, ν_2) respectively, ‘λ’ being the scale parameter and ‘ν’ being the shape parameter.

$$f(t_1) = \lambda_1.\nu_1.t^{\nu_1-1}.e^{-\lambda_{1}.t_1{}^{\nu_1}}, \qquad \lambda_1 > 0, \nu_1 > 0, t_1 > 0 \text{ and} \tag{26}$$

$$f(t_2) = \lambda_2.\nu_2.t^{\nu_2-1}.e^{-\lambda_{2}.t_2{}^{\nu_2}}, \qquad \lambda_2 > 0, \nu_2 > 0, t_2 > 0 \tag{27}$$

The Expected values of ‘T_1’ and ‘T_2’ are

$$E(T_1) = \frac{1}{\lambda_1}.\Gamma\left(1+\frac{1}{\nu_1}\right) \text{ and} \tag{28}$$

$$E(T_2) = \frac{1}{\lambda_2}.\Gamma\left(1+\frac{1}{\nu_2}\right) \tag{29}$$

Substituting these values in the equation (18), we get the expected cost per a unit time as

$$Z = \{C_0\left(\frac{c.\theta}{c-1}\right) + C_1\{\left(S+\frac{1}{(1-\beta)}\right).h - \left(\frac{c.\theta}{c-1}\right) + n.E + \frac{\delta_1}{\lambda_1}.\Gamma(1+\frac{1}{\nu_1}) + \frac{\delta_2}{\lambda_2}.\Gamma(1+\frac{1}{\nu_2})\} + C_2.S.\alpha + \frac{(a+b.n)}{h}.\{\left(S+\frac{1}{(1-\beta)}\right).h + n.E + \frac{\delta_1}{\lambda_1}.\Gamma\left(1+\frac{1}{\nu_1}\right) + \frac{\delta_2}{\lambda_2}.\Gamma\left(1+\frac{1}{\nu_2}\right)\} + W\} / \{(1-\delta_1).T_0.S.\alpha + (S+\frac{1}{(1-\beta)}).h + n.E + \frac{\Gamma\left(1+\frac{1}{\nu_1}\right)}{\lambda_1} + \frac{\Gamma\left(1+\frac{1}{\nu_2}\right)}{\lambda_2}\} \tag{30}$$

Where, ‘α’ and ‘β’ are as defined in Equations (5) and (6) respectively.

for obtaining the optimal design parameters of the $\overline{X}$ chart, we differentiate ‘Z’ with respect to ‘h’ and ‘n’ and equate them to zero.

$\frac{\partial z}{\partial h} = 0$ implies,

$$\{\{(1-\delta_1).T_0.S.\alpha + \left(S+\frac{1}{(1-\beta)}\right).h + n.E + \frac{\Gamma\left(1+\frac{1}{\nu_1}\right)}{\lambda_1} + \frac{\Gamma\left(1+\frac{1}{\nu_2}\right)}{\lambda_2}\}.\{C_1.\left[S+\frac{1}{(1-\beta)} + h.R\right] + C_2.\alpha.R + \frac{(a+b.n)}{h}.\{S+\frac{1}{(1-\beta)} + h.R\} - \frac{(a+b.n)}{h^2}.\{\left(S+\frac{1}{(1-\beta)}\right).h + n.E + \frac{\delta_1}{\lambda_1}.\Gamma\left(1+\frac{1}{\nu_1}\right) + \frac{\delta_2}{\lambda_2}.\Gamma\left(1+\frac{1}{\nu_2}\right)\}\} - \{C_0\left(\frac{c.\theta}{c-1}\right) + C_1\{\left(S+\frac{1}{(1-\beta)}\right).h - \left(\frac{c.\theta}{c-1}\right) + n.E + \frac{\delta_1}{\lambda_1}.\Gamma(1+\frac{1}{\nu_1}) + \frac{\delta_2}{\lambda_2}.\Gamma(1+\frac{1}{\nu_2})\} + C_2.S.\alpha + \frac{(a+b.n)}{h}.\{\left(S+\frac{1}{(1-\beta)}\right).h + n.E + \frac{\delta_1}{\lambda_1}.\Gamma\left(1+\frac{1}{\nu_1}\right) + \frac{\delta_2}{\lambda_2}.\Gamma\left(1+\frac{1}{\nu_2}\right)\} + W\}.\{S+\frac{1}{(1-\beta)} + h.R + (1-\delta_1).T_0.S.\alpha.R\}\} / \{(1-\delta_1).T_0.S.\alpha + \left(S+\frac{1}{(1-\beta)}\right).h + n.E + \frac{\Gamma\left(1+\frac{1}{\nu_1}\right)}{\lambda_1} + \frac{\Gamma\left(1+\frac{1}{\nu_2}\right)}{\lambda_2}\}^2 = 0 \tag{31}$$

Where, ‘α’ and ‘β’ are as defined in Equations (5) and (6) respectively.

$\frac{\partial z}{\partial n} = 0$ implies,

$$\{\{(1-\delta_1).T_0.S.\alpha + \left(S+\frac{1}{(1-\beta)}\right).h + n.E + \frac{\Gamma\left(1+\frac{1}{\nu_1}\right)}{\lambda_1} + \frac{\Gamma\left(1+\frac{1}{\nu_2}\right)}{\lambda_2}\}.\{C_1.E + \frac{(a+b.n)}{h}.E + \left(\frac{b}{h}\right).\left[\left(S+\frac{1}{(1-\beta)}\right).h + n.E + \frac{\delta_1}{\lambda_1}.\Gamma\left(1+\frac{1}{\nu_1}\right) + \frac{\delta_2}{\lambda_2}.\Gamma\left(1+\frac{1}{\nu_2}\right)\right]\} - \{C_0\left(\frac{c.\theta}{c-1}\right) + C_1\{\left(S+\frac{1}{(1-\beta)}\right).h - \left(\frac{c.\theta}{c-1}\right) + n.E + \frac{\delta_1}{\lambda_1}.\Gamma(1+\frac{1}{\nu_1}) + \frac{\delta_2}{\lambda_2}.\Gamma(1+\frac{1}{\nu_2})\} + C_2.S.\alpha + \frac{(a+b.n)}{h}.\{\left(S+\frac{1}{(1-\beta)}\right).h + n.E + \frac{\delta_1}{\lambda_1}.\Gamma(1+\frac{1}{\nu_1}) + \frac{\delta_2}{\lambda_2}.\Gamma(1+\frac{1}{\nu_2})\} + W\}.E\} / \{(1-\delta_1).T_0.S.\alpha + \left(S+\frac{1}{(1-\beta)}\right).h + n.E + \frac{\Gamma\left(1+\frac{1}{\nu_1}\right)}{\lambda_1} + \frac{\Gamma\left(1+\frac{1}{\nu_2}\right)}{\lambda_2}\}^2 = 0 \tag{32}$$

Where, ‘α’ and ‘β’ are as defined in Equations (5) and (6) respectively.

Solving the equations (31) and (32) simultaneously for ‘h’ and ‘n’ using numerical techniques, we obtain the optimal time interval between successive samples (h^*) and the optimal sample size (n^*).

To study the effect of the random nature of ‘T_1’ and ‘T_2’ on the optimal design parameters we carry out the sensitivity analysis for the parameters ‘λ_1’, ‘ν_1’, ‘λ_2’ and ‘ν_2’ with the initial values of the other parameters as

c =2, θ = 5, δ_1= δ_2=1, E= 0.01, a = 3, b = 0.01, T_0=1, C_2=5,W = 90,C_0=10, C_1=20, ξ=0.05, η=2, γ=2, δ=1, μ=2.5, σ=1, k=3, Δ=0.5 and are shown in Table-3.

Table 3. Optimal values of n, h and Z for various values of λ_1, ν_1, λ_2 and ν_2

λ_1	ν_1	λ_2	ν_2	h*	n*	Z*
2	0.7	1	0.5	11.525	6	19.893
4	0.7	1	0.5	11.398	8	19.892
6	0.7	1	0.5	11.357	9	19.892
8	0.7	1	0.5	11.336	10	19.892
3	0.4	1	0.5	11.716	2	19.894
3	0.5	1	0.5	11.538	5	19.893
3	0.6	1	0.5	11.472	7	19.893
3	0.9	1	0.5	11.412	8	19.892
3	0.7	1.1	0.5	11.368	9	19.892
3	0.7	1.2	0.5	11.308	11	19.892
3	0.7	1.3	0.5	11.257	12	19.892
3	0.7	1.4	0.5	11.214	13	19.892
3	0.7	1	0.50	11.44	8	19.893
3	0.7	1	0.54	11.342	10	19.892
3	0.7	1	0.58	11.272	11	19.892
3	0.7	1	0.62	11.220	13	19.892

From Table 3, we observe that as the parameter 'λ_1' increases, the optimal values of 'n' is increasing, the optimal values of 'h' is decreasing and the expected cost per hour decreases for fixed values of the other parameters. When the parameter 'ν_1' increases , the optimal values of 'n' is increasing, the optimal values of 'h' is decreasing and the expected cost per hour decreases for fixed values of the other parameters. With respect to the parameter 'λ_2' as it increases , the optimal values of 'n' is increasing, the optimal values of 'h' is decreasing and the expected cost per hour remains constant for fixed values of the other parameters. As the parameter 'ν_2' increases , the optimal values of 'n' is increasing, the optimal values of 'h' is decreasing and the expected cost per hour decreases for fixed values of the other parameters. The optimal design parameters, n^* and h^* and the expected cost per a unit time are highly sensitive to the Weibull model parameters and by suitably estimating the model parameters we can have more accuracy in reducing the nonconformities and minimize the cost of Quality improvement program.

5. Conclusions:

In this paper we have proposed a Statistical economic design of $\bar{X}$ control chart for the variables having Johnson distribution as $\bar{X}$ distribution and the process in-control times follow a Pareto distribution. The Pareto distribution considered in this study can be applied for the processes which will run for a minimum period of time without non conformities. This distribution also includes the increasing and decreasing rates of failure. Minimizing the expected cost per a unit time, the optimal design parameters namely, sample size and time interval between successive samples are determined.

The numerical values indicate that the effect of Johnson distribution parameters and Pareto distribution parameters have significant effect on optimal design parameters. Another variation in this model is also considered by introducing randomness for 'T_1' and 'T_2' (Time to identify the assignable cause and time to repair). As a result of this modification it is observed that the model parameters of 'T_1' and 'T_2'will also significantly influence the design parameters. Sensitivity analysis carried out indicates that the optimal design parameters and the cost per a unit time are more sensitive towards the cost parameters than the other parameters. This design is much useful in quality control programs of production industries like chemicals, paints, films, etc.

Acknowledgements:

The authors are very much thankful to the reviewers and the chief editor for their constructive and helpful comments and suggestions which have improved the quality of the paper to the present level

References:

[1] H.A. Al–Oraini, M.A. Rahim, "Economic Statistical design of $\bar{X}$ control charts for systems with Gamma (λ,2) in-control times". Computers & Industrial Engineering, Vol. 43, 2002, 645-654.

[2] Y. Nagendra, G. Rai, "Optimum sample size and sampling interval for controlling non- normal variables". Journal of the American Statistical Association, Vol. 66, 1971, 637-646.

[3] M.A. Rahim, "Economic model of $\bar{X}$ chart under non-normality and measurement errors". Computer and Operations Research, Vol. 12, 1985, 291-299.

[4] J.W. Burr, "The effects of non-normality on constants for $\bar{X}$ and R charts". Industrial Quality control, Vol. 23, 1967, 563-568.

[5] S.A. Yourstone, W.J. Zimmer, "Non-normality and the design of control charts for averages". Decision Sciences, Vol. 23, 1992, 1099-1113.

[6] C. Chou, C. Chen, H. Liu, "Economic statistical design of $\bar{X}$ charts for non-normal data by considering quality loss". Journal of Applied Statistics, Vol. 27, 2000, 939-951.

[7] Huifen Chen and Yuyen Cheng, "Non-normality effects on the economic statistical design of $\bar{X}$ charts with Weibull in-control time". European Journal of Operational Research, Vol. 176, 2007, 986-998.

[8] T.P. Mc Williams, "Economic control chart designs and the in-control time distribution: A sensitivity study". Journal of Quality Technology, Vol. 21, 1989, 103-110.

[9] T.J. Lorenzen, L.C. Vance, "The economic design of control charts: A unified approach". Technometrics, Vol. 28, 1986, 3-10.

[10] Johnson, N.L., Kotz, S., Balakrishnan, N. Continuous Univariate distributions.

Vol. 1 and 2. Newyork: John Wiley & Sons. Inc; 1994.

JJMIE
Jordan Journal of Mechanical and Industrial Engineering

Volume 4, Number 3, June, 2010
ISSN 1995-6665
Pages 372 - 377

Strengthening Aluminum Scrap by Alloying with Iron

W. Khraisat[a], and W. Abu Jadayil

Department of Industrial Engineering, The Hashemite University, Zarqa, 13115, Jordan

Abstract

The aim of this research is to experimentally study the effect of strengthening aluminum scrap by iron powder in order to achieve better mechanical properties. Aluminum scrap is melted in a heated furnace to form a melt composition. The melt is adjusted to form the present composition, consisting essentially of iron, 1,2,3 and 5 wt%. The alloys were made by melting scrap aluminum using an induction furnace, and then iron powder was added to the melt. The composition is then casted into steel moulds to be later machined to produce tensile tests specimens. The mechanical and metallurgical characteristics of the fabricated alloys were studied through optical, Hardness survey, and tensile testing. Superior properties were obviously manifested in the cast aluminum with 1 wt% iron addition. Ultimate tensile strength and elongation to fracture and Vickers hardness were all increased by 72 %, 60%, and 7% respectively.

Keywords: Aluminum Scrap; Iron Powder; Casting; Mechanical Properties.

1. Introduction and Literature Review

Pure aluminum is weak having a tensile strength between 90 to 140 N/mm^2, however, wrought aluminum in its alloyed form has higher strength and is similar to structural steels. It is mainly used for electrical conductors and for domestic products, however, for structural use it has to be strengthened by alloying [1].

Aluminum alloys are used extensively in making mechanical parts due to its high specific strength (strength/density). The main usage of aluminum alloys are in applications requiring light weight materials as in aerospace industries and in automotive industries. The second important property of aluminum is its resistance to corrosion. Aluminum has a strong protective oxide layer which prevents continues corrosion of the base material. Therefore, a lot of work is done to achieve better properties of aluminum by alloying, heat treatment and other processes. On the other hand aluminum has a big disadvantage of having a low melting temperature which put limits on the temperature range of applications

Aluminum can be recycled, it retains a high scrap value. It can be recycled indefinitely without losing any of its superior characteristics, making it especially appealing according to both environmental and economic criteria

Aluminum recycling saves 95 percent of the energy required to produce aluminum from raw materials. Conserving natural resources is important; because it takes four pounds of bauxite ore to produce one pound of aluminum, every pound of recycled aluminum saves four pounds of ore. Increasing the use of recycled metal has an important effect on the CO2 emission, since producing aluminum by recycling produces only about 4% as much CO_2 as by producing it from natural resources [2,3].

Iron is the most common impurity found in aluminum. It has a high solubility in molten aluminum and is therefore easily dissolved in the liquid state of aluminum, however its solubility in the solid state is very low (~0.04%). The low solubility of iron in the solid state is accompanied by decreased ductility as a result of the formation of intermetallic phases like FeAl and/or Fe_3Al. These intermetallic phases increases the strength of the aluminum alloy they also enhances corrosion resistance. [4,5].

The most difficult elements to control in the recycled aluminum is Fe and Si and these elements tend to increase slightly the more often the metal has been recycled. Fe in particular has a higher tendency to increase gradually in metal recycled over and over again, primarily from pickup from scrap handling systems. As a result, Fe is an ideal candidate for application to alternative products, a good example of which is the use of increased Fe content in aluminum as a deoxidizing agent for steel production. This would benefit both the aluminum and steel industries and add to the life-cycle benefits of aluminum operations [6]. Another example of using high Fe bearing aluminum is to make use of the affinity of Zr for Fe, creating a heavy particle readily taken from an aluminum melt [6].

The mechanical behaviour of an alloy based on Fe-40A1 prepared from mechanically alloyed powders was examined over a wide temperature range in the fine-grained, as-extruded state as well as after recrystallizing to a large-grained state by Morris and Gunther in 1995 . They found that the fine-grained material was strong and reasonably ductile at room temperature, in contrast with the weaker and more brittle large-grained material. At high temperature the strength fell to low values, similar for both materials. They related that behaviour to the contribution of strengthening due to the particles present [7]. Sasaki *et. al., in 2009,* consolidated Nanocrystalline Al–5 at.% Fe alloy powders produced by mechanical alloying by spark plasma sintering. The sintered sample showed high strength with a large plastic strain of 15% at room temperature and 500 MPa at 350 ºC. A range of mechanical properties have been investigated for non-hardenable aluminium alloys [8]. Zander et. al., in 2007, took into account in their study *the* particle strengthening and work hardening the models solid solution. Morris *et. al.,* in 2006, descovered a new iron–aluminium alloy with zirconium and chromium additions that forms fine coherent precipitates on annealing cast material that remain very fine even after extended annealing at temperatures as high as 900 ºC. Using this new model they could improve high-temperature creep stresses.

In this study aluminum and iron powder were processed by casting into rectangular shaped samples. Iron powder was added to molten aluminum to obtain a two phase material consisting of aluminum matrix and a second dispersed iron aluminide phase. The solubility of iron in aluminum is almost negligible at room temperatures this in turn results in a composite material of more than one phase. The strength of the resulting material will depend mainly on the amount of the iron aluminides present in the microstructure. The properties will also depend on the amount of other alloying elements found the material.

In order to optimize the material properties for certain applications it is necessary to study the cast structures. In the present work this has been done for iron aluminides. The results are discussed with respect to material parameters like composition.

Generally recycling needs a significant challenge in shredding, sorting, and, in some cases, further refining of the metal to achieve acceptable impurity levels. Fe in particular can be a significant challenge.

Aluminum scrap is refined by separation processes that increase metal purity such as the segregation method, the solid solution separation method, the temperature gradient method, the eutectic separation method, the inter-metallic compound method, the gravity separation method, etc. These methods, however, are difficult to apply to the manufacturing systems because of low efficiency, complicated apparatus, high cost and environmental contamination [11]. This puts high demands for innovative separation technologies to improve the sorting, and thereby the quality, of scrap. Another approach is to reduce significantly the amounts of various elements that occur in scrap, the nearly universal alternative for controlling such elements in recycled aluminum alloys is to dilute them with purer alloy grades or virgin pig [12].

2. Materials, Experiments, and Characterization

2.1. Materials

Scrap aluminum consisting mainly of electrical cables having the composition shown in table 1, was first melted and then iron powder was added to the melt. The amount of powder added and the total composition of the mixture is shown in table 2. The iron powder has the commercial designation ASC 100 delivered by Höganäs AB, Sweden. The powder is a water atomized iron powder having a packing density of ≈ 3 g/cm^3 and a particle size range between 20 to 150 µm.

Table 1. Chemical composition (wt-%) of the aluminum alloy used in electrical cables

Al	Si	Fe	Cu	Ti	V	Mn
99.84	0.0517-0.0361	0.1256-0.0728	0.0017-0.0007	0.01-0.0075	0.01-0.0075	0.003-0.0006

Table 2. Composition (wt-%) of the five alloys investigated

Alloy	wt% Scrap Aluminum	wt% ASC 100
1	100	0
2	99	1
3	95	5
4	90	10
5	85	15

2.2. Experimental Procedure

The successive stages of casting the aluminum scrap are:

Firstly the aluminum cables were cut into small pieces and then they were cleaned from surface oxides by a sand plaster machine. This was done to reduce the amount of slag present in the molten metal and to avoid or minimize the oxide present in the casting**.**

Secondly, the small pieces of the aluminum scrap wires were melted in a batch furnace having a maximum temperature of 1300 ºC with no protective atmosphere. This was done by heating the furnace to 1000 ºC then the aluminum scrap wires were added into the crucible.

Thirdly, when the aluminum scrap wires were completely melted the iron powder was added to the melt. The mixture was stirred continuously in order to avoid sedimentation and to achieve a more homogeneous mixture.

Finally, the mixture was then poured into a rectangular shaped mould and cold in air.

2.3. Characterization

The mechanical properties of the cast aluminum scrap were tested using an Instron universal testing machine. The tensile testing samples were made by machining the as cast alloys using a chipping machine and a milling machine.

The microstructure of the as- cast alloys was characterized by means of an optical microscope. Sample preparation was done by wet grinding, diamond polishing and etching in a chemical solution (0.5% -1%HF. 2.5% HNO_3, 1.5%HCl, and 95.5% distilled water).

3. . Results

3.1. Mechanical properties

The results of the mechanical properties are shown in Figs, 1, 2, and 3. These figures give a summary of the obtained mechanical properties, ultimate tensile strength (UTS), elongation to fracture, and Vicker's hardness.

Figure1 shows the effect of percent iron added to aluminum on UTS. The standard deviations of the mean for the measured UTS are indicated by the scatter bands at top of the bars in the figure. Clearly, the scatter is rather high for alloy 1 and for the other alloys the scatter is rather low and a comparison between different alloys can be made. As can be seen from Figure1, the UTS increases compared to the starting alloy with increasing iron addition from 1 wt% to 5 wt% then the UTS value drops down below the UTS of the starting alloy with further iron addition. The highest obtained UTS is for alloy 2 which is about 155 MPa and the lowest UTS is for alloy 5 which is about 40 MPa.

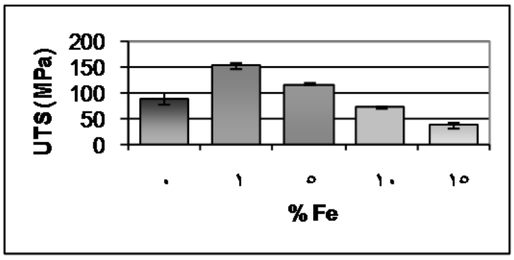

Figure 1. UTS values for the alloys studied in their as cast condition.

Figure2 shows the elongation to fracture for the different alloys. As in the previous figure, the error bars indicating the standard deviations shows that the scatter for the starting alloy is rather high thus a rough comparison can be made. The maximum elongation obtained is for alloy 2 which is about 16 % elongation to fracture and the minimum elongation is for alloy 5 which is about 0.2% elongation to fracture.

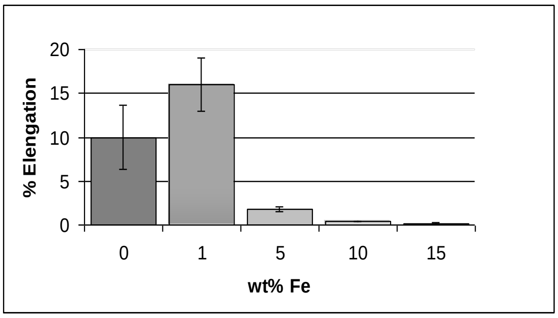

Figure 2. Elongation to fracture for the alloys studied in their as cast condition

The effect of Fe addition on the hardness of the starting alloy is shown in Figure3. The error bars indicating the standard deviations show that the scatter in measured data is such that a comparison of the measured hardness can be made for the different alloys. The measured hardness values indicate a continuous increase in hardness with increasing added iron to the starting alloy. The maximum hardness values is obtained for alloy 5 which is about 43 HV and the minimum hardness value is for alloy 1 which is about 21 HV

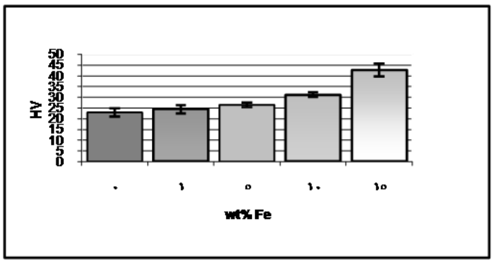

Figure 3. Vickers hardness for the alloys studied in their as cast condition.

3.2. Microstructure

Microstructural analyses were conducted by optical microscopy. The microstructures of as cast samples are given in Figures. 4, 5 and 6.

Fig.4 shows the microstructure of the starting alloy number 1. It's clear from the micrograph that the microstructure consists of grains of Aluminum. The black dots in the microstructure are mainly effects of etching and some impurities.

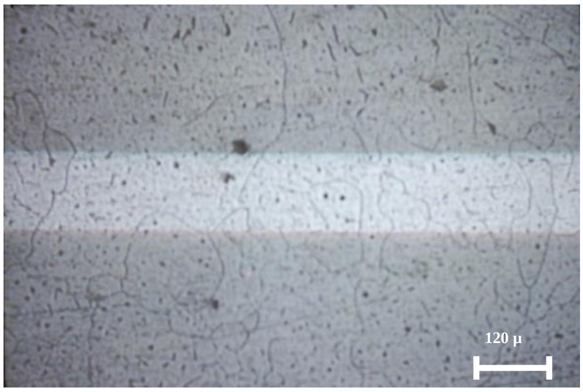

Figure 4. As cast microstructure of alloy 1 showing grain and grain boundaries of Aluminum

Fig. 5 shows the microstructure of alloy 2. The as cast microstructure of alloy 2 shown in Fig. 5 consists of two phases, the dark phase which is iron aluminide located at grain boundaries and a light phase which is aluminum grains

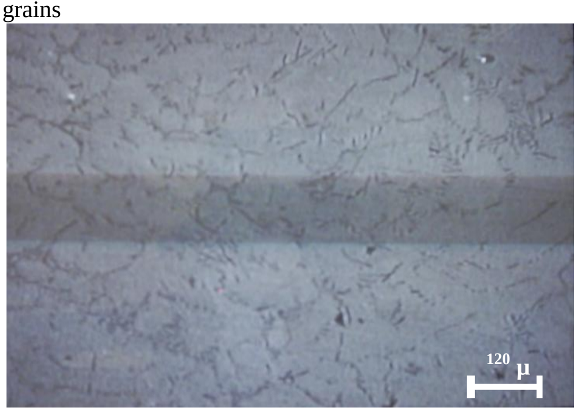

Figure 5. As cast microstructure of alloy 2 showing two phases the dark phase which is iron aluminide and the light phase aluminum grains

Fig. 6 shows the microstructure of alloy 3. The microstructure consists of two phases the dark phase which is iron aluminide and the light phase aluminum grains.

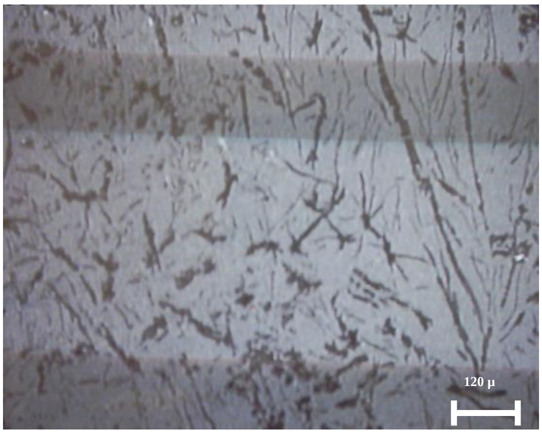

Figure 6. Microstructure of alloy 3 after sintering showing two phases the dark phase which is iron aluminides and the light phase aluminum grains.

4. Discussion

The analysis of the results shows that the effect of the 1% addition of iron to aluminum scraps has a positive effect on the mechanical properties of the aluminum scraps (UTS and elongation to fracture). This can be attributed to the precipitation of intermetallic compound on the grain boundaries of aluminum.

Increasing the amount of iron to above 1% deteriorates the mechanical properties except for hardness. This is due to the increase of the hard inter-metallic phase amount in the microstructure.

The mechanical properties of the alloys containing iron aluminides are very sensitive to the amount of iron aluminide and to factors affecting the strength of the iron aluminide like aluminum content dissolved in the iron aluminide, order (type, amount, and size), heat treatment, test temperature, and defects because Iron aluminides have limited ductility at ambient temperatures.

Considering the equilibrium binary phase diagram for aluminum and iron, as the iron content increases, the amount of the intermetallic phase Al3Fe increases too. For alloy 2 the amount of Al3Fe present is approximately 4% by atomic weight and for alloy 3 the amount of Al3Fe is approximately 20 % by atomic weight. The mechanical properties of iron aluminides are very sensitive to many factors including aluminum content, order (type, amount, and size), heat treatment, test temperature, alloying additions, environment, microstructure, and defects [13].

Studies have shown that the ductility of the Fe3Al-based aluminide can be substantially improved by increasing aluminum content from 25 to 28% [14]. Thus by increasing the amount of iron in the alloys studied the amount of aluminum in the intermetallic phase decreases leading to a decrease in ductility.

The mechanical properties of the starting alloy with no iron addition showed inferior properties. This can be attributed to the fact that the microstructure is made up of coarse grains as shown in Fig.4. Adding iron to Aluminum causes grain refinement which is evident from alloy 2 where superior mechanical properties is obtained compared to the starting alloy. According to ref. [15] adding 0.5 wt% Fe content to pure aluminum caused the most effective grain refinement compared to the other iron contents.

From the finding of this work it can be stated that instead of refining the aluminum scrap by expensive means or by controlling the composition of aluminum scrap by diluting elements found in the scrap with purer alloy grades or virgin pig, enhancing the mechanical properties by alloy addition like the addition of iron as in the case of recycled electrical wires is a more economical and less time consuming process.

5. Conclusions

- Superior properties were obviously manifested in the cast aluminum with 1 wt% iron addition. Ultimate tensile strength and elongation to fracture and Vickers hardness are increased by 72 %, 60%, and 7% respectively at ambient temperature.
- The low ductility of the used aluminum scrap is due to its coarse grain structure

References

[1] J. Dwight, "Aluminum Design and Construction". E & FN SPON, an imprint of Routledge London and New York, 1999.

[2] S. Das, "Designing Aluminum Alloys for a Recycle-Friendly World". Secat, Inc., Light Metal Age, 2006.

[3] S. Das, "Designing Aluminum Alloys for a Recycle-Friendly World". Materials Science Forum, Vol. 519-521, 2006, 1239-1244.

[4] J. Kaufman, E. Rooy, "Aluminum Alloys and Castings Properties, Process, and Applications". American foundry society, ASM International, Materials Park. 2004.

[5] R. Fielding, "Recycling Aluminum, Especially Processing Extrusion Scrap". Light Metal Age, Vol. 63, No. 4, 2005, 20-35.

[6] Technical notes, Advanced Materials & Processes, ASM International, Materials Park, OH, 2005, 67.

[7] D. Morris, S. Gunther, "Strength and Ductility of Fe-40A1 Alloy Prepared by Mechanical Alloying". Materials Science and Engineering, Vol. 208, 1996, 7-19.

[8] T. Sasaki, T. Ohkubo, and K. Hono, "Microstructure and Mechanical Properties of Bulk Nanocrystalline Al–Fe Alloy Processed by Mechanical Alloying and Spark Plasma Sintering". Acta Materilia, Vol. 57, 2009, 3529-3538.

[9] J. Zander, R. Sandstrom, and L. Vitos, "Modelling Mechanical Properties for Non-Hardenable Aluminium Alloys". Computational Materials Science, Vol. 41, 2007, 86-95.

[10] D. Morris, M. Morris, and L. Requejo, "New Iron–Aluminium Alloy with Thermally Stable Coherent Intermetallic Nanoprecipitates for Enhanced High-Temperature Creep Strength". Acta Materilia, Vol. 54, 2006, 2335-2341.

[11] J. Kim, E. Yoon, "Elimination of Fe Element in A380 Aluminum Alloy Scrap by Electromagnetic Force". Journal of Materials Science Letters, Vol. 19, No. 3, 2000, 253-255.

[12] J. Hess, “Physical Metallurgy of Recycling Wrought Aluminum Alloys”. Metallurgical and Materials Transactions A, Vol. 14, No. 2, 1983, 323-327.

[13] C. McKamey, V. Sikka, and G. Goodwin, “Development of Ductile Fe3Al Based Aluminides”. Oak Ridge National Laboratory, 1993.

[14] C. McKamey, J. Horton, and C. Liu, “High Temperature Ordered lntermetallics”. Edited by N. Stoloff, C. Koch, C. Liu, and O. Izumi, MRS, Pittsburgh, 1987.

[15] Y. Zhang, N. Ma, H. Yi, S. Li, and H. Wang, “Effect of Fe on Grain Refinement of Commercial Purity Aluminum”. Journal of Materials and Design, Vol. 27, No. 9, 2006, 794-798.

JJMIE

Volume 4, Number 3, June, 2010
ISSN 1995-6665
Pages 378 - 387

Jordan Journal of Mechanical and Industrial Engineering

Investigation into the Vibration Characteristics and Stability of a Welded Pipe Conveying Fluid

Nabeel K. Abid Al-Sahib [a], Adnan N. Jameel [b], Osamah F. Abdulateef [a,*]

[a] *Al-Khawarizmi College of Engineering, University of Baghdad, Jaderyia, Baghdad, Iraq*

[b] *College of Engineering, University of Baghdad, Jaderyia, Baghdad, Iraq*

Abstract

The stability of fluid conveying welded pipe is of practical importance because the welding induced residual stresses which affected on the vibration characteristics and stability. This paper deals with the vibration and stability of straight pipe made of ASTM-214-71 mild steel, conveying turbulent steady water with different velocities and boundary conditions, the pipe was welded on its mid-span by single pass fusion arc welding with an appropriate welding parameters. A new analytical model was derived to investigate the effects of residual stresses at girth welds of a pipe on the vibration characteristics and stability. The reaction components of the residual stresses at a single pass girth weld in a pipe was used in combination with a tensioned Euler-Bernoulli beam and plug flow model to investigate the effect of welding on the vibration characteristics of a pipe. The stability is studied employing a D-decomposition method. A finite element (FE) simulation was presented to evaluate velocity and pressure distributions in a single phase fluid flow. A coupled field fluid-structure analysis was then performed by transferring fluid forces, solid displacements, and velocities across the fluid-solid interface. A prestressed modal analysis was employed to determine the vibration characteristics of a welded pipe conveying fluid. Experimental work was carried out by built a rig which was mainly composed of a different boundary conditions welded pipes conveying fluid and provided with the necessary measurement equipments to fulfill the required investigations. It has been proven theoretically and experimentally that the residual stresses due to welding reducing natural frequencies for both clamped-clamped and clamped-pinned pipe conveying fluid. Also, we proved that for small fluid velocity (sub-critical), the clamped-clamped and clamped-pinned welded pipes conveying fluid are stable. For relatively high fluid velocities (super-critical) the clamped-pinned welded pipe loses stability by divergence.

Keywords**:** Stability; pipe conveying fluid; welding.

Nomenclature

- A_i Internal cross sectional area of the pipe (m2).
- C_j Amplitudes of vibrations.
- EI Bending stiffness of the pipe (Nm^2).
- $f_{int}(z, t)$ Force acting on the pipe from inside (N).
- g_j Wave numbers.
- K Dimensionless stiffness of the rotational stiffness.
- K_{rs} Stiffness of the rotational spring.
- L Length of the pipe (m).
- m Pipe and Fluid mass per unit length (Kg/m).
- m_f Fluid mass per unit length (Kg/m).
- m_p Pipe mass per unit length (Kg/m).
- P_i Hydrostatic pressure inside the pipe (N/m^2).
- T Axial force due to welding (N).
- $T_{eff.}$ Effective force (N).
- t Time (sec).
- U Fluid velocity (m/sec).
- V Non-dimensional fluid velocity.
- Ω Non-dimensional natural frequency.
- ω Circular frequency of motion (rad/sec).
- λ Eigenvalue of the characteristic equation.
- η Non-dimensional transverse displacement of the pipe y/L.
- ξ Non-dimensional z-coordinate along the pipe z/L.

1. Introduction

The fluid flow and pipes are interactive systems, and their interaction is dynamic. These systems are coupled by the force exerted on the pipe by the fluid. The fluid force causes the pipe to deform. As the pipe deforms it changes its orientation to the flow and the fluid force may change. Mathematical models are generated for the pipe and fluid, the dynamic interaction is described by nonlinear oscillator equations. The stability of fluid conveying welded pipes is of practical importance because the natural frequency of a pipe generally decreases with the increasing velocity of the fluid flow $\omega_1 = \omega_N\ [1-(U/U_c)^2]^{1/2}$, Where ω1 is the fundamental natural frequency of the pinned-pinned pipe conveying fluid, ω_N is the fundamental natural frequency of the pipe in the absence of fluid flow, U_c is the critical velocity of flow for static buckling, and U is the fluid velocity. In certain problems involving very high velocity flows through flexible thin-walled welded pipes, such as

* Corresponding author. ausamalanee@yahoo.com.

those used in the feed lines to rocket motors and water turbines, the decrease in natural frequency can be important. The pipe may become susceptible to resonance or fatigue failure if its natural frequency falls below certain limits. If the fluid velocity becomes large enough, the pipe can become unstable.

Many researchers have been carried out on the vibration of a pipe conveying fluid. Amabili, Pellicano, and Paidoussis [1] investigated the non-linear dynamic and stability of simply supported, circular cylindrical shells containing in-viscid incompressible fluid flow. Manabe, Tosaka, and Honma [2] discussed the dynamic stability of a flow conveying pipe with two lumped masses by using domain decomposition boundary element method. Amabili, Pellicano, and Paidoussis [3] investigated the response of a shell conveying fluid to harmonic excitation, in the spectral neighborhood of one of the lowest natural frequencies for different flow velocities. Yih-Hwang and Chih-Liang [4] studied the vibration control of Timoshenko pipes conveying fluid. Excessive vibration in this flow induced vibration problem was suppressed via an active feedback control scheme. Nawaf M. Bou-Rabee [5] examined the stability of a tubular cantilever conveying fluid in a multi-parameter space based on non-linear beam theory. Lee and Chung [6] presented a new non-linear model of a straight pipe conveying fluid for vibration analysis when the pipe is fixed at both ends. Using the Euler-Bernoulli beam theory and the non-linear Lagrange strain theory, from the extended Hamilton's principle the coupled non-linear equations of motion for the longitudinal and transverse displacements are derived. These equations of motion are discretized by using the Galerkin method. Reddy and Wang [7] derived equations of motion governing the deformation of fluid-conveying beams using the kinematic assumptions of the (a) Euler-Bernoulli and (b) Timoshinko beam theories. The formulation accounts for geometric nonlinearity in the Von Karman sense and contributions of fluid velocity to the kinetic energy as well as to the body forces. Finite element models of the resulting non-linear equations of motion were also presented. Kuiper and Metrikine [8] proofed analytically a stability of a clamped-pinned pipe conveying fluid at a low speed. A tensioned Euler-Bernoulli beam in combination with a plug flow model was used as a model. The stability was studied employing a D-decomposition method. Langre and Paidoussis [9] considered the stability of a thin flexible cylinder considered as a beam, when subjected to axial flow and fixed at the upstream end only. A linear stability analysis of transverse motion aims at determining the risk of flutter as a function of the governing control parameters such as the flow velocity or the length of the cylinder. Stability is analyzed applying a finite difference scheme in space to the equation of motion expressed in the frequency domain.

From these papers a considerable shortage of the investigation about the effect of residual stresses at welds in pipes on the vibration characteristics and stability of a pipe conveying fluid.

2. Vibration of A Welded Pipe Conveying Fluid

The welded pipe conveying fluid sketched in Figure. (1) is initially straight, stressed, and finite length. The following assumptions are considered in the analysis of the system under consideration [10]:

- Neglecting the effect of gravity, material damping, shear deformation and rotary inertia.
- The pipe considered to be horizontal.
- The pipe is inextensible.
- The lateral motion y (z, t) is small and of long wavelength as compared to the diameter of the pipe so that the Euler-Bernoulli theory is applicable for description of the pipe dynamic bending.
- Neglecting the velocity distribution through the cross-section of the pipe.

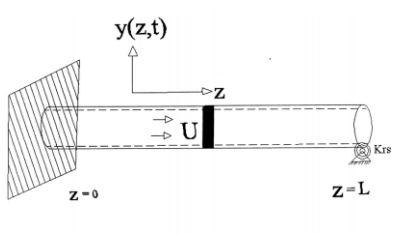

Figure 1. Welded pipe conveying fluid

Derivation of the equation of motion for pre-stressed single-span pipe conveying fluid as a function of the axial distance z and time t, based on beam theory is given by:

$$EI\frac{\partial^4 y}{\partial z^4} - T\frac{\partial^2 y}{\partial z^2} + m_p\frac{\partial^2 y}{\partial t^2} = f_{\text{int}}(z,t) \quad (1)$$

Where: EI is the bending stiffness of the pipe, mp is the mass of the pipe per unit length, T is a prescribe axial force due to welding, f_{int} (z, t) is a force acting on the pipe from inside.

The axial force due to welding T is obtained by multiplying the axial bending stress obtained from welding on the inner and outer surfaces at any section inside or outside the tensile zone σ_{zb} by the cross sectional area of the pipe. The axial bending stresses are a function of the curvature [11]:

$$\sigma_{zb} = \mp\frac{Et}{2(1 \quad \upsilon^2)}\frac{d^2 y}{dz^2} \quad (2)$$

The internal fluid flow is approximated as a plug flow, i.e., as if it was an infinitely flexible rod traveling through the pipe, all points of the fluid having a velocity U relative to the pipe. This is a reasonable approximation for a fully developed turbulent flow profile [12]. The inertia force exerted by the internal plug flow on the pipe, can be written as:

$$f_{\text{int}} = -m_f\frac{d^2 y}{dt^2}\Big|_{z=U.t} \quad (3)$$

Where m_f is the fluid mass per unit length, U is the flow velocity. The total acceleration of the fluid mass can be decomposed into a local, carioles and centrifugal acceleration:

$$m_f \frac{d^2y}{dt^2}\bigg|_{z=U.t} = m_f\left\{\left\{\frac{d}{dt}\left(\left(\frac{\partial y}{\partial t}+\frac{\partial y}{\partial z}\frac{dz}{dt}\right)\right)\Big|_{z=U.t}\right\}\right\}$$
$$= m_f\left\{\left\{\frac{d}{dt}\left(\left(\frac{\partial y}{\partial t}+U\frac{\partial y}{\partial z}\right)\right)\Big|_{z=U.t}\right\}\right\}$$
$$= m_f\left\{\left\{\frac{\partial^2 y}{\partial t^2}+2U\frac{\partial^2 y}{\partial z\,\partial t}+U^2\frac{\partial^2 y}{\partial z^2}\right\}\right\} \quad (4)$$

The internal fluid causes a hydrostatic pressure on the pipe wall. This can easily be incorporated by changing the true axial force due to welding into a so-called effective force.

$$T_{eff.} = T - A_i P_i \quad (5)$$

Where A_i is the internal cross sectional area of the pipe, and P_i is the hydrostatic pressure inside the pipe. Combining Eqs. (1) ~ (5) the resulting equation of motion for a pre-stressed pipe conveying fluid can be written as:

$$EI\frac{\partial^4 y}{\partial z^4}+\left(m_f U^2 - T_{eff.}\right)\frac{\partial^2 y}{\partial z^2}+2m_f U\frac{\partial^2 y}{\partial z\,\partial t}+m\frac{\partial^2 y}{\partial t^2}=0 \quad (6)$$

In which $m=m_f+m_p$. The left end of the pipe is rigidly support, whereas the right end is assumed to allow no lateral displacement but to provide a restoring moment proportional to the rotation angle of the pipe. The clamped-clamped or clamped-pinned pipe is obtained from this formulation in the limit of the restoring rotational moment going to infinity or zero respectively. Thus, the boundary conditions at ends of the pipe are given as:

$$y(0,t)=0 \quad (7)$$
$$\frac{\partial y(0,t)}{\partial z}=0 \quad (8)$$
$$EI\frac{\partial^2 y(L,t)}{\partial z^2}= \quad K_{rs}\frac{\partial y(L,t)}{\partial z} \quad (9)$$
$$y(L,t)=0 \quad (10)$$

Where K_{rs} is the stiffness of the rotational spring at the right end. Introducing the following dimensionless variables and parameters:

$$\eta = y/L,\ \xi = z/L,\ \tau = t\sqrt{EI/m}/L^2,$$
$$V = U\sqrt{m_f/EI},\ \ K = K_{rs}L/EI,$$
$$\alpha = L\sqrt{T_{eff.}m_f/(mEI)},\ \ \beta = L^2 T_{eff.}/EI.$$

The statement of the problem Eqs. (6) ~ (10) is rewritten as:

$$\frac{\partial^4\eta}{\partial\xi^4}+\beta\left(V^2-1\right)\frac{\partial^2\eta}{\partial\xi^2}+2\alpha V\frac{\partial^2\eta}{\partial\xi\partial\tau}+\frac{\partial^2\eta}{\partial\tau^2}=0 \quad (11)$$
$$\eta(0,\tau)=0 \quad (12)$$
$$\frac{\partial\eta(0,\tau)}{\partial\xi}=0 \quad (13)$$
$$\frac{\partial^2\eta(1,\tau)}{\partial^2\xi}=-K\frac{\partial\eta(1,\tau)}{\partial\xi} \quad (14)$$
$$\eta(1,\tau)=0 \quad (15)$$

To find the eigenvalues of the problem (11) ~ (15), which determine the stability of the pipe, the displacement η (ξ, τ) is to be sought in the following form:

$$\eta(\xi,\tau)=w(\xi)e^{\lambda\tau} \quad (16)$$

The pipe is unstable if one of the eigenvalues λ has a positive real part. Substituting Eq. (16) into the equation of motion Eq. (11), the following ordinary differential equation is obtained:

$$\frac{d^4w}{d\xi^4}+\beta\left(V^2-1\right)\frac{d^2w}{d\xi^2}+2\alpha V\lambda\frac{dw}{d\xi}+\lambda^2 w=0 \quad (17)$$

The general solution to this equation is given by:

$$w(\xi)=\sum_{j=1}^{4}C_j e^{ig_j\xi} \quad (18)$$

Where C_j are amplitudes of vibrations and g_j are the wave numbers. Substituting Eq. (18) into Eq. (17), a relationship is obtained between the wave numbers g_j and the eigenvalues λ:

$$g^4{}_j - \beta\left(V^2-1\right)g^2{}_j + 2\alpha V\lambda_i g_j + \lambda^2 = 0 \quad (19)$$

From these relationships four wave numbers g_j can be determined as functions of λ and the pipe parameters.

3. Natural Frequency

In order to evaluate the natural frequency for the system under consideration, substituting Eq. (17) into the boundary conditions Eqs. (12)~ (15). This yields the following system of four linear algebraic equations which can be written in matrix form as follows:

$$[H_{i,j}]\{C_j\}=0 \quad (20)$$

Where i,j=1,2,3,4. This system of equations has a non-trivial solution if, and only if its determinant Δ is equal to zero, which leads to the characteristic equation Δ =0. Trial and error procedure, the value of Ω (where λ=i Ω) that makes the determinant vanished can be found which will represent the non-dimension natural frequency. The non-dimensional frequency Ω related to the circular frequency of motion ω by the following equation:

$$\Omega=(m/EI)^{1/2}L^2\omega \quad (21)$$

4. Stability of A Welded Pipe Conveying Fluid

Linear structures containing flow inside them are found commonly in the wide range of applications. The macroscopic example is a pipeline for the oil industry. Intuitively, it seems that such a tube-like structure can be unstable and will rush about widely for the powerful flow inside it, but in the context of physics it is not obvious. The D-decomposition method, which is used in this paper, was developed for stability analyses of linear dynamical systems [13, 14].

The D-decomposition method has both advantages and disadvantages. The main advantage becomes apparent if a parametric study of stability should be performed. A D-decomposed plane of a parameter P contains information on stability of the system for all values of P, whereas the Argand diagram, for example, indicates the stability for a specific value of this parameter, only (if this parameter is not the fluid speed). Another advantage of the D-decomposition method is that it is equally applicable to pipes with any (linear) boundary conditions. For applying this method, no introduction of comparison functions is necessary (which takes quite an experience), like in the case of Galerkin method. The major disadvantage of the D-decomposition method is that having decomposed the plane of a parameter, it is still necessary to know the number of "unstable" eigenvalues for a specific, though arbitrary, value of this parameter. To find this number is not necessarily an easy task, although it can always be done by using the principle of the argument [15]. The other possibilities are to combine the D-decomposition method with the classical one or (the best, if possible) to use a degenerate value of the parameter, for which the system stability is known either from physical considerations or previous research.

To apply this method efficiently, the characteristic equation should contain a parameter that can be expressed explicitly. Characteristic equations of pipes conveying fluid do not necessarily contain such a parameter. By changing a boundary condition (extra mass, stiffness, dashpot, etc.), the boundary condition element enters the characteristic equation in such a way that it can be expressed explicitly as a function of all other system parameters. For the clamped-clamped and clamped-pinned pipe the rotational spring is introduced for this purpose at right end of the pipe, see Figure. (1) and Eq. (9). If the stiffness of this spring is zero, then the clamped-pinned pipe is retrieved. On the other hand, if this stiffness tends to infinity, the right end of the pipe becomes fixed. The characteristic equation for the pipe at hand consist of two parts, one proportional to the dimensionless rotational stiffness K and the other part independent of this stiffness:

$$\Delta = KA(\Omega) + B(\Omega) = 0 \tag{22}$$

Where A and B are functions of Ω obtained by using the relationship between the wave numbers g_j and the eigenvalues λ (Eq. (19)) and the expression $\lambda = i\Omega$. Expressing the rotational stiffness from Eq. (22), the rule is obtained for mapping the imaginary axis of the λ-plane on to the plane of the parameter K:

$$\boldsymbol{K} = -\frac{\boldsymbol{B}(\Omega)}{\boldsymbol{A}(\Omega)} \tag{23}$$

Note that in complex K-plane the positive part of the real axis only has physical meaning, since K is the stiffness of the rotational spring.

5. Finite Element Modeling Procedure

The FE analysis was carried out to calculate vibration characteristics of a welded pipes conveying fluid with different velocities and boundary conditions using a general purpose FE package ANSYS V9.0. The approach is divided into five parts: thermal analysis, coupled field thermal-structure analysis, computational fluid dynamics (CFD), coupled field fluid-structure analysis, and modal analysis.

5.1. Thermal analysis

A non- linear transient thermal analysis was conducted first to obtain the global temperature history generated during and after welding process(at the weld region). The basis for thermal analysis is a heat balance equation obtained from the principle of conservation of energy. The FE thermal solution employed a nonlinear (material properties depend on temperature) transient thermal analysis using two modes of heat transfer: conduction, and convection, to determine temperatures distributions that vary over time. The applied loads at the region of weld are function of time which described by divided the load-versus-time curve into load steps. For each load step, its need to specify both load and time values, along with other load step options such as stepped or ramped loads, automatic time stepping, etc. It's then written each load step to a file and solves all load steps together. SOLID90 element type is used, which it is a 3-D twenty nodes with a single degree of freedom, temperature, at each node. The 20-node elements have compatible temperature shapes and are well suited to model curved boundaries. It is applicable to a 3-D, steady-state or transient thermal analysis, Figure.(2) shows the model geometry and the mesh of the model

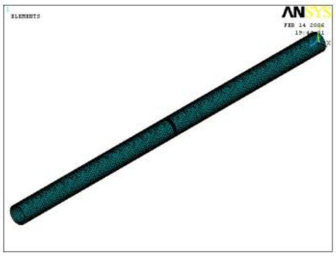

Figure 2. model geometry and the mesh

5.2. Coupled Field Thermal-Structure

A stress analysis was then developed with the temperatures obtained from the thermal analysis used as loading to the stress model. SOLID95 element type was used, which it can tolerate irregular shape without as much loss of accuracy. SOLID95 element has compatible displacement shapes and is well suited to model curved boundaries. It is defined by 20 nodes having six degree of freedom per node. The element may have any spatial orientation. SOLID95 has plasticity, creep, stress stiffening, large deflection, and large strain capabilities

5.3. Computational fluid dynamics (CFD)

The ansys flotran analysis used to solve 3-D flow and pressure distributions in a single phase viscous fluid. For the FLOTRAN CFD elements FLUID142, the velocities are obtained from the conservation of momentum principle, and the pressure is obtained from the conservation of mass principle. A segregated sequential solver algorithm is used; that is, the matrix system derived from the finite element discretization of the governing equation for each degree of freedom is solved separately. The flow problem is nonlinear and the governing equations are coupled together. The sequential solution of all the governing equations, combined with the update of any pressure dependent properties, constitutes a global iteration. The number of global iterations required to achieve a converged solution may vary considerably, depending on the size and stability of the problem.

5.4. Coupled field fluid-structure analysis

The coupled field fluid-structure analysis solved the equations for the fluid and solid domains independently of each other. It transfers fluid forces and solid displacements, velocities across the fluid-solid interface. The algorithm continues to loop through the solid and fluid analyses until convergence is reached for the time step (or until the maximum number of stagger iterations is reached). Convergence in the stagger loop is based on the quantities being transferred at the fluid-solid interface.

5.5. Modal analysis

We used modal analysis to determine the vibration characteristics (natural frequencies and mode shapes) of a welded pipe conveying fluid. The natural frequencies and mode shapes are important parameters in the design of a structure for dynamic loading conditions. The procedure to do a prestressed modal analysis is essentially the same as a regular modal analysis, except that you first need to prestress the structure by doing a static analysis:

Build the model and obtain a static solution with prestress effects turned on from thermal-structure and fluid-structure analyses.

- Reenter the solution and obtain the modal solution, also with prestress effects turned on from thermal-structure and fluid-structure analyses.
- Expand the modes and review them in the postprocessor.

in a modal analysis, however, we use the term "expansion" to mean writing mode shapes to the results file. Figure 3 shows a flow chart for solution algorithm of modal analysis.

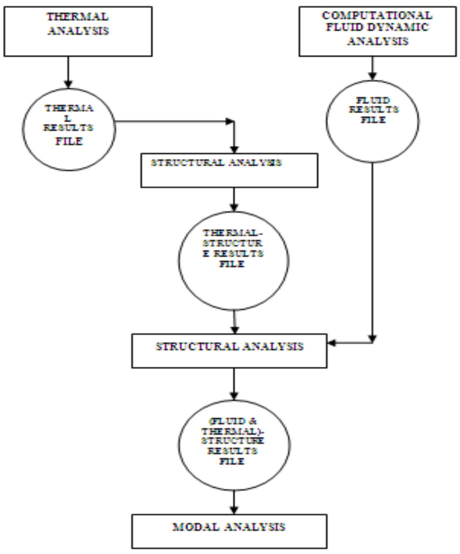

Figure 3. Modal solution algorithm for welded pipe conveying fluid

6. Experimental Work

The experimental procedures for measuring the natural frequencies were carried out with different steps:

- Pipes without flowing fluid

The vibration characteristics measurement was first done on a straight pipe 1m length, 50.8 mm diameter with clamped-pinned support without welding. The natural frequencies were measured by varying the shaker frequency slowly until a sharp increasing in the tube response that was displayed on the oscilloscope occurred. The same procedure was repeated by taking two straight pipe 0.5m length welded together by a single pass fusion arc welding with a current of 30A and voltage equal 460 volt using an electrode type E7010-G, to make a straight pipe 1m length with welding on its mid span. This was performed to investigate the effects of welding on the first few natural frequencies of a pipe.

- Pipes with flowing fluid

The vibration characteristic measurements were performed on straight pipe 1m length (without welding and with welding on its mid span) conveying water at a constant speed. To obtain a steady-state, we operate the centrifugal pump for enough time before began the measurements. This procedure was carried out with different flow velocities, which controlled by the valve. Another models were tested using the same previous procedures but with different lengths, diameters, welding position, and boundary conditions. figureure 4.Shown a schematic diagram for the experimental setup.

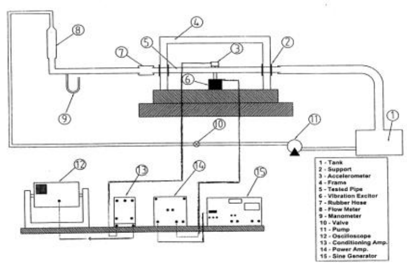

Figure 4. Schematic diagram of experimental setup

7. Results and Discussions

The pressure and velocity distributions in a pipe conveying fluid (water) are shown in figures. (5) and (6). The fluid is assumed water entered a pipe with a non-dimensional velocity (V=2) and a non-dimensional pressure (β=2), and Reynolds number 9.14*106. The outlet pressure is atmospheric pressure. The fluid forces and solid displacements, velocities was transferred across the fluid-solid interface to produce stresses distributed along the pipe geometry.

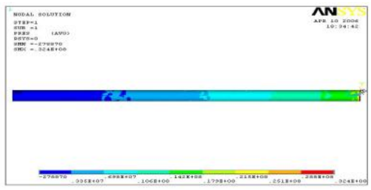

Figure 5. Pressure distribution along a pipe

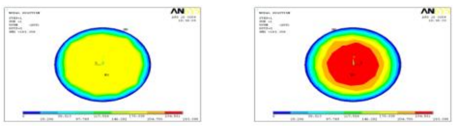

(a) (b)

Figure 6. Velocity distribution at pipe sections

a- inlet of the pipe b- outlet of the pipe

Figures. (7) and (8) shows the displacement vector sum, Von Mises stress, and Von Mises total strain due to flowing fluid (water) for both clamped-clamped and clamped-pinned boundary conditions respectively. The results of clamped-clamped and clamped-pinned pipes obtained from free vibration analysis under steady flow are studied. The analytical and finite element analyses are applicable to determine natural frequencies and mode shape of a vibrating system before and after welding, and then compared with the experimental results. The sample of calculations was made on a single mild steel pipe with a (1 m) length, (50.8 mm) outer diameter, and a (1.5 mm) thickness, while the welded pipe was formed by joining two (0.5 m) pipes by single pass fusion arc welding with a current of 30 A and voltage equal 460 volt using an electrode type E7010-G to make a straight pipe 1m length with welding on its mid span; the welding procedure was modeled as a single pass in this analysis. Water was supplied to the pipe from an external reservoir; the parameters used in the calculations are listed in table (1). The analytical analysis is performed using Matlab V6.5 software to determine natural frequencies and mode shape. The program was developed to be used for any specified pipe dimensions, length, pipe material stiffness, different flow velocities, and welding specifications

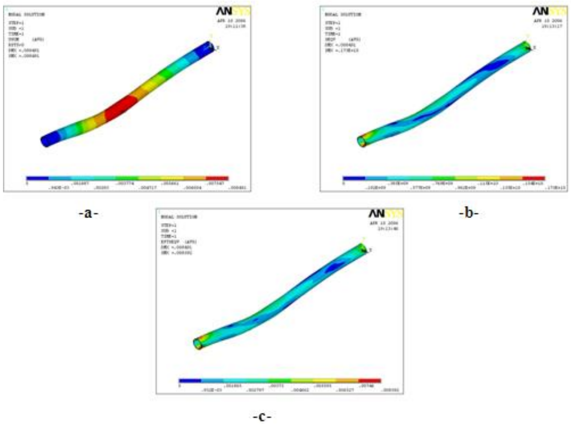

Figure. 7. clamped-clamped boundary conditions

a- Displacement vector sum b- Von Mises stress c- Von Mises total strain

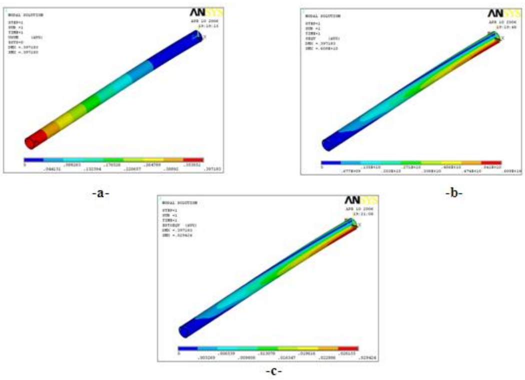

Figure 8.clamped-pinned boundary conditions

a- Displacement vector sum b- Von Mises stress c- Von Mises total strain

Table (1) Parameters used in the calculation

EI	1.4122*104	Nm
mf	1.795	Kg/m
m	3.608	Kg/m
R	25.4	mm
Teff	$3.0243*10^5$	N
L	1	m
ρf	1000	Kg/m^3
β	21.41	
α	3.264	
Reynolds no.	$9.14*10^6$	

8. -Pipe Without Flowing Fluid

8.1. Clamped-Clamped Pipe

Table (2) shows the natural frequencies of a clamped-clamped pipe with and without welding obtained by finite element analysis and experiments, it shows good agreement between these results. We can see that the welding of a pipe causes reduction in the natural frequencies of it. This result is new and important to explain the effect of welding on the vibration characteristics of a pipe without flowing fluid. Figure. (9) Shows the mode shapes of a clamped-clamped pipe with and without welding.

Table (2) Natural frequencies (Hz) of a clamped-clamped pipe with and without welding

Mode no.	Without welding			With welding		
	FE analysis	Experimental work	% error	FE analysis	Experimental work	% error
1st	308.726	290	6.2	302.47	285	5.69
2nd	815.086	850	-4.1	799.37	840	-4.83
3rd	1518	1440	5.41	1489.6	1400	6.42

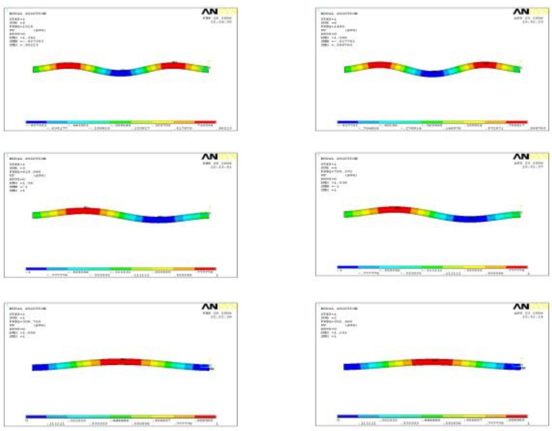

(a) *(b)*

Figure 9. Mode shapes of a clamped-clamped pipe with and without welding

a- without welding b- with welding

8.2. Clamped-Pinned Pipe

Table (3) shows the natural frequencies of a clamped-pinned pipe with and without welding obtained by finite element analysis and experiments, it shows good agreement between these results. Also we can see that the welding of a pipe causes reduction in the natural frequencies of it. This result is also new and important to explain the effect of welding on the vibration characteristics of a pipe without flowing fluid. Figure. (10) Shows the mode shapes of a clamped-pinned pipe with and without welding**.**

Table (3) Natural frequencies (Hz) of a clamped-pinned pipe with and without welding

Mode no.	Without welding			With welding		
	FE analysis	Experimental work	% error	FE analysis	Experimental work	% error
1st	215.916	200	8.0	212.19	195	8.8
2nd	676.339	725	-6.71	664.78	710	-6.36
3rd	1349	1250	7.92	1325	1220	8.6

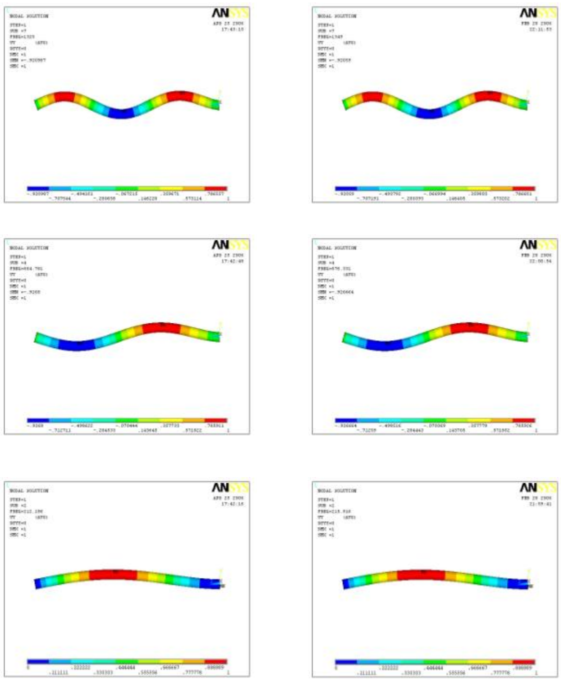

(a) (b)

Figure 10.Mode shapes of a clamped-pinned pipe with and without welding

a- without welding b- with welding

9. Pipe with Flowing Fluid

The fluid parameters (velocity, pressure, and mass ratio) have direct effects on the dynamic characteristics of the system in consideration. The effect of the fluid flow velocity and mass ratio will be discussed. In general the natural frequencies for steady flow decreases with increasing the fluid flow velocity as shown in figure. (11). If the velocity of the flow in the pipe equal zero, then the case will be a normal beam system and when the flow velocity equal the critical velocity the pipe bows out and buckles, because the forces required to make the fluid deform to the pipe curvature is greater than the stiffness of the pipe. Mathematically the buckling instability arises from the mixed derivative term in equation (5) which represent a forces imposed on the pipe by the flowing fluid that always 90o of phase with the displacement of the pipe, and always in phase with the velocity of the pipe. This force is essentially a negative damping mechanism which extracts energy from the fluid flow and inputs energy into the bending pipe to encourage initially, vibration, and ultimately buckling [16].

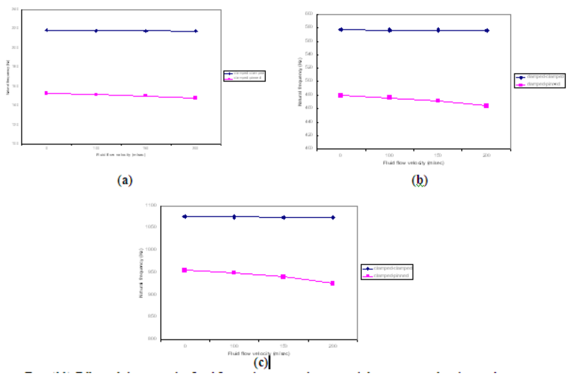

Figure 11. Effect of changing the fluid flow velocity on the natural frequencies of a clamped-clamped and clamped-pinned welded pipe

a-first mode b-second mode c-third mode

9.1. Super-Critical Velocity

In this case, a comparison is made between the analytical and finite element, because the available pump in the market cannot gives high velocity (maximum fluid velocity = 5 m/sec).

9.2. Clamped-Clamped Pipe

Table (4) shows the natural frequencies of a clamped-clamped pipe with and without welding flowing water as a fluid with a non-dimensional velocity (V=2) obtained by analytical and finite element analysis; it shows good agreement between these results. Figure. (12) Shows the mode shapes of the pipe obtained analytically and by finite element analysis**.**

Table (4) Natural frequencies (Hz) of a clamped-clamped pipe with and without welding flowing water (V=2)

Mode no.	Without welding			With welding		
	Analytical analysis	FE analysis	% error	Analytical analysis	FE analysis	% error
1st	216.62	217.832	0.55	212.7	213.981	0.6
2nd	573.83	576.172	0.4	564.58	566.091	0.26
3rd	1069.3	1074	0.43	1050.55	1055	0.42

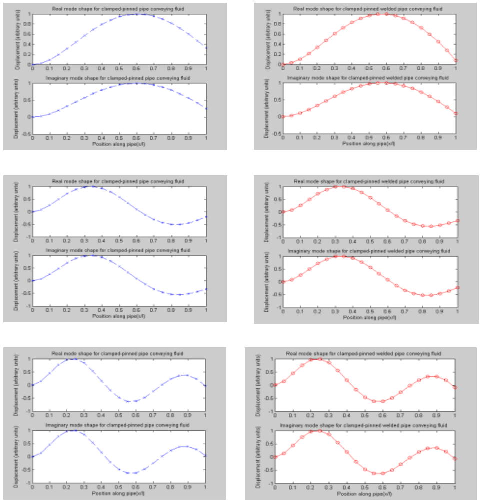

(a) (b)

Figure 12. Mode shapes of a clamped-clamped pipe with flowing water (V=2)

a- without weld b- with weld

10. Clamped-Pinned Pipe

Table (5) shows the natural frequencies of a clamped-pinned pipe with and without welding, flowing water with a non-dimensional velocity (V=2) obtained by analytical and finite element analysis; it shows good agreement between these results. Figure. (13) Shows the mode shapes of the pipe obtained analytically and finite element analysis. We can see that the welding of a pipe leading to reduce the natural frequencies of a pipe conveying fluid for both clamped-clamped and clamped-pinned boundary conditions. This result is new and important to explain the effect of welding on the vibration characteristics of a pipe conveying fluid**.**

Table (5) Natural frequencies (Hz) of a clamped-pinned pipe with and without welding flowing water (V=2)

Mode no.	Without welding			With welding		
	Analytical analysis	FE analysis	% error	Analytical analysis	FE analysis	% error
1st	148.9	149.182	0.19	147.68	148.224	0.36
2nd	465.04	467.672	0.56	462.82	465.05	0.48
3rd	930.77	935.59	0.51	925.9	932.323	0.69

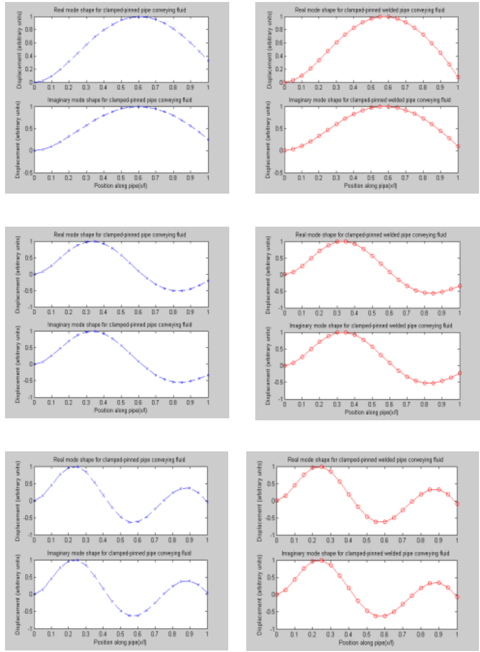

(a) **(b)**

Figure 13.Mode shapes of a clamped-pinned pipe with flowing water (V=2)

a- without weld b- with weld

11. Sub-Critical Velocity

For low water velocity (V=0.5), the results are summarized in table (6) for clamped-clamped and table (7) for clamped-pinned pipe conveying water (with and without welding). The comparison was made between analytical, finite element, and experimental, it shows good agreement between them and the error percentage is within ranges shown in literatures.

Table (6) Natural frequencies (Hz) of a clamped-clamped pipe with flowing water with a non-dimensional (V=0.5)

Mode no.	Without welding			With welding		
	analytical	finite element	experimental	analytical	finite element	experimental
1st (error)	218.3 (6.48%)	219.65 (7.14%)	052	217.4 (8.7%)	218.7 (9.35%)	002
2nd (error)	575.21 (4.58%)	577.3 %)4.96(	055	573.26 (6.15%)	574.13 (6.32%)	540
3rd (error)	1070 (-6.7%)	1075.8 (-6.2%)	1147	1060 (-7.01%)	1064.8 (-6.59%)	1140

Table (7) Natural frequencies (Hz) of a clamped-pinned pipe with flowing water with a non-dimensional (V=0.5)

Mode no.	Without welding			With welding		
	analytical	finite element	experimental	analytical	finite element	experimental
1st (error)	151.8 (4.68%)	152.9 (5.44%)	145	149.6 (3.17%)	150.38 (3.7%)	145
2nd (error)	477 (6.0%)	479 (6.4%)	450	465 (5.68%)	470.99 (7.0%)	440
3rd (error)	952.7 (-4.53%)	954.3 (-4.37%)	998	934.36 (-4.94%)	939.21 (-4.45%)	983

12. Effect of Weld Position on the Vibration Characteristics

The effect of weld position on the natural frequencies was examined using finite element for clamped-clamped and clamped-pinned welded pipe conveying water with a steady non-dimensional velocity (V=2). The result shows that as the position of welding far from the stationary edge, the natural frequencies reduced more. Figure. (14) Shows the effect of weld position clearly.

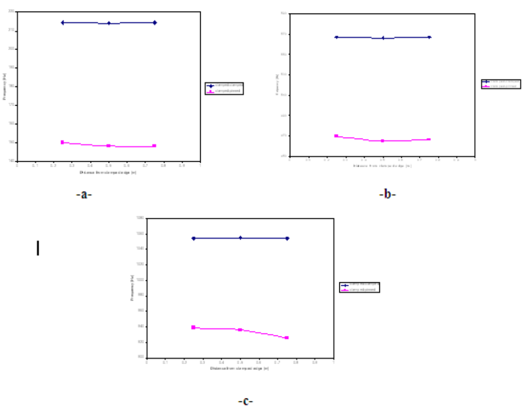

Figure 14. Effect of weld position on natural frequencies of welded pipe conveying fluid
a- first mode b- second mode c- third mode

13. Stability of A Welded Pipe Conveying

The stability of welded pipe conveying fluid using the D-decomposition method via Matlab V6.5 software. The result of D-decomposition of the k-plane is shown in Figure. (15) for two fluid speeds V=0.5 (sub-critical) and V=2 (super-critical), respectively. Figure. (15-a) shows that in the sub-critical case, V=0.5, the D-decomposition lines do not cross the positive part of the real axis. This implies that the number of "unstable" eigenvalues does not depend on the rotational stiffness of the pipe's support (the physically admissible values of this stiffness are real and positive). In particular, this implies that the number of unstable roots for the clamped-clamped pipe ($k \to \infty$) is the same as for the clamped-pinned pipe (k=0). Thus, since it is well known [12] that the clamped-clamped and clamped-pinned pipes are stable at small fluid speeds; we can conclude that the clamped-clamped and clamped-pinned welded pipes are stable at these speeds as well.

The main difference between Figures. (15-a) and (15-b) is that in the former figureure the D-decomposition curves cross the positive part of the real axis. This implies that there is a critical stiffness of the rotational spring (the coordinate of the crossing point) below which the pipe is for sure unstable. Thus, if the flow is super-critical (V=2), the clamped-pinned welded pipe is unstable. The critical velocity corresponds to the situation, when the D-decomposition curves cross the origin of the k-plane.

14. Conclusions

Theoretical analysis and experimental work are used to determine the effect of welding on the vibration characteristics and stability of a welded pipe conveying fluid. The main summarized conclusions are:

- The natural frequencies of a welded pipe with steady flow decreases with increasing the fluid flow velocity in both clamped-clamped and clamped-pinned boundary conditions.
- The welding of a pipe leading to reduce the natural frequencies of a pipe conveying fluid for both clamped-clamped and clamped-pinned boundary conditions.
- The natural frequencies affected by the position of weld. They are reduces more as the position of welding far from the stationary edge for both clamped-clamped and clamped-pinned boundary conditions.
- The welded clamped-clamped and clamped-pinned pipes are stable for small fluid velocities (sub-critical), and the clamped-pinned pipe lose stability by divergence at relatively high fluid velocities (super-critical).

References

[1] Amabili M., Pellicano F. and Paidoussis M.P., " Non-linear dynamics and stability of circular cylindrical shells containing flowing fluid, Part I: Stability ", Journal of Sound and Vibration, Vol. 225, 1999, 655-699.

[2] Manabe T., Tosaka N. and Honama T., " Dynamic stability analysis of flow-conveying pipe with two lumped masses by domain decomposition beam ", Fuji Research Institute Corp., Tokyo, Japan, 1999.

[3] Amabili M., Pellicano F. and. Paidoussis M.P, " Non-linear dynamics and stability of circular cylindrical shells containing flowing fluid, Part IV: large-amplitude vibrations with flow ", Journal of Sound and Vibration, Vol. 237, 2000, 641-666.

[4] Yih-Hwang Lin and Chih-Liang Chu, " Active modal control of Timoshinko pipes conveying fluid ", Journal of the Chinese Institute of Engineers, Vol.24, No.1, 2001, 65-74.

[5] Nawaf M. Bou-Rabee, "Numerical stability analysis of a tubular cantilevered conveying fluid ", California Institute of Technology, 2002.

[6] Lee S. I. and Chung J., "New non-linear modeling for vibration analysis of a straight pipe conveying fluid ", Journal of Sound and Vibration, Vol. 254, 2002, 313-325.

[7] Reddy J.N. and Wang C.M., "Dynamics of fluid-conveying beams ", Centre of offshore research and engineering, National University of Singapore, August, 2004.

[8] Kuiper G.L. and Metrikine A.V., "On stability of a clamped-pinned pipe conveying fluid ", Heron, Vol. 49, No.3, 2004, 211-231.

[9] d e Langre E., Paidoussis M. P., Doare O. and Modarres – Sadeghi Y., " Flutter of long flexible cylinders in axial flow", J. Fluid Mechanics, October, 2005.

[10] Al-Rajihy A.A., "Out-of-plane vibration of an intermediately supported curved tube conveying fluid ", M.Sc. Thesis, 1990.

[11] Adnan N. Jameel, Nabeel K. Abid Al-Sahib, and Osamah F. Abdulateef,"Residual Stress Distributions for a Single Pass Weld in pipe", Journal of Engineering College, under press, 2007.

[12] Paidoussis M.P., " Fluid-structure interactions: slender structures and axial flow ", Vol.1, Academic Press, London, 1998.

[13] [13] Neimark Yu. I., "Dynamic systems and controllable processes ", Nauka, Moscow, Russia, 1978.

[14] Neimark Yu.I., Golumov V.I., Kogan M.M., "Mathematical models in natural science and engineering ", Springer, Berlin, 2003.

[15] Metrikine A.V. and Verichev S.N., " Instability of vibrations of a moving two-mass oscillator on a flexibly supported Timoshinko beam", Archive of Applied Mechanics, Vol. 71, 2001, 613-624.

[16] Blevens D., "Flow-induced vibration ", New York, Van Nostrand Reinhold Co., 1977.

JJMIE

Volume 4, Number 3, June, 2010
ISSN 1995-6665
Pages 388 - 393

Jordan Journal of Mechanical and Industrial Engineering

Reliability Analysis of Car Maintenance Scheduling and Performance

Ghassan M. Tashtoush[a,*], Khalid K. Tashtoush, Mutaz A. Al-Muhtaseb[a], Ahmad T. Mayyas[b]

[a]*Mechanical Engineering Department, Faculty of Engineering,Jordan University of Science and Technology, Irbid, 22110, Jordan*

[b] *Clemson University–International Center for Automotive Research ,CU–ICAR, 340 Carroll Campbell Jr. Graduate Engineering Center CGEC, Greenville, SC 29607, USA*

Abstract

In car maintenance scheduling and performance control, researchers have mostly dealt with problems either without maintenance or with deterministic maintenance when no failure can occur. This can be unrealistic in practical settings. In this work, a statistical model is developed to evaluate the effect of corrective and preventive maintenance schemes on car performance in the presence of system failure where the scheduling objective is to minimize schedule duration. It was shown that neither scheme is clearly superior, but the applicability of each depends on the scheduling environment itself. Furthermore, we showed that parameter values can be chosen for which preventive maintenance does better than corrective maintenance. The results provided in this study can be useful to practitioners and to system machine administrators in car maintenance scheduling and elsewhere.

Keywords: Car Maintenance scheduling; Mean Time to failure MTTF; Performance Weibull probability.

Nomenclatures

F(t)	Unreliability function
MTTF	Mean time to failure
MDTF	Mean distance to failure
TOR	Time of repairing
R(t)	Reliability function
η	Scale time parameter
β	the slope of the weibull graph
t	Time (hr)
λ	The mean failure rate

1. Intoduction

in car maintenance scheduling performance control, good bounds are available for the problem of minimizing schedule durations, or the make span. Graham [1] provided the worst-case bound for the approximation algorithm, Longest Processing Time, and Coffman, Garey and Johnson [2] provided an improved bound using the heuristic, multifit. By combining these, Lee and Massey [3] were able to obtain an even tighter bound. These studies, however, assumed the continuous availability of machines, which may not be justified in realistic applications where machines can become unavailable due to deterministic or random reasons.

It was not until the late 1980's that research was carried out on machine scheduling with availability constraints. In a study, Lee [4] considered the problem of parallel machine scheduling with non-simultaneous available time. In another work, Lee [5] discussed various performance measures and machine environments with single unavailability. For each variant of the problem, a solution was provided using a polynomial algorithm. Turkcan [6] analyzed the availability constraints for both the deterministic and stochastic cases. Qi, Chen and Tu [7] conducted a study on scheduling the maintenance on a single-machine. The reader is referred to Schmidt [8] for a detailed literature review of machine scheduling with availability constraints. Other work on scheduling with maintenance is available, but with different scheduling environments and/or objectives. Lee and Liman [9] studied single-machine flow-time scheduling with maintenance while Kaspi and Montreuil [9] attempted to minimize the total weighted completion time in two machines with maintenance. Schmidt [8] discussed general scheduling problems with availability constraints, taking into account different release and due dates in a recent work.

These studies addressed the problem of maintenance, but in a limited way. They either considered only one deterministic maintenance (or availability) constraint or maintenance without machine failures. The results, however, are inadequate for solving real problems. Industrial systems, like automotive or machines, can fail due to heating or lack of lubrication, for example; in computer systems, the Internet is a typical example of system instability and breakdowns due to both hardware and software problems. In such cases, maintenance needs to be carried out, either periodically or after failure. Yet, even with maintenance, failures are not completely eliminated. Furthermore, the overall performance, in

*Corresponding author. gtash@just.edu.jo

 © 2010 Jordan Journal of Mechanical and Industrial Engineering. All rights reserved - Volume 4, Number 3 (ISSN 1995-6665)

addition to its being the worst-case performance, is of greater relevance to the users and administrators of these systems.

In this work, we address this need and study the expected maintenance scheduling performance with both maintenance and failures. Since maintenance as well as failure is everyday occurrences in these systems, this study is particularly relevant to practitioners and systems administrators.

2. Methodology and Procedure

Data were collected from a private company that faced a problem in reliability analysis of car maintenance scheduling performance. Firstly, the data were analyzed, and rearranged according to the car systems (brake, steering, clutch, injection and cooling systems respectively) and according to the common troubleshooting method followed as shown in the figures 2, 4, 6, 8 and 10. Secondly, the traditional standard maintenance technique that is used in car maintenance companies and machine maintenance was applied to choose the best statistical analysis approach. In analyzing the collected data, the Weibull distribution was selected and applied according to several characteristics that make Weibull distribution the best distribution method to be used for these data.

The primary advantage of Weibull analysis is the ability to provide reasonably accurate failure analysis and failure forecasts with extremely small samples. Another advantage of Weibull analysis is that it provides a simple and useful graphical plot. The data plot is extremely important to the engineer and to the manager [Montgomery and Runger 2003]

Many statistical distributions were used to model various reliability and maintainability parameters. Whether to use one distribution or another is highly depending on the nature of the data being analyzed. Some commonly used statistical distributions are:

1. Exponential and Weibull. These two distributions are commonly used for reliability modeling – the exponential is used because of its simplicity and because it has been shown in many cases to fit electronic equipment failure data. On the other hand, Weibull distribution is widely used to fit reliability and maintainability models because it consists of a family of different distributions that can be used to fit a wide variety of data and it models, mainly wearout of systems (i.e., an increasing hazard function) and in electronic equipment failures.
2. Tasks that consistently require a fixed amount of time to complete with little variation. The lognormal is applicable to maintenance tasks where the task time and frequency vary, which is often the case for complex systems and products.

3. Results and Discussion

The aim of using the traditional technique for car maintenance is to calculate reliability function of time R(t) of the overall system (the car). This was done by calculating R(t) for each subsystem in the car parallel to the other.

For calculating the reliability function R(t) for each system, the collected data were converted from Mean Distance To Failure (MDTF) to Mean Time To Failure (MTTF). This is because the reliability function which was used in this study is a function of time, where the reliability decreases as time increases. Hence, the Unreliability function F(t) increases as time increases, which leads to the logic relation

$$F(t) + R(t) = 1.0 \tag{1}$$

R(t), MTTF and the mean failure rate (λ) were calculated for each system according to the following relations [10]:

$$R(t) = \exp(-\lambda \times t) = \exp\left\{\frac{-(t-t_0)}{\eta}\right\}^{\beta} \tag{2}$$

Where t is time, t_0 is initial time, β is slope and η is scale time parameter. By combining to Equations 1 and 2:

$$F(t) = 1 - \exp(-\lambda \times t) = 1 - \exp\left\{\frac{-(t-t_0)}{\eta}\right\}^{\beta} \tag{3}$$

For calculating λ(t), η was calculated by setting the initial time for all subsystems equal to zero. Therefore, F(t) = (1- e^t) =0.632. Then, the unreliability function was drawn on a Weibull probability graph paper as a straight line to estimate η (scale time parameter) from the intersection of the line with the x-axis, and β from the slope of the line plotted for each system as shown in the figures 3, 5, 7, 9 and 11. Then, F(t) was found for each subsystem by applying Equation1. The slope of the Weibull plot, beta, (β), determines which member of the family of Weibull failure distributions best fits or describes the data. The slope, β, also indicates which class of failures is present:

$\beta < 1.0$ indicates infant mortality

$\beta = 1.0$ means random failures (independent of age)

$\beta > 1.0$ indicates wear out failures

A comparison between the preventive time maintenance from the company database and fro

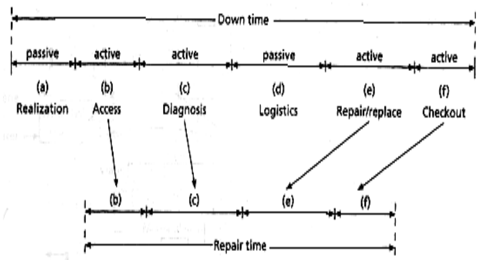

Figure 1. the difference between down time and Repair time

statistical approach was performed; and recommendations were reported to the car company to change preventive time maintenance of the company database to that obtained from statistical approach.

In addition to the above analysis, Unreliability test was made for the overall system, and this was by considering each system work separate to the other (parallel to the other), and this leading to the following equation:

$$F_{(system)} = F_1 \times F_2 \times F_3 .... F_j ... F_n \qquad (4)$$

For this approach, the real primitive time maintenance was found to make the car Reliable and Available every time of use and this is safe time significantly comparing to break down maintenance as in graph.

The results were divided in a sequins way for each system:

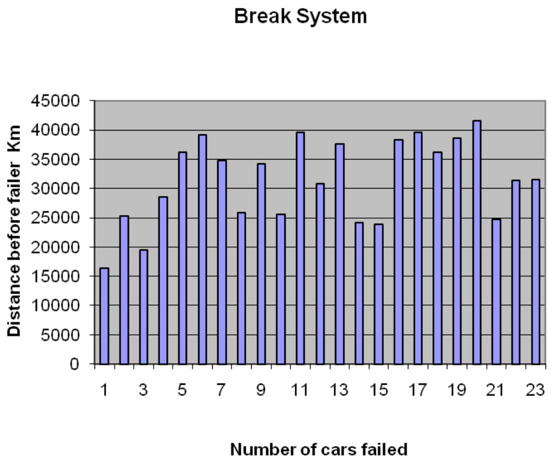

Figure 2. A bar diagram of the brake system data used in the analysis.

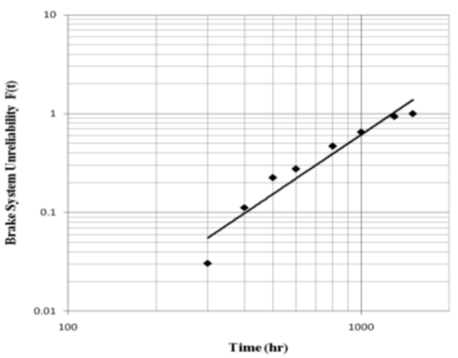

Figure 3. Brake system unreliability data plotted on a Weibull probability graph

η (Scale Parameter) = 1000 hr

β from slope =1.5

Results from statistics analysis:

Total Average of Distance between Failure (Km) = 23688.56

Mean Time to Failure (MTTF) =296.107

Failure rate model (λ) =0.003377 {means very good}

Time of repairing (TOR) = 0.5 hr

Reliability Failure model (R(t))= 0.9969 (at 15 000 Km)

Un-reliability Failure model F(t) =0.0030

R(t)= .85 at Distance= 20000 Km {primitive distance from company}

From statistical analysis and actual data Distance=15 000Km

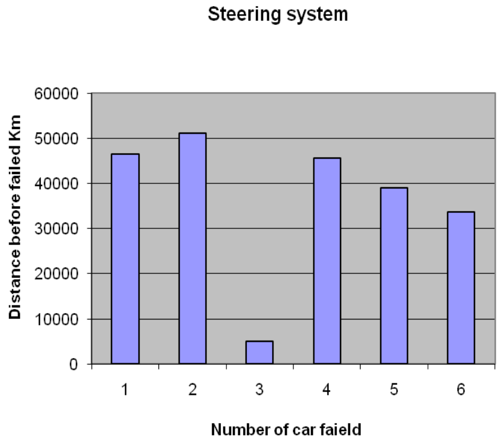

Figure 4. A bar diagram of the steering system data used in the analysis

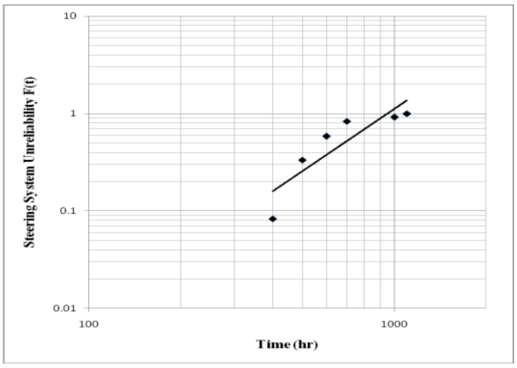

Figure 5. Steering system unreliability data plotted on a Weibull probability graph

η (Scale Parameter) =650 hr

β from slope = 2.4

Results from statistics analysis:

Total Average of Distance between Failure (Km) = 100367.9

Mean Time to Failure (MTTF) = 1254.599

Failure rate model (λ) = 0.000797{means very good}

Time of repairing (TOR) = 2 hr

Reliability Failure model R(t) =0.8612 (at 15 000 Km)

Un-reliability Failure model F(t) = 0.1388

R(t)= 0.68 at Distance= 40 000 Km {primitive distance from company}

From statistical analysis and actual data Distance=15 000Km

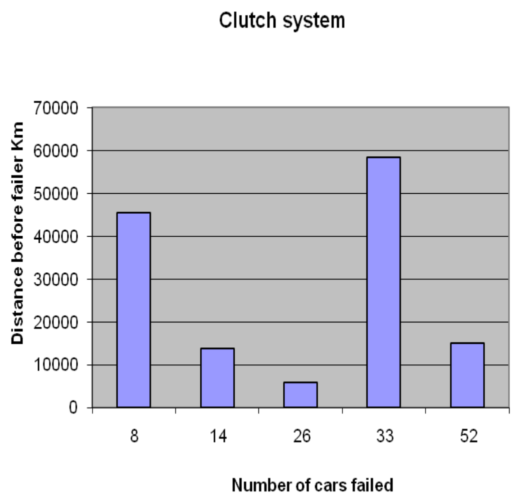

Figure 6. A bar diagram of the clutch system data used in the analysis steering

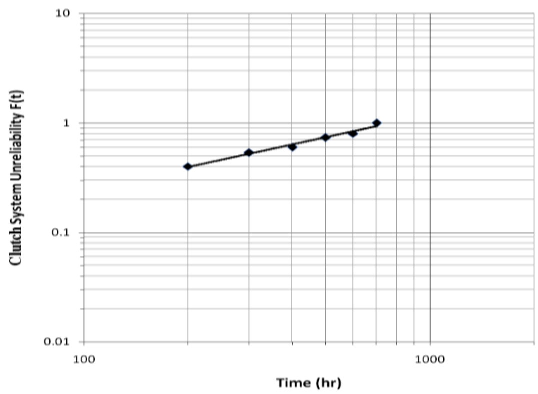

Figure 7. Clutch system unreliability data plotted on a Weibull probability graph

η (Scale Parameter) =580 hr

β from slope = 1.7

Results from statistics analysis:

Total Average of Distance between Failure (Km) = 112367

Mean Time to Failure (MTTF) =384.9573

Failure rate model (λ) = 0.002598{means very good}

Time of repairing (TOR) = 0.4 hr

Reliability Failure model R(t) =0.699 (at 15 000 Km)

Un-reliability Failure model F(t) = 0.301

R(t)=0.133 at Distance= 10 000 Km {primitive distance from company}

From statistical analysis and actual data Distance=15 000Km.

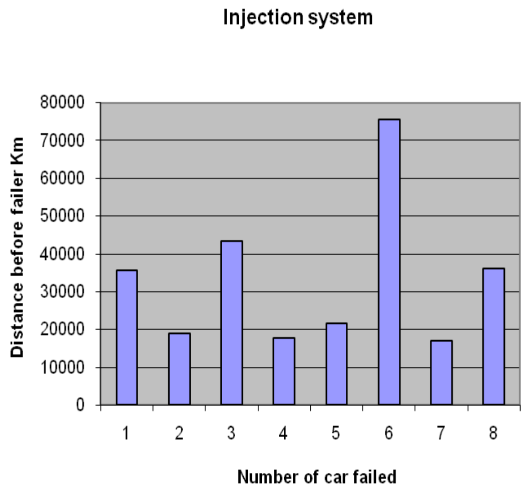

Figure 8. A bar diagram of the injection system data used in the analysis

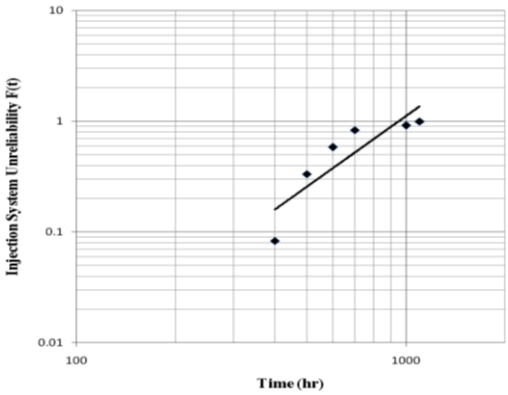

Figure 9. Injection system unreliability data plotted on a Weibull probability graph

η (Scale Parameter) = 680 hr

β from slope = 2.4

Results from statistics analysis:

Total Average of Distance between Failure (Km) =38930.54

Mean Time to Failure (MTTF) =486.6318

Failure rate model (λ) = 0.002055{means very good}

Time of repairing (TOR) = 0.5 hr

Reliability Failure model (R(t)) = 0.9709 (at 15 000 Km)

Un-reliability Failure model F(t) = 0.0291

R(t)=.99 at Distance= 10 000 Km {primitive distance from company}

From statistical analysis and actual data Distance=15 000Km

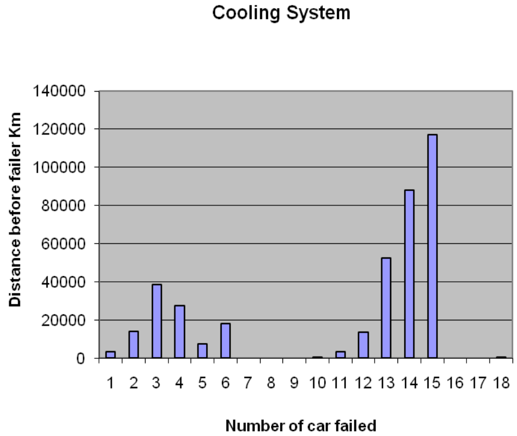

Figure 10. A bar diagram of the cooling system data used in the analysis

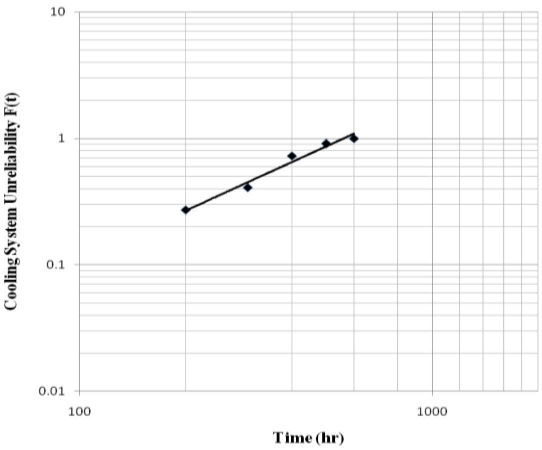

Figure 11. Cooling system unreliability data plotted on a Weibull probability graph

η (Scale Parameter) =620 hr
β from slope = 2.3
Results from statistics analysis:
Total Average of Distance between Failure (Km) = 23688.56
Mean Time to Failure (MTTF) =296.107
Failure rate model (λ 0.003377{means very good}
Time of repairing (TOR) = 0.5 hr
Reliability Failure model (R (t)) =0.642 (at 15 000 Km)
Un-reliability Failure model F (t) = 0.358
R (t) =0.42 at Distance= 4000 Km {primitive distance from company}
From statistical analysis and actual data Distance=15 000Km.
As a result of calculating the Un-reliability function for each system in the automobile based on the statistical analysis and actual data Distance =15 000Km the total un-reliability of the automobile (overall system) as given in equation 4 is calculated as
F(t) =0.0030 x 0.1388x 0.301x0.0291x0.358= 0.0000013

4. Conclusion

The primitive distance specified from the company was not matching the distance calculated from the statistical analysis based on the real data collected from the work shop. It was found for most of the automobile systems, 15000 -20000km was found to perfect distance for scheduling preventive maintenance to guarantee the reliability and the availability of the automobile for operation. It was assumed that all systems work in parallel, so if one system fails then the other systems still work independently. However, if we assumed all systems to work in series then it means that the overall system configuration will fail. This is not the case in this study. The effect of corrective and preventive maintenance schemes on car performance in the presence of system failure was proven to minimize schedule duration. It was shown that neither scheme is clearly superior, but the applicability of each depends on the scheduling environment itself. Further, we showed that parameter values can be chosen for which preventive maintenance does better than corrective maintenance. The results provided in this study can be useful to practitioners and to system machine administrators in car maintenance scheduling and elsewhere.

References

[1] R.L. Graham, "Bounds on multiprocessing timing anomalies". SIAM Journal of Applied Mathematics, Vol. 17, 1969, 263–269.

[2] E.G. Coffman Jr., M.R. Garey and D.S. Johnson, "An application of bin-packing to multiprocessor scheduling". SIAM Journal on Computing, Vol. 7, 1978, 1–17.

[3] C.Y. Lee and J.D. Massey, "Multiprocessor scheduling: Combining LPT and MULTIFIT". Discrete Applied Mathematics, Vol. 20, 1988, 233–242.

[4] C.Y. Lee, "Machine scheduling with an availability constraint". Journal of Global Optimization, Vol. 9, 1996, 395–416.

[5] C.Y. Lee, "Parallel machines scheduling with no simultaneous machine available time". Journal of Discrete Applied Mathematics, Vol. 30, 1991, 53–61.

[6] A. Turkcan, " Machine Scheduling with Availability Constraints". Available at: benli.bcc.bilkent.edu.tr/~ie672/docs/present/turkcan.ps, 1999.

[7] X. Qi, T. Chen and F. Tu,, "Scheduling the maintenance on a single machine". Journal of the Operational Research Society, Vol. 50, 1999, 1071–1078.

[8] G. Schmidt, "Scheduling independent tasks with deadlines on semi-identical processors". Journal of Operational Research Society, Vol. 39, 1988, 271–277.

[9] C.Y. Lee and S.D. Liman, " Single machine flow-time scheduling with scheduled maintenance". Acta Informatica, No. 92, 1929, 375–382.

[10] Montgomery D., and Runger J., Applied Statistics and Probability for Engineers, John Wiley and Sons, Inc 4the edition 2007.

JJMIE

Volume 4, Number 3, June, 2010
ISSN 1995-6665
Pages 394 - 403

Jordan Journal of Mechanical and Industrial Engineering

Dynamic Modeling and Simulation of MSF Desalination Plants

Awad S. Bodalal*, Sayed A. Abdul_Mounem, Hamid S. Salama

Mechanical Engineering Department, Faculty of Engineering, Garyounis University, Benghazi-Libya

Abstract

This paper describes the development of a mathematical model to predict the performance of multi-stage flash (MSF) plant systems under transient conditions. The model developed is based on coupling the dynamic equations of mass, energy and momentum. These equations describe the dynamic behavior of brine and product streams within the flashing stages, the effect of salinity and temperature variation on the specific heat, boiling point, enthalpy and density is accounted for in this model. The model which consists of a set of differential and algebraic equations (describing the dynamic behavior of each stage in terms of some key physical parameters) are solved by using the fifth order Runge-Kutta method. The proposed model was validated by using data from previous theoretical studies as well as actual data obtained from an operating MSF plant. The results obtained are useful for dynamic parametric studies and for the prediction of the performance of a given plant under a wide range of possible transient conditions.

Keywords. Desalination; MSF; Dynamic Modeling; Simulatio

Nomenclature

A_{BH}	Brine heater tube section area
$Cp_{b(i)}$	Specific heat of flashing brine stream exiting the ith stage
$Cp_{ba(i)}$	Specific heat of circulating brine exiting the ith stage
$Cp_{bd(i)}$	Specific heat of blow down
$Cp_{bg(i)}$	Specific heat of vapor flashing from brine pool in the ith stage
Cp_{BH}	Specific heat of brine in brine heater
$Cp_{C(i)}$	Specific heat of liquid condensing from the tubes in the ith stage
$Cp_{gv(i)}$	Specific heat of vapor in the ith stage
Cp_K	Specific heat of make up
$Cp_{pg(i)}$	Specific heat of vapor flashing from distillate tray in the ith stage
$Cp_{pr(i)}$	Specific heat of the product in the ith stage
$Cp_{V(i)}$	Specific heat of vapor in the ith stage
$h_{bg(i)}$	Enthalpy of vapor flashing from the brine pool in the ith stage
$h_{C(i)}$	Enthalpy of condensing from the cooling tubes in the ith stage
h_L	Enthalpy of condensate in the brine heater
$h_{pg(i)}$	Enthalpy of vapor flashing from distillate tray in the ith stage
h_S	Enthalpy of heating steam
i	Stage number
LT_{BH}	Brine heater tube length
$M_{B(i)}$	Mass hold-up of flashing brine in the ith stage
$m_{b(i)}$	Flashing brine flow rate from the brine pool in the ith stage
m_{bd}	Blow down flow rate
$m_{bg(i)}$	Rate of vaporization from the flashing brine pool in ith stage
M_{BH}	Mass hold-up in the brine heater
$m_{C(i)}$	Rate of condensing from the cooling tubes in the ith stage
$m_{gv(i)}$	Flow rate of vapor due to venting in the ith stage
m_k	Make up flow rate
m_L	Condensate flow rate
$m_{pg(i)}$	Rate of vaporization from the distillate tray in the ith stage
$M_{PR(i)}$	Mass hold-up of distillate in the ith stage
$m_{pr(i)}$	Distillate flow rate from the ith stage
m_S	Steam flow rate
$M_{V(i)}$	Mass hold-up of vapor in the ith stage
n	Last stage
$m_{wa(i)}$	Circulating brine flow rate brine in the ith stage
$M_{WA(i)}$	Mass hold-up for condenser tubes in the ith stage
NT_{BH}	Number of tubes in the brine heater
$T_{B(i)}$	Temperature of the mass hold-up in the flashing brine pool
$T_{b(i)}$	Temperature of flashing brine exiting the ith stage
T_{bd}	Temperature of blow down
$T_{bg(i)}$	Temperature of vapor flashing from the brine pool in the ith stage
$T_{C(i)}$	Temperature of liquid condensing from the tubes in the ith stage
$T_{gv(i)}$	Temperature of vapor in the vapor space in the ith stage

* Corresponding author. *drawadbodalal@hotmail.com*.

T_L	Temperature of condensate
$T_{pg(i)}$	Temperature of vapor flashing from the distillate tray in the ith stage
$T_{PR(i)}$	Temperature of the mass hold-up in the distillate tray
$T_{pr(i)}$	Temperature of distillate exiting the ith stage
T_S	Steam temperature
$T_{V(i)}$	Temperature of vapor in the ith stage
$T_{WA(i)}$	Temperature of the mass hold-up in the condenser tubes in the ith stage
$T_{wa(i)}$	Temperature of circulating brine exiting the ith stage
V_{BH}	Volume of the brine in the brine heater
$X_{B(i)}$	Salinity of flashing brine in the ith stage
$X_{b(i)}$	Salinity of flashing brine stream exiting the ith stage
X_{bd}	Blow down salinity
X_K	Make up flow rate salinity
$X_{WA(i)}$	Salinity of circulating brine in the ith stage
$X_{wa(i)}$	Salinity of brine in the condenser tubes exiting the ith stage
Greek	
ρ_{BH}	Brine density in the brine heater
ΔT	Log mean temperature difference

1. Introduction

In arid, water-scarce parts of the world, such as the Arab Gulf area and North Africa, multi-stage flash (MSF) desalination is considered one of the most common techniques that provide a considerable quantity of potable water. Massive amounts of seawater and therefore a similarly large quantity of energy are processed through these large, costly facilities. In that regard, considerable quantities of concentrated brine are disposed of after the desalination treatment. The aforementioned features of MSF plants make topics such as optimization of the operation and minimization of the corresponding environmental impact a main priority [1]. To the aim of addressing all these aspects, mathematical models provide a very useful tool. The steady state modeling of the MSF desalination plant has been the subject of various studies in the past; several publications for the steady-state simulation of desalination systems have been reported in literatures [2-4]. Due to the fact that the MSF desalination process has many input and output variables, it is difficult to model the dynamic behavior of the plant; but to design the instrumentation and control system to have better control on process variables, the knowledge of dynamics is necessary. The first attempt to obtain a dynamical model of an MSF-process was presented in [5]. The first attempt to obtain a dynamical model of an MSF-process was presented by Yokoyama et al. [6]. Viral et al. [7] carried out a dynamic model applying empirical corrections for the evaporation rates. The degrees of freedom based on a dynamic model were used to determine the number of controlled and manipulated variables. Thomas et al. [8] developed a mathematical model and its solution procedure to simulate the dynamic behavior of multi-stage flash desalination plants. The model was used to predict the operating parameters of an actual MSF plant. Theoretical models which simulate the transient behavior of MSF desalination plants under various conditions have been reported by Rimawi et al. [9]. Tarifa and Scenna [10], studied a dynamic simulator for MSF desalination plants, this simulator was developed to study the effects of faults that may affect a MSF system. Other models have also been proposed in [11-15]. In this way, for any process, the development of a dynamic simulator, which is able to simulate a dynamic process, is an interesting goal. Indeed, this dynamic simulator can be used fortraining operating personnel and investigating plant behavior under dynamic situations, which helps to predict the dynamic conditions of the plant in order to study potential operating modes and control behavior. Therefore, this work outlines the development and performance of a simulator able to simulate a dynamic process, specifically aimed to MSF processes at start-up, this simulator was developed to investigate the effects of changing the characteristics of the plant that may affect a MSF system at start up

2. MSF Process Description

MSF desalination is an evaporating and condensing process. The heat energy required for evaporation is supplied by exhaust heat recovery boilers and auxiliary boilers. The energy supplied during evaporation is recovered in the condensation. The MSF unit can be divided into three sections; a heat reject section, a heat recovery section, and a brine-heater section. A schematic diagram for the MSF system with brine circulation is shown in Figure 1. [16]. The recovery and reject sections are made up of a series of stages, each MSF stage has a flash chamber and a condenser; the vapor flashed off in the flash chamber is separated from the condenser by a demister which intercepts brine droplets entrained in the flashing vapor. A distillate trough under the condenser tubes collects the condensate. The sea water from supply pumps enters the MSF plant and flows through the condenser tubes of the reject section stages and gets heated by the heat released due to condensation of the flashing vapor. A part of this stream leaving the reject section is mixed with the sea water to preheat it; a part is added to the flash chamber of the last flash as make-up, and the remainder is rejected to the sea, the recycle brine drawn from the last flash enters the tubes of the recovery section and gradually gets heated by the heat released from the condensation of the flashing vapor in each stage and leaves the recovery section out of the first flash. It enters the brine-heater section on the tube side where it is heated further to the required top brine temperature (TBT) by condensing steam on the shell side. The heated brine then enters the flash chamber of the first stage which is maintained at an appropriate pressure where it flashes. The flashing brine flows from one stage to the next through an orifice which controls the brine level in each flashing chamber. Pressure is gradually decreased in the successive stages as flashing continues. A part of the concentrated brine from the flashing chamber of the last stage is discharged as blow-down and the remainder combined with the make-up flow serves as the recycled brine. The distillate flowing from stage to stage in the distillate tray is taken out as the product from the last stage and chemically treated to adjust the pH and hardness prior to sending it to the storage tanks. There are a number of process variables which need to be set for reasonable operation of an MSF plant. They are:

1. TBT from the brine heater. This directly affects the distillate production and the levels in each flash chamber. There is a maximum allowable value, depending upon the type of scale inhibitors added to the make-up feed.
2. Brine recycles flow. This directly affects the levels in each flash chamber and the steam consumption for a fixed TBT. The higher the flow rate, the lower the flashing efficiency with a reduction in the residence time in the stages and an increasing brine level in the stages.
3. Make-up flow. This makes up for the blow-down flow and the distillate product flow out of the plant. It affects the temperature of the recirculating brine and thus affects the flashing process.
4. Low pressure (LP) steam temperature leaving the spray system. This dictates the heat content of the steam.
5. Sea water feed flow. This governs the fluid velocities in the tubes of the reject section. It affects the heat transfer in the heat reject section.
6. Sea water feed temperature. This directly affects the heat transfer in the reject section. It also affects the temperature of the makeup and thus of the recirculating brine.
7. Brine heater condensate level. This ensures that the heat exchanger tubes are not submerged in condensed steam, since that will adversely affect the heat transfer.
8. Brine level in the last stage. This affects the level of brine in the preceding stages, and helps to avoid drainage of the system.
9. Distillate level in the last stage. This ensures that the **distillate does not overflow the distillate tray.**

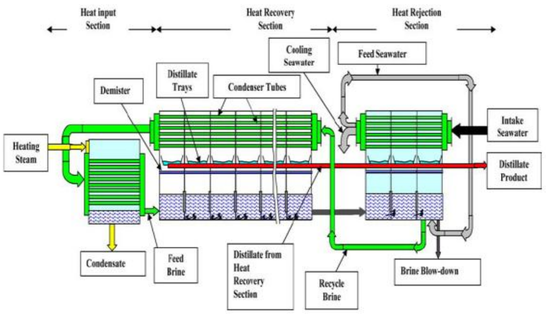

Figure 1. Multi stage flash desalination process [16]

3. Physical Model Description

The MSF process is a flash evaporation process at low pressure (vacuum), where the pressure decreases and the evaporation temperature in accordance decreases from the first to the last stage. From the modeling point of view, it is easier to describe a single flash stage if it is split up into four control volumes, which can be treated separately. The four control volumes are, flash chamber, vapor space, product tray, and tube bundle. Figure 2 shows the graphical representation of the four control volumes of stage. Each fluid stream communicating with the individual stage has four characterizing variables, flow rate, temperature, pressure, and salt concentration. The physical properties, enthalpy, density, and specific heat of the stream, are functions of these variables. The time derivatives included for the mass hold-up, concentration, temperature and specific enthalpy in each of the control volumes of the MSF stages represent the dynamic model. With these derivatives put to zero, the model represents steady-state conditions.

3.1. Mathematical representation of the stage

The MSF desalination stage can be divided into the following four control volumes (CV):

1. The flashing brine pool.
2. The distillate (product) tray.
3. The vapor space.
4. The condenser tubes.

These control volumes are shown in Figure 2. In each control volumes the mass flow rate, temperature, concentration and pressure are considered the fundamental independent variables that characterize the stream. In the present model, the lumped capacitance and uniform state approximations are assumed. Therefore, the state of the flow at CV exit is assumed the same as that for the mass hold-up in the CV. Thus yield;
$T_{b(i)} = T_{B(i)}$, $T_{pr(i)} = T_{PR(i)}$, $T_{wa(i)} = T_{WA(i)}$ and $X_{b(i)} = X_{B(i)}$

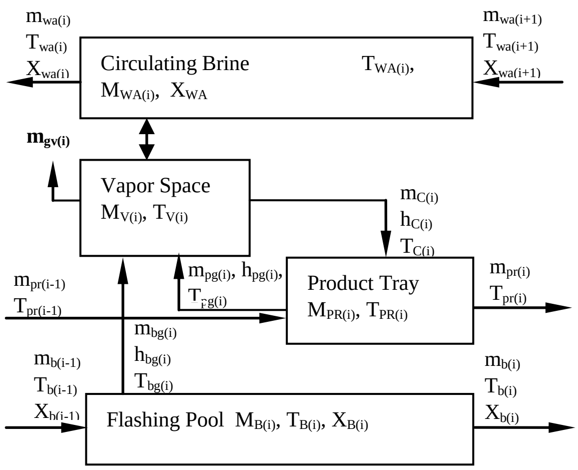

Figure 2. Block diagram of a repeated stage.

Also the following basic assumptions are carried out in the present work.

1. Salt is not present in the vapor.
2. Liquid is perfectly mixed on each unit.
3. The heat of mixing due to change in salinity is ignored.
4. Vapor is perfectly mixed on each unit.
5. The vapor is saturated.
6. The oscillations of stage brine level are negligible.

7. Initially at time t = 0, the system is at atmospheric conditions.

in addition to the above-mentioned assumptions, the present model has the following advantages:

1. The pre-heater heat transfer area and the surface area of each flashing chamber are considered in the objective function and the main brine heater transfer area is also considered.
2. The system is well insulated.
3. Dependence of heat capacity, boiling point elevation and latent heat of evaporation on temperature and concentration is considered by rigorous correlations.
4. Dependence of the overall heat transfer coefficient on brine velocity, temperature, and tube diameter is considered.
5. Non-equilibrium allowance is taken into account according to the correlation developed in [3].
6. Hydraulic correlations given in [4]. These equations describe the inter-stage flow rate of the flashing brine.
7. Stage geometric design (length, width and height) is considered.
8. Non-condensable effects are neglected.
9. Maximum number of stages N =21.

3.1.1. Stage Model

The mass conservation equation for the brine in the flashing pool is given by:

$$\frac{dM_{B(i)}}{dt} = m_{b(i-1)} - m_{b(i)} - m_{bg(i)} \qquad (1)$$

$$m_{b(i)} = \rho_{b(i)} A_{O(i)} v_{(i)} \qquad (2)$$

The balance of the dissolved solids reads

$$M_{B(i)} \frac{dX_{B(i)}}{dt} = m_{b(i-1)} X_{b(i-1)} - m_{b(i)} X_{b(i)} \qquad (3)$$

The energy balance for brine pool is given by

$$M_{B(i)} Cp_{b(i)} \frac{dT_{B(i)}}{dt} = m_{b(i)} Cp_{b(i-1)} T_{b(i-1)} - m_{b(i)} Cp_{b(i)} T_{b(i)} - m_{bg(i)} h_{bg(i)} \qquad (4)$$

The mass conservation equation for the product in the tray is

$$\frac{dM_{PR(i)}}{dt} = m_{pr(i-1)} + m_{c(i)} - m_{pr(i)} - m_{pg(i)} \qquad (5)$$

The energy balance for the product tray is

$$M_{PR(i)} Cp_{pr(i)} \frac{dT_{PR(i)}}{dt} = m_{pr(i-1)} Cp_{pr(i-1)} T_{pr(i-1)} - m_{pg(i)} h_{pg(i)} - m_{pr(i)} Cp_{pr(i)} T_{pr(i)} + m_{c(i)} h_{c(i)} \qquad (6)$$

The mass balance for the vapor space produces

$$\frac{dM_{V(i)}}{dt} = m_{bg(i)} + m_{pg(i)} - m_{c(i)} - m_{gv(i)} \qquad (7)$$

The energy balance for the vapor space is as follows

$$dM_{V(i)} Cp_{V(i)} \frac{dT_{V(i)}}{dt} = m_{bg(i)} Cp_{bg(i)} T_{bg(i)} + m_{pg(i)} Cp_p - U_{(i)} A_{c(i)} \Delta T_{(i)} \qquad (8)$$

Where $U_{(i)}$ is the heat transfer coefficient, $A_{C(i)}$ is the heat transfer area and $\Delta T_{(i)}$ is the log mean temperature difference (LMTD), given by

$$\Delta T_{(i)} = \frac{\left(T_{c(i)} - T_{wa(i)}\right) - \left(T_{c(i)} - T_{wa(i+1)}\right)}{Ln\left[\frac{\left(T_{c(i)} - T_{wa(i)}\right)}{\left(T_{c(i)} - T_{wa(i+1)}\right)}\right]} \qquad (9)$$

The mass balance for the condenser tubes can be written as

$$m_{wa(i)} = m_{wa(i+1)} \qquad (10)$$

The salt balance of circulating brine is given by

$$X_{wa(i)} = X_{wa(i+1)} \qquad (11)$$

It is assumed that mass of brine in the condenser tubes remains constant and there is no accumulation of salt in the condenser tubes. Thus,

$$\frac{dM_{WA(i)}}{dt} = 0 \quad \text{and} \quad M_{WA(i)} \frac{dX_{WA(i)}}{dt} = 0 \qquad (12)$$

The energy balance for the condenser tubes yields

$$M_{WA(i)} Cp_{ba(i)} \frac{dT_{WA(i)}}{dt} = m_{wa(i+1)} Cp_{ba(i+1)} T_{wa(i+1)} - m_{wa(i)} Cp_{ba(i)} T_{wa(i)} + U_{(i)} A_{c(i)} \Delta T_{(i)} \qquad (13)$$

The saturation temperature of the vapor above the flashing brine will be less than the brine temperature by the boiling point elevation (BPE), non-equilibrium allowance (NEA) and loss in saturation temperature due to other pressure losses ΔT_P,

$$T_{V(i)} = T_{b(i)} - BPE_{(i)} - NEA_{(i)} - \Delta T_{P(i)} \qquad (14)$$

3.1.2. Last stage Model

The brine mass conservation equation is

$$\frac{dM_{B(n)}}{dt} = m_{b(n-1)} + m_k - m_{wa(n)} - m_{bd} - m_{bg(n)} \qquad (15)$$

The balance of dissolved salt is

$$M_{B(n)} \frac{dX_{B(n)}}{dt} = m_{b(n-1)} X_{b(n-1)} + m_k X_k - m_{wa(n)} X_{w(n)} - m_{bd} X_{bd} \qquad (16)$$

The energy balance for the brine is,

$$M_{B(n)} Cp_{bd} \frac{dT_{B(n)}}{dt} = m_{b(n-1)} Cp_{b(n-1)} T_{b(n-1)} + m_k Cp_k T_k - m_{wa(n)} Cp_{wa(n)} T_{wa(n)} - Cp_{bd} m_{bd} T_{bd} - m_{bg(n)} h_{bg(n)} \quad (17)$$

The conservation equations for distillate tray vapor space and the condenser tube can be written in a similar manner as that for the repeated stage (i), Eqs. (5) to (14).

The formulated basic equations include some physical properties which are correlated with subsidiary equations as functions of these stage variables, it can be found in[17].

3.1.3. Modeling of the Brine Heater

The brine heater is a shell and tube type heat exchanger in which, heating steam condenses outside the tube surface, exchanging its latent heat with the brine. The brine flows through the tubes and consumes the energy supplied by the steam. A schematic of the brine heater is shown in Figure 3.

The brine heater (BH) has a steam flow, m_S coming in at temperature T_S, and the condensate, m_L going out through at temperature T_L. The incoming steam is considered to be saturated and at the temperature of condensate in the sump as in the real plant

The mass and energy balance equations are given by

$$M_{BH} Cp_{BH} \frac{dT_{BH}}{dt} = m_S (h_S - h_L) - m_{wa(1)} (Cp_{wa(0)} T_{wa(0)} - Cp_{wa(1)} T_{wa(1)}) \quad (18)$$

$$M_{BH} = \rho_{BH} V_{BH} \quad (19)$$

$$m_{wa(1)} = m_{wa(0)} \quad (20)$$

$$m_L = m_S \quad and \quad T_L = T_S \quad (21)$$

$$X_{wa(1)} = X_{wa(0)} \quad (22)$$

$$V_{BH} = A_{BH} LT_{BH} NT_{BH} \quad (23)$$

Where, (0) refers to the 0^{th} stage i.e. the brine heater (BH).

4. Solution Procedure

The resulting sets of governing equations are solved numerically by using Runge-Kutta method. A computer package based on Mat-lab with menu driven user interface, interactive graphic interface, long double precision, mouse support, and printer support is implemented, the main output windows are shown in appendix (A). Starting from the initial state, the simulation strategy involves the procedure carried out in the following steps:

1. The algebraic variables are determined from correlations and algebraic equations.
2. The right hade side (R.H.S) of all the ODE's is calculated by using the algebraic variables determined in step 1.
3. A numerical solution using Runge-Kutta method uses the R.H.S to calculate the new values of all the differential variables for the next simulation time till a certain convergence.
4. Increment time by Δt and repeat steps 1 to 5, till a steady state is approached

5. Model Validation

The validity of the present model was checked by comparing the steady state results with some of the previous results and the actual data for Kuwait, Benghazi and Zuitina MSF plants. The comparisons are shown in Tables (1) to (3). Table (1) shows the comparison between the present predictions and actual data of Kuwait for the top brine temperature (TBT), the recirculating brine temperature that enters the brine heater (TW(1)), the product flow rate (mpr), the product temperature (TPr), the blow-down temperature and the performance ratio, which is defined as the mass flow rate ratio of distillate product to the heating steam. Table 2 shows the comparison between the present prediction of the top brine temperature (TBT), recirculating brine temperature enters the brine heater (TW(1)), product flow rate (mpr), product temperature (TPr), blow-down temperature and performance ratio with the actual data Zuitina MSF plant. The comparison shows good agreement between the present predictions and the actual data. Therefore, the present model is considerably valid to accurately predict the performance characteristics of MSF desalination plant at both steady states and transient.

6. Case Study

In this case study, the transient performance characteristics have been predicted utilizing the design data of Zuitina MSF desalination plant. The plant is constructed with a cross-tube-type multi-stage flash (MSF) evaporator with recirculating brine, and multi-stage condensers with two sections. The plant is composed of a heat recovery section (18 stages) and a heat rejection section (3 stages). Some of the design data of the Zuitina plant is listed in Table 3.

Table 1. Comparison between the present predictions, and some pervious data

Operating Parameters		Kuwait MSF plant	Al-Shayji [19]	Present predictions	(%) Deviation
Input	No. of Stages	24	24	24	---
	m_f , (T/h)	9629.3	9629.3	9629.3	---
	T_f , (^oC)	32.22	32.22	32.22	---
	m_S, (T/h)	140.862	140.862	140.862	---
	T_S , (^oC)	100	100	100	---
	X_F , ppm	45,000	45,000	45,000	---
Output	TBT , (^oC)	90.56	89.1	90.672	0.12
	$T_W(1)$, (^oC)	83.20	82.22	82.429	0.93
	m_{pr} , (T/h)	1127.7	1159.8	1121.5	0.55
	T_{Pr} , (^oC)	38.60	36.54	39.047	1.15
	T_{bd} , (^oC)	40.5	38.44	39.521	2.42
	PR	8.005	7.76	7.961	0.48

Table 2. Comparison between the present predictions and the data from Zuitina MSF plant

Operating Parameters		Zuitina MSF plant	Present predictions	(%) Deviation
Input	No. of Stages	21	21	---
	mf , (T/h)	2800	2800	---
	Tf, , (^oC)	28	28	---
	mS , (T/h)	52	52	---
	TS , (^oC)	124	124	---
	XF , ppm	35,000	35,000	---
Output	TBT , (^oC)	118	117.8612	0.12
	TW(1) , (^oC)	109.3	109.4263	0.11
	mpr , (T/h)	416.7	413.6298	0.74
	TPr , (^oC)	37	39.3282	5.9
	Tb(N) , (^oC)	38.2	40.3367	5.6
	PR	8.0128	7.9544	0.73

Table 3. The condenser tube bundle specifications

Parameter	Recovery section	Rejection section	Brine heater
Tube material	CuNi10Fe	Titanium	CuNi30Fe
No. of tubes per stage	1313	1410	1302
Tube length (m)	9	9.4	13.09
Outside diameter (mm)	24	19	24
Wall thickness (mm)	0.9	0.5	1
Heat transfer area (m^2)	891	791	1274
Fouling factor ($m^2.K/W$)	0.00009	0.000178	0.000178

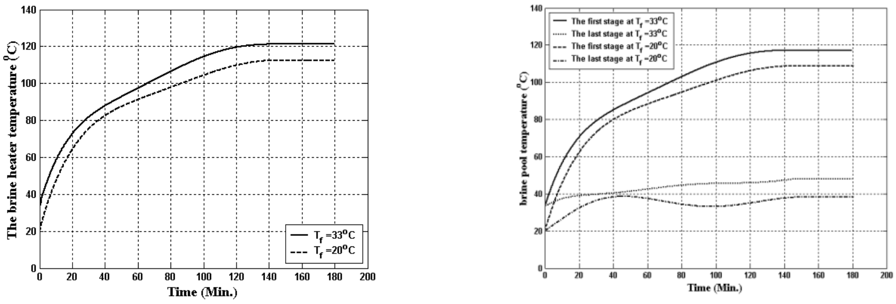

(a) At brine heater outlet (b) At the outlet of the first and the last stages

Figure 8. The time dependent flashing temperature at different seawater inlet temperatures

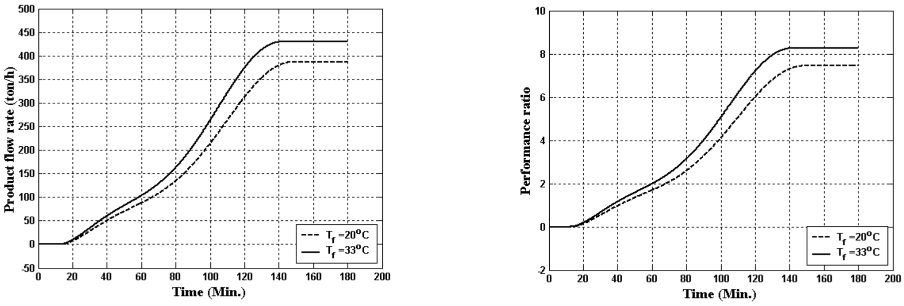

(a) Product flow rate (b) Performance ratio

Figure 9. Effect of seawater inlet temperature on product flow rate and performance ratio

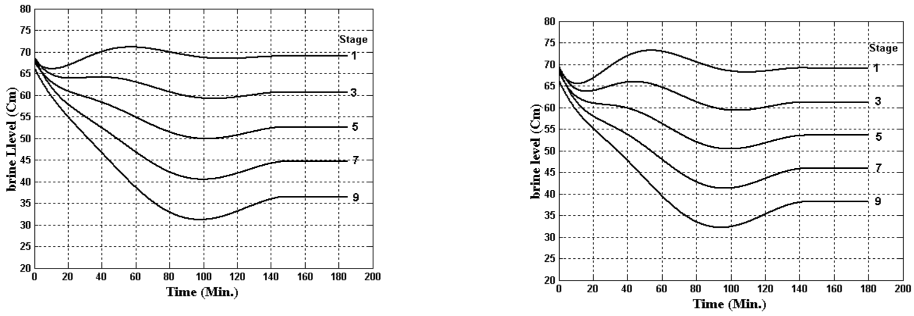

(a) At T_f =20 °C (b) At T_f =33 °C

Figure 10. Brine levels at start up period for Zuitina plant at two seawater inlet temperatures

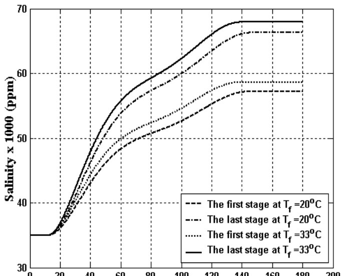

Figure 11. Stage wise salinity at two different seawater inlet temperatures

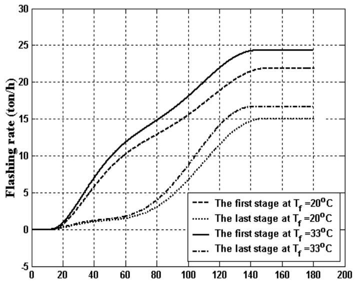

Figure 12. Stage wise flash rate at two different seawater inlet temperatures

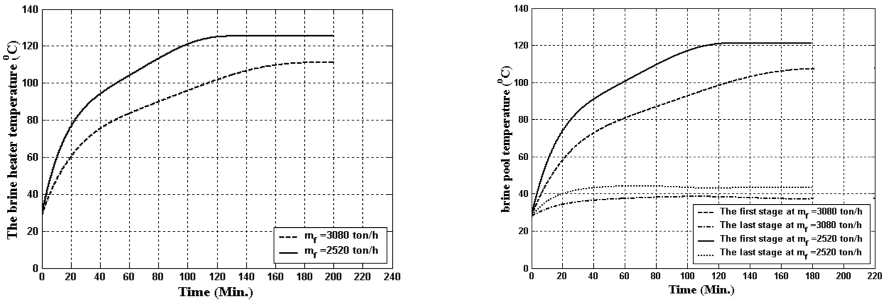

(a) Brine heater outlet temperature (b) Brine pool temperature

Figure 13. Brine temperatures at different seawater inlet flow rate

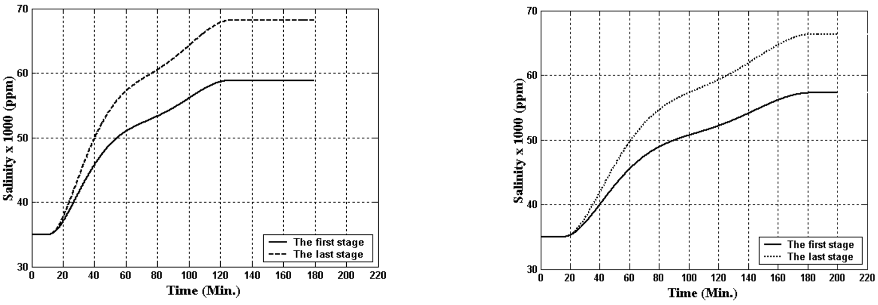

(a) m_f=2520 ton/h (-10% of design point) (b) m_f =3080 ton/h (+10% of design point)

Figure 14. Stage wise salinity at two different seawater inlet flow rate

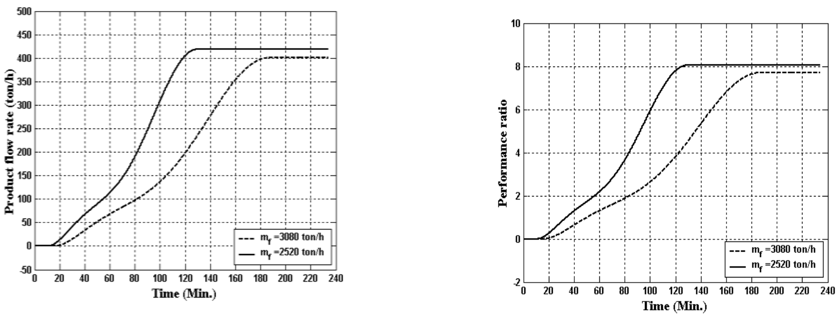

Figure 15. Effect of seawater flow rate on the product flow rate and performance ratio (±10% of design point)

i. Effect of the Heating Steam Temperature

One of the most important parameter that affects the MSF desalination process is the temperature of heating steam. The top brine temperature is dependant on the heating steam temperature which affects the overall plant performance characteristics as shown in Figure 16. The plant performance enhances with the increase in the heating steam temperature. This is due to the fact that as heating steam temperature increases the top brine temperature increases which enhances the flashing rate and product flow rate and in accordance enhances the plant performance ratio. An increase in the flashing rate results in the decrease of the brine levels in the first stage and subsequently to the other stages (as shown in Figure 17). Unfortunately, the extra increase in the heating steam temperature may increase the scales due to the increase in both salinity and the overall temperature level in the plant. Therefore, the heating steam temperature is limited to about 130 ^{o}C in most of the commercial MSF plant

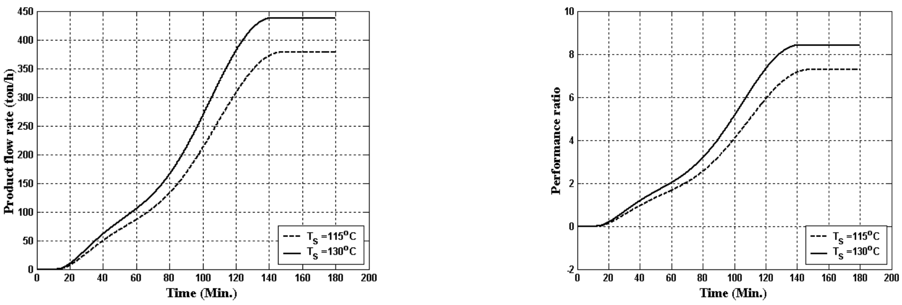

(a) Product flow rate (b) Performance ratio

Figure 16. The effect of heating steam temperature on transient product flow and performance ratio

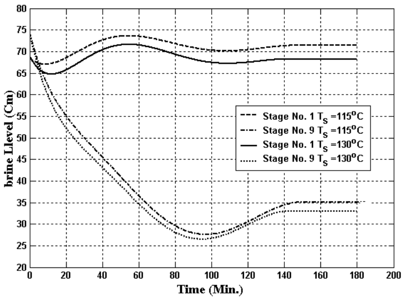

Figure 17. Brine level at two different heating steam temperatures

7. Conclusion

This work has presented a dynamic simulator for the analysis of MSF desalination plants using a dynamic analysis. The developed model is based on the basic equations of mass, momentum and energy. The proposed was able to investigate the affect of some key parameters such as seawater concentration and other thermal parameters that may affect the general performance of the MSF plant during transient as well as steady state operation condition. The proposed model was validated by using data from previous theoretical studies as well as actual data obtained from an operating MSF plant. The validation results showed good agreement with the predicted and the real case measured values. Based on data derived from a number of selected runs, the following conclusions may be drawn:

1. The seawater inlet flow rate (mf) had a very strong effect on the system performance, where its decrease results in increasing the system temperature and the flashing rate and subsequently the performance ratio. This is the opposite effect to increasing the seawater inlet flow rate.
2. An increase in the heating steam temperature (T_S) results in an increase of the system temperature, which improves the flashing efficiency as well as the net product flow rate. Also, this results in a decrease of the brine level that might result in vapor leaking across the stages. This is the opposite effect to decreasing the heating steam temperature.
3. Sea water temperature (T_f) has a considerable affect on the product of the plant as well as the performance ratio, and it has a slight effect on the top brine temperature and brine levels.

References

[1] Mazzotti, M., Rosso, M., Beltramini, A. and Morbidelli, M., “Dynamic modeling of multistage flash desalination plants” Desalination, Vol. 127, No. 3, 2000, 207-218.

[2] El-Dessouky,H.T. Shaban H. I. and Al-Ramadan, H. Desalination, Vol. 103,1995, 271-287..

[3] El-Dessouky,H.T. and Bingulac, S. Desalinat- ion, Vol. 107, 1996, 171-193.

[4] Aly, N.H., El-Fiqi, A.K., Desalination, Vol. 158, 2003, 127-142.

[5] Glueck, A.R., and Bradshaw, R.W., Proc. 3rd Int. Symp. on Fresh Water from the Sea, Vol. 1, 1970, 95–108.

[6] Yokoyama, K., Ikenaga, Y., Inooe, S. and Yamamoto, T., Desalination, Vol. 22, 1977, 395-401.

[7] Maniar, V. M., and Deshpande, P.B., J. proct. Cont., Vol. 6, No. 1, 1996, 49-55.

[8] Thomas, P.J., Bhattacharyya, S., Patra, A. and Rao, G.P., Comput. Chem. Engng., Vol. 22, No. 10, 1998, 1515-1521.

[9] Rimawi, M., Euouney, H., and Aly, G. Desalination, Vol. 74, 1998, 327–338.

[10] Tarifa, E.E., Scenna, N.J., Desalination, Vol. 138, 2001, 349–364.

[11] G.P. Rao, Desalination, Vol. 92, 1993, 103.

[12] E. Ali, Desalination, Vol. 143, 2002, 73-91.

[13] Aly, N.H., Marwan, M.A., Desalination, Vol. 101, 1995, 287-293.

[14] Alatiqia, I., Ettouneya, H., El-Dessoukya, H., Al-Hajrib, K., Desalination, Vol. 160, 2004, 233–251.

[15] Gambier, A., Badreddin, E., Desalination, Vol. 166, 2004, 191–204.

[16] El-Dessouky, H.T., Ettouney, H.M. Al-Roumi, Y., Chem. Eng., Vol. l73, 1999, 173-190.

[17] Helal, A.M., Medani, M.S. and Soliman, M.A., Comput. Chem. Eng., Vol. 10, No. 4, 1986, 27–342.

[18] Al-Shayji, K.A, “Modelling, Simulation, and Optimization of Large-Scale Commercial Desalination Plants.” Dissertation, Virginia Polytechnic Institute and State University, USA, 1998..

[19] Shivayanamath, S., Tewari, P.K., Desalination, Vol. 155, 2003, 277-286.

Appendix

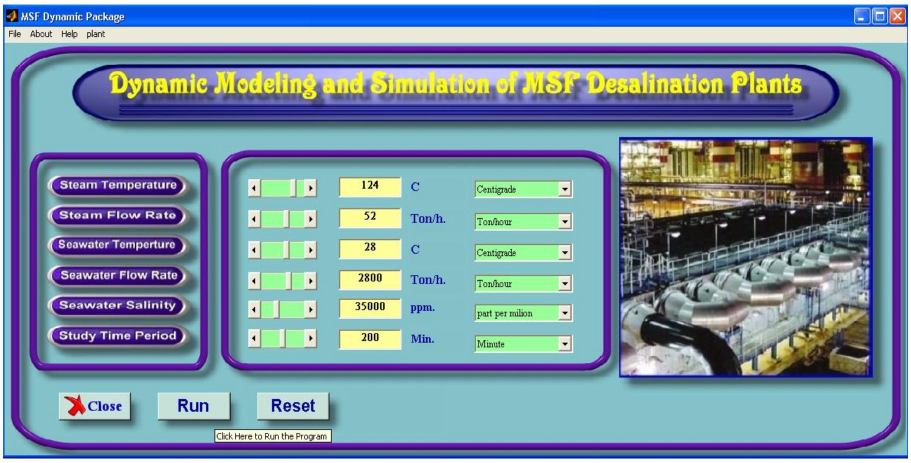

The Mat-lab graphical user interface for the interactive simulation

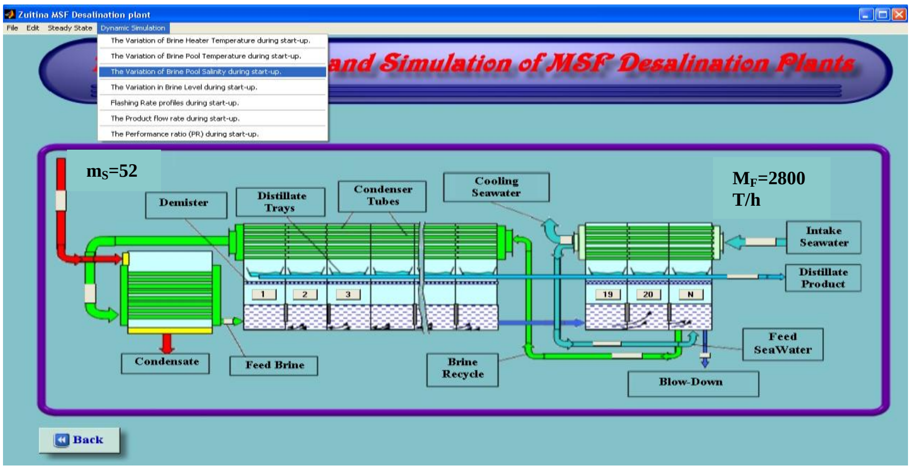

The main out-put screen

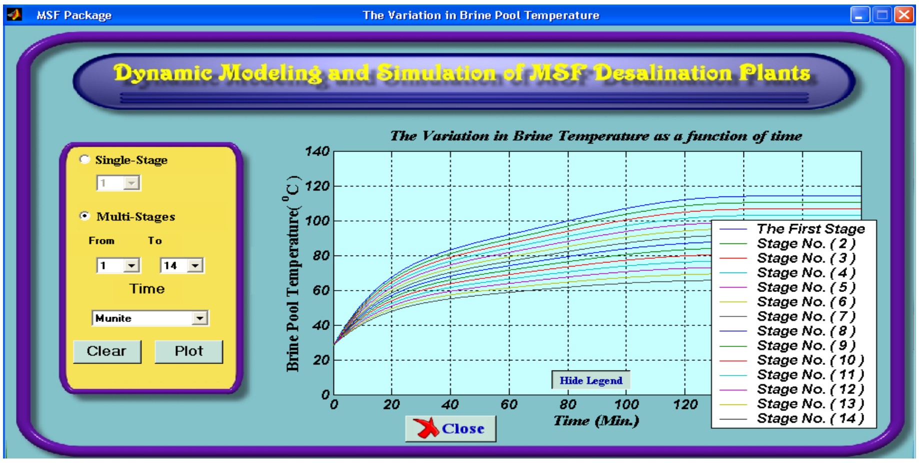

JJMIE

Volume 4, Number 3,June, 2010
ISSN 1995-6665
Pages 404 - 411

Jordan Journal of Mechanical and Industrial Engineering

An Automatic Method for Creating the Profile of Supersonic Convergent-Divergent Nozzle

M. Al-Ajlouni*

Department of Mechanical Engineering,Faculty of Engineering, Mu'tah University, Mu'tah, Al-Karak 61710 Jordan

Abstract:

The supersonic convergent-divergent nozzles have many applications. An advanced design method must be used when the conditions are critical and wave-free stream must be reached. The characteristic method is a general technique in which the design of a nozzle can be achieved. Unfortunately, this technique can be performed only through a lengthy graphical procedure. The aim of this paper is to create an automatic way to perform the nozzle profile using the above method. Although, there are a variety of CFD & FE packages that deal with nozzle design, they all require the profile of the nozzle to be started with. This research develops a new approach that helps the machine designer to create this profile. Through this work, two computational stages have been used and both with the aid of the computer. Firstly, a well-known calculation and graphical packages have been used to create the unit model matrix for each Mach number. Then, in the second stage, programming with visual basic has been used to create the profile of the nozzle automatically by multiplying the unit model matrix by the proper scale factor that is calculated according to the working requirements. User friendly software has been written for this purpose. The functionality of the method is validated by solving problems with known solutions and this approach presented logical results. This work is limited for Mach number up to 2.5 only, constant specific heat and two dimensional flows.

Keywords**:** Convergent-divergent supersonic nozzle; Characteristic method; Mach-wave; Prandtl-Meyer angle; maximum expansion angle and algorithm.

Nomenclature

A	Cross sectional area (mm^2)
D	Diameter (mm)
H	Height (mm)
L	Length of the nozzle (mm)
M	Mach number
m	Mass flow rate (kg/s)
N	Speed index = 2θ
P	Pressure (N/m^2)
PDEs	Partial differential equations
R	Gas constant = 8.31434 (kJ/kmol . K)
SCDN	Supersonic convergent divergent nozzle
T	Temperature (ºK)
u, V	The Velocity (m/s)
γ	The Ratio of Specific Heats
μ	Mach angle (Degree)
θ	Prandtl-Meyer angle (Degree)
θ_a	Flow inclination(Degree)
ξ	Characteristic Subscripts
i	Inlet
e	Exit
t	Throat

1. Introduction

Supersonic nozzle has many applications in industry. These include, and not limited to, the areas of gas turbines and turbo machinery [1], separation systems [2 and 3], geo-environmental techniques [4], air conditioning [5] and many others. It is used in many ways like: De Laval nozzle in the high-speed steam turbine, in the jet propulsion units, in rocket motors, in the drive of air turbines, in gas turbines, in the thermal ejectors and in the supersonic wind tunnels.

The basic theory (one and two dimensional analysis) of the design of the super sonic convergent divergent nozzle(SDCN) can be found in many references like those at the end of this paper. More advanced methods must be used when the conditions are critical and wave free stream must be reached. The characteristic method is a general technique in which the design of nozzles can be achieved [6]. Unfortunately, this technique can be performed only through a lengthy graphical procedure. Step-by-step graphical procedure must be accurately followed. Although, there is a wide range of CFD and FE packages that deals with nozzle design each of these needs the profile of the nozzle to start with [7,8]. Dimarogonas [7]

* Corresponding author. ajlouni@mutah.edu.jo.

concluded that any attempt to utilize computer methods for machine design or analysis should start with the description of the geometry of the machine or a machine part in a complete and unambiguous manner by a set of computer-stored information that can be further utilized for analysis or design. The aim of this paper is to create an automatic way to perform the profile of the SCDN . To generate such a profile the method of characteristic can be used and the graphical procedure is performed automatically by aid of the computer. Unfortunately, this graphical procedure cannot be programmed directly and a primary stage of data preparing is needed. Microsoft Excel and AutoCAD have been chosen to create the database required. A Visual Basic code has been developed in order to treat with this database and then to determine the required profile.

On other words, the objective of this research is to develop a new method that performs the creation of the profile of the SCDN automatically. A user friendly software package helps the machine designer to get this profile that produces uniform supersonic flow at the end of the nozzle. Input parameters for the software will include for example: air properties, mass flow rate, and the Mach number required at exit. The output of the software will include a plot of the nozzle profile, a table that contains the coordinates of this profile in both x and y directions and a full report in win-word or notepad format. This paper is structured as in the following: Section two covers the theoretical background of the different approaches of modelling. Section three outlines the methodology of the research and the developments of the software. Section four shows the results and discusses them. Section five provides the summery and conclusions of the research.

2. Theoretical Background

The design of the supersonic convergent–divergent nozzle (SCDN) has different approaches with different levels of simplifications. The following sections will cover these levels.

2.1 One-Dimensional Flow :

The concept of ‘one-dimensional’ flow in any form of conduit is that all relevant quantities (velocity, pressure, density and so on) are constant over any cross-section of that conduit. Thus the flow can be described in terms of only one coordinate and time. The flow of a real fluid is never strictly one-dimensional because of the presence of boundary layers, but the assumption provides satisfactory solutions of many problems in which the boundary layer is not very thick and there are no abrupt changes of cross-section. Many references in the literature [e.g. 9] use the one-dimensional idealization to examine instances of flow in which the effects of compressibility are of particular importance. The whole analysis will not be repeated here and only some important points will be drawn. The main relation between the area and velocity is

$$dA/A = du/u\ (M^2-1) \qquad (1)$$

Several important conclusions may be drawn from equation (1). For subsonic velocities (M<1), dA and du must be opposite in sign. That is, an increase of cross-sectional area causes a reduction of velocity and vice versa. For supersonic velocities, however, M^2-1 is positive and so dA and du are of the same sign. When M=1 or du=0, dA must be zero and A must be a minimum.

The relation between throat area, and choked mass flow rate for air, with constant specific heat is

$$m = \rho AV = 0.686\, A_t\ P_i / (R\, T_i)^{1/2} \qquad (2)$$

This equation shows that no matter how much the exit pressure is reduced, or how the shape of the duct may change upstream or downstream of the minimum cross-section, this maximum flow rate cannot be exceeded. The nozzle will be either subsonic throughout, over-expanding or under-expanding depending on the exit pressure. (For more details see[10 and 11].

2.2 Multidimensional Flow:

The computation of exact or nearly exact flows of a frictionless incompressible fluid around general two-dimensional boundaries offers problems of some mathematical difficulty [12, 13, 14 and 6]. The additional condition that the density of the fluid may vary will complicate the problem under certain conditions; however, in those cases where the velocities in the flow field are everywhere greater than the local speed of sound, a fundamental simplification occurs. James [15], presented the nonlinear partial deferential equations (PDEs) of motions (continuity and momentum) for multidimensional flow. He showed that direct integration of these equations over the entire flow field is difficult unless further assumptions are made about the nature of the flow. The mathematics associated with a system of nonlinear PDEs is extremely complex; in many cases, solutions are not possible. To reduce the equations to more workable form, one shall place certain restrictions on the flow and thereby linearize the PDEs. In certain cases, as the case of the SCDN, however, approximate solutions obtained by linearization are not adequate, but greater accuracy is necessary. Instead of dropping terms, it is often desirable to consider the complete nonlinear equation. Fortunately, as James maintained, the very nature of supersonic flow allows a numerical method of solution of the complete differential equation for problems in two-dimensional flow, axisymmetric flow, and one dimensional unsteady flow. This process is known to mathematicians as the “method of characteristics”.

2.3 Method of Characteristics:

The method of characteristic is a general technique in which partial differential equations of pressure transients are converted into particular simultaneous total differential equations which, after being expressed in finite-difference form, can be solved by computer. The fundamental idea of the method of characteristics is to replace the infinite number of waves by a finite number which can then be treated separately. In the areas between waves, the velocity magnitude and direction are considered constant. Therefore it is necessary to replace the actual boundaries of the flow by approximate boundaries with a finite number of disturbances. In other words, a curved boundary is replaced by a number of straight-line segments, with a definite angle between them [6]. The process of computing the flow change from region to another is thus reduced to the purely mechanical process. This approach is explained in details in the work of [3 and 6] and will not be repeated here and only some important relations will be given.

A characteristic is a line that exists only in supersonic flows. Characteristics should not be confused with finite strength waves, such as shock waves [13]. The ξ characteristic is inclined to the local streamline by the angle μ, which is the Mach angle,

$$\mu = \sin^{-1} (1/M) \tag{3}$$

The difference between a shock wave and a Mach wave should be kept in mind. A Mach wave represents a surface across which some derivative of the flow variables (such as the thermodynamic properties of the fluid and the flow velocity) may be discontinuous while the variables themselves are continuous. A shock wave represents a surface across which the thermodynamic properties and flow velocity are essentially discontinuous. Thus, the characteristic curves, or Mach lines, are patching lines for continuous flows, whereas shock waves are patching lines for discontinuous flows. The use of the isentropic relationships then permits an evaluation of the change of pressure and temperature taking place through the expansion. At a concave corner in supersonic flow, an isentropic expansion takes place [15]. This flow consists of a large number of expansion Mach waves; across each wave the changes in flow properties are infinitesimally small. The resultant flow is analyzed by using the equations of continuity, momentum, and energy for a perfect gas with constant specific heats. The sum of the angles of the concave wall ($\Sigma\theta_a$) that called the Prandtl-Meyer angle expansion (θ) is a function of the Mach number as given by

$$\theta = \sqrt{\frac{y+1}{y-1}} \tan^{-1} \sqrt{\frac{y-1}{y+1}(m^2-1)} - \tan^{-1}\sqrt{m^2-1} \tag{4}$$

Equation (4) above has been derived in details by James [15]. The result of this analysis has been presented in tabular form, showing the change in Mach number occurring for a given flow turning angle. The use of the isentropic relationships then permits an evaluation of the change of pressure, temperature, and other thermodynamics taking place through the expansion. The maximum permissible expansion angle (θ_{max}) for any nozzle design, as Puckett [6] maintained, is exactly one half of the Prandtl-Meyer angle expansion (θ).

When a Prandtl-Meyer expansion flow impinges on a plane wall, sufficient waves must be generated to maintain the wall boundary condition; that is, at the wall surface, the flow must be parallel to the wall. To cancel the incident wave, the wall must turn through an angle of θ_a at the point of impingement of the incident wave. The resultant wave interactions present complexities that render an exact analysis of the flow which is extremely difficult; however, the general nature of the flow can be recognized. There is no reflected wave, since the boundary condition at the wall is satisfied without it; the incident wave is effectively canceled. One more use of this idea is the nature of effect of the centerline. Since, from symmetry there can be no flow across the center streamline; this streamline can be replaced by a plane wall. This fact will allow the designer to reduce the calculation as only one side of the nozzle will be considered.

2.4 The Design of the Supersonic Convergent-Divergent Nozzle (SCDN):

The method of characteristics was first applied to supersonic flows by Prandtl and Busemann in 1929 and has been much used since. Puckett, in his significant paper in 1946 [6], used this method with supersonic nozzle design and made the technique more accessible to engineers.

In supersonic nozzle design the conventional two-dimensional nozzle is usually considered to consist of several regions as shown in figure (1) These are :--

(i) the contraction, in which the flow is entirely subsonic,
(ii) the throat region, in which the flow accelerates from a high subsonic to a low supersonic speed,
(iii) an initial expansion region, where the slope of the contour increases up to its maximum value,
(iv) the straightening or 'Buseman~' region in which the cross sectional area increases but the wall slope decreases to zero, and
(v) the test section, where the flow is uniform and parallel to the axis.

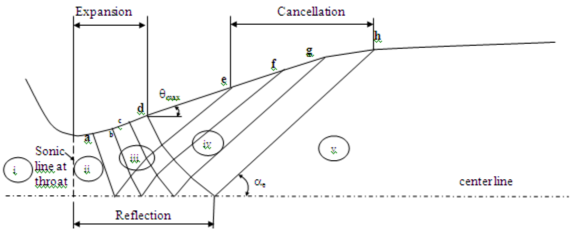

Figure 1. Supersonic nozzle design by the method of characteristics

The equations of motion assume such a form that they may be solved graphically, in a step-by-step process. A two-dimensional flow field in which the velocity is everywhere supersonic can always be represented approximately by a number of small adjacent quadrilateral flow fields in each of which the velocity and pressure are constant. These quadrilaterals must be separated by lines representing waves in the flow; changes in velocity and pressure through any wave can be computed. By increasing the number of small areas into which the complete flow is divided, the accuracy of this approximate solution may be increased without limit. Because of symmetry, the centerline of the nozzle is treated as a solid boundary, and only one half of the nozzle need to be considered for calculation. The gas is to be accelerated to uniform and parallel supersonic flow at the desired Mach number.

The design of the convergent part (region i) is less critical than the divergent part as it contains a subsonic flow [16]. The contraction, from supply section to the throat, must be such a shape that the air is uniformly accelerated and to ensure that the pressure decreases monotonically without any adverse pressure gradient or accrues of separation. This can be achieved by changing the curve smoothly. The length of this section has a little effect on the boundary layer thickness at the throat. The wall curve of this section has been considered as part of a circle with a diameter equal to the throat height started from the throat area. The length of this section can be any value between 0.5 and 1 of the height of the throat. This value depends on the application and whether long or short nozzle is required. The smallest value in the range will be used, in this work, for the short nozzles and the largest value will be used for the long nozzles.

The divergent part (regions iii-iv) of the nozzle is designed according to the characteristic method using the maximum expansion angle. Saad [17], showed that the gas accelerates beyond the throat (region ii) until the desired Mach number is reached, and the cross-sectional area of the nozzle must increase downstream of the throat. The nozzle contour must then decrease more and more gradually the closer it comes to final area, so that there will be one-dimensional parallel flow at exit (region v). The first portion of the divergent part (region iii) is build in such a way that the contour of the nozzle first turns through a positive angle in the region from point **a** to point **d**, and then tern back through the same angle from **e** to **h**. Point **d** thus corresponds to the maximum inclination of the wall (θ_{max}). The contour of the nozzle from **a** to **d** is divided into a number of straight segments **ab**, **bc** and **cd**. The expansion of the gas flowing from section **a** to **d** is treated as a series of expansion across the waves generated at **a**, **b**, **c**, and **d**. When those waves reach the centerline, they are reflected, and these reflected waves then intersect other incident waves until they finally reach the nozzle contour at point **e**, **f**, **g**, and **h**. In the case of the intersection of two waves of opposite families each one will deflect dθ on its side. Practically, this has been achieved by constructing this portion (region iii) in such a way that the area increases by a finite number of straight line each one millimeter in length and inclined by 2 degree more than the previous one. This process will be continued until the angle of maximum expansion (θ_{max}) is reached. The more points selected in the region between a and d, the larger is the number of the waves that are considered in the analysis and the more effective is the nozzle in providing the desired flow. The nozzle contour a-b-c-d turns the flow through the angle θ_{max}. Its length can be made minimum provided no flow-separation or boundary-layer effects are generated. Any expansion waves that are generated in this portion of the nozzle must be canceled. The nozzle at each impingement point is of such contour that any reflected waves are canceled, and the resulting flow is then parallel and wave-free. The maximum turning angle of the nozzle counter angle θ_{max} occurs at the end of expansion (at point **d**). At this point the wall will start inclining (region iv) downward by 2 degree at the end of each of reflected Mach wave until it becomes parallel to the axis again as explained previously. Whilst doing this step-by-step graphical procedure, the rules of intersection of two waves and intersection of wave and wall have been used in the way explained above and details can be found in the literatures.

This method was graphical and approximate so that it was subject to protractor errors, and afforded no means of determining the length of the nozzle in advance.

The nozzle design method described above can be used to calculate the 'potential outline'. However, in real fluids, many other factors can affect the design. One of those factors is that it is necessary to allow the growth of the boundary layer along the walls of the tunnel [6]. This is done by displacing the potential outline away from the tunnel centre line, the correction being applied from knowing the displacement thickness of the boundary layers. Another factor is the shape of throat region. There are two categories for this nozzle according to the sonic line [18-22]. If the sonic line is a straight line, as in this work, the wall at the throat generates centered and divergent waves. The second category has a curved sonic line. In this case, the flow inside the nozzle has no centered Mach lines. This type of nozzle is named Plug nozzle with curved sonic line. One more factor is to include the high temperature effect. This will modify the final shape of the profile as shown by many references [e.g. 21]. The last factor to be mentioned here is the case of the nozzle of the minimum length [21]. This nozzle is characterized by the absence of an initial expansion region. For this case, a series of expansion wave take place at the sharp corner that is called Prandtl-Meyer expansion fan.

3. The Methodology Of The Research

The nozzle design method described above can be achieved in a mechanical manner by using the computer as an aid technique. The problem is solved by developing a software package to perform it. Figure 2 presents the main window of the software package and Figure 3 presents the **Calculations and Results** window and the details can be found in the Appendix.

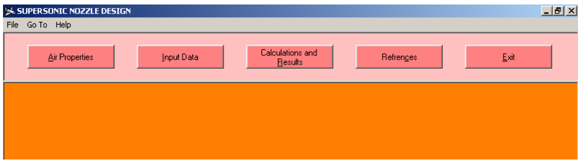

Figure 2. The main window of the packge

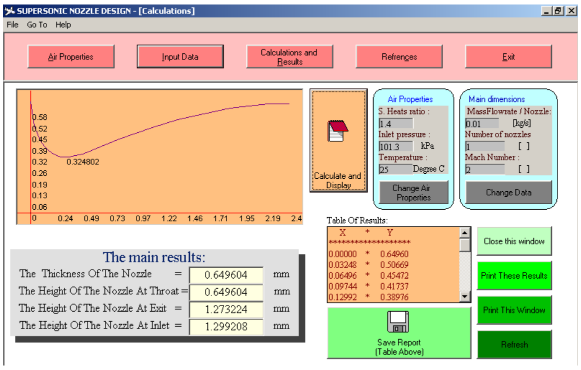

Figure 3. The calculations and results window

Having covered the theoretical background of the design and the features of the software it is appropriate at this point to describe the logic used in this work. The research consists of two stages. The first stage deals with the preparation of databases required whilst the second stage deals with writing the code of the design package that use these data. At the first stage, many graphs have been drawn manually using a standard drafting package, namely, AutoCAD with the aid of Microsoft Excel as a calculation tool. At this stage, graphs for several Mach numbers at a unit throat height have been drawn. These graphs represent the unit model of the nozzles for each value of Mach number. Figure 4 shows the unit models for nine different values of Mach numbers ranging from 1 to

2.5. Each unit model represents a nozzle that gives a specific Mach number with a unit height.

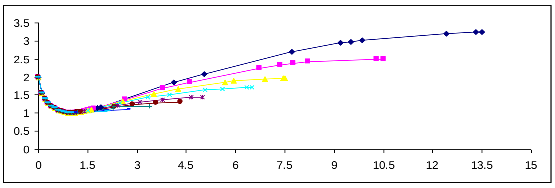

Figure 4. The unit models for nine different values of Mach numbers ranging from 1 to 2.5.

The nozzle may be drawn symmetrically about the center line, or, as is done here, the center line is replaced by a solid wall; the flow solution must be the same in either case[6]. The method of characteristic, described above, has been used step-by-step graphically to construct these models. The x-y coordinates of these graphs have been stored in the unit matrices in the database and then exported into the VB code. At the second stage, a Visual Basic code has been developed to receive the operating conditions from the user and then scaling the unit model to match these conditions.

The main inputs to be entered to the program are the mass flow rate and the required Mach number. The mass flow rate is the main factor to determine the size of the nozzle (i.e. the throat height). One of the menus of the software prompts the user to enter the value of the total mass flow rate required by the application and allow the user to divide this value by the number of nozzles if conditions suggest that. Since the size of the nozzle should not exceed some practicable value, it is suggested here to change the number of the nozzles in order to decrease the flow rate per nozzle and, sequentially, decrease its size. On the other hand, the required Mach number at the exit is the main factor to define the profile of the nozzle and the area ratios. Fortunately, this profile is depending on the geometry only and can be scaled to any size or revised by changing x and y in the same ratio. This is the idea behind extracting infinite number of nozzles from the few unit models explained above. This can be done by finding the ratio between the required throat area and the throat area of the appropriate unit model. This ratio is the scale factor that converts the unit model into the profile of the required nozzle.

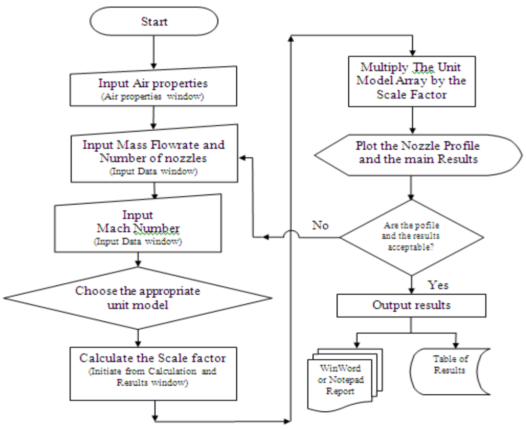

Figure 5. Presents the flowchart of the main program.

The following is a pseudo code presentation of the algorithm of the main program:

Algorithm:

Step 1: Choose the working fluid and provide its properties.

Step 2: Enter the total mass flow rate and the number of nozzles.

Step 3: Enter the required Mach number at the nozzle exit.

Step 4: Initialize the calculation and evaluate the scale factor by comparing the area required by the mass flow rate and the area of the unit model.

Step 5: Choose the appropriate unit model among the available database according to the required Mach number at the nozzle exit.

Step 6: Multiply the array of the unit model by the scale factor and this will create the final array.

Step 7: Plot the x-y profile of nozzle from the final array.

Step 8: Change input data if required.

Step 9: Send the final array into the list box.

Step 10: Send the final array into a file if a soft copy is required.

Step 11: Send the whole screen into a printer if a hard copy is required.

Step 12: Terminate the session.

4. Results and Discussion

In this section some examples of how to use the program and few study cases have been presented. Figure 6 presents an example of how to use the program. This figure has been extracted from the program for the same Mach number (2.3688) and for five different values of flow rate. The figure shows the similarity of the five nozzles and the only difference is the size that changes by the scale factor.

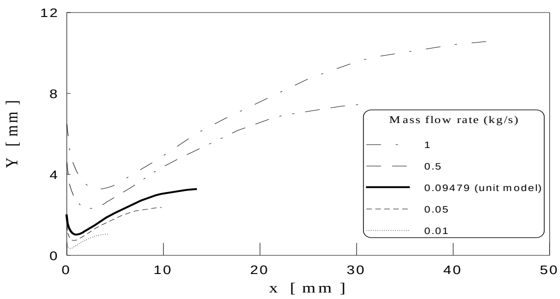

Figure 6. Comparison of a nozzle profile for five different values of flow rate and the same value of Exit Mach No. of 2.3688.

The functionality of the software has been validated by using it to solve many problems with known solutions. The software displayed logical results (study cases are shown in figures 7-9). Figures 7 and 8 show a very high degree of agreement between the manual methods [3,6] and computerized method of this work.

The diversity shown in figure 9 between the package results and the result of Puckett [6] is due to the approximations used in the latter work, and as expected the nozzle become longer. The approximation was necessary before the use of computer; however, the new results look more accurate.

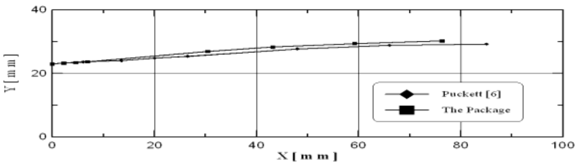

Figure 7. Case1: Comparison of a nozzle profile of Exit Mach No. of 1.64 between the values extracted from the Package and from Fig. 8 of [6].

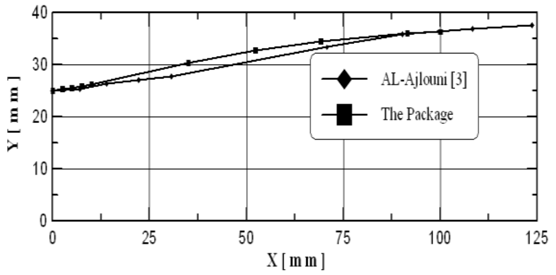

Figure 8. Case2: Comparison of a nozzle profile of Exit Mach No. of 1.77 between the values extracted from the Package and from Figure (7.2) of [3].

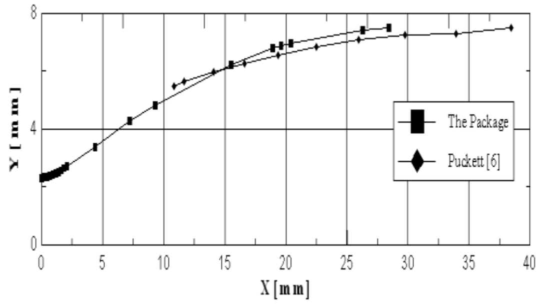

Figure 9. Case3: Comparison of a nozzle profile of Exit Mach No. of 2.42 between the values extracted from the Package and Table 2 of [6].

5. Conclusions

Supersonic convergent-divergent nozzles (SCDN) have many applications. They are usually subjected to complex flow pattern. Different degrees of simplification have been studied. Computer is a must to achieve high accuracy and large calculation needed with modern high speed applications. Hence, a computerized approximation approach might be a better method to tackle such a problem. Characteristic method is the most appropriate method to be used with (SCDN) design. Programming of this method directly is impractical as it uses a step-by-step graphical procedure. This problem has been overcome by using the unit models as a database for the developed package. The unit models have been built by using the method of characteristic for a representative number of nozzles that cover the required range of Mach numbers. These models have been established as the advocate database for the software package under development.

This research presents the development of a software package that can be considered as a tool for designing a (SCDN). The software is very user friendly and provides a wide range of options such as filing, plotting, and reporting. The profile of the nozzle in both graphical and tabulated form is the main output. The developed software includes also an error tracking system. The functionality of the software has been validated by using it to solve many problems with known solutions. The software displayed logical results

It shows that the developed software is a very useful tool for the designer in producing an accurate and immediate solution for very complicated cases. Any way, this is not the final version of the software and many other facilities could be added. For example, more general conditions may be considered. The future version of this software may include extension for higher range of Mach number, calculation of the mass flow rate, boundary layer correction, High temperature compensation, Minimum length nozzle, other types of the nozzle cross section, and a flexible link with other CAD packages.

Encouraging results are obtained so far. However, more future research must be made to develop a more sophisticated and flexible version of the package

Acknowledgments

The main part of this work has been perfumed whilst the author was spending his sabbatical leave at Philadelphia University/ Jordan. He acknowledges their help, encouragement, and time allocated. The author also, acknowledges Mutah University for their financial support.

References

[1] S. Gilham, P.C. Ivey, J.M. Owen, "The Transfer of heat by Self-induced flow in a rotating tube", ASME Journal of Turbo-machinery, Vol. 116, 1994, 316-326.

[2] Chul-Huyng Lee, M. AL-Ajlouni, N. Syred, "Centrifuges design for submicron particle separation", Journal of Energy Research and Development, Vol. 17 No. 3-4, 1995, 51-59.

[3] AL-Ajlouni M, Studies of rotating high speed separation systems, PhD Thesis, UWCC, Cardiff, UK; 1996.

[4] T. G. Hughes, M. C. R Davies, P. R. Taunton, "The small scale modelling of masonry arch bridges using a centrifuge", Proceedings of the Institute of Civil Engineers, Journal of Structures & Buildings, Vol. 128, 1998, 49-58.

[5] M. Al-Ajlouni, A. Al-Hamdan, "Engine exhaust operated ejector for vehicle air conditioning" , Mu'tah Journal for Research and Studies, Vol. 17 No. 3, 2002, 119-137.

[6] A. E. Puckett, "Supersonic Nozzle Design", Journal of Applied mechanics, Transaction of ASME, Vol. 13 No. 4, 1946, 265-270.

[7] Dimarogonas, A D, Machine Design: A CAD Approach, 2nd ed. New York: John Wiley and sons inc; 2001.

[8] Amirouche F, Principles of Computer-Aided Design and Manufacturing, 2nd ed. Upper Saddle River, New Jersey: Pearson Prentice Hall; 2004.

[9] Kuethe A M, Chow Ch-Y, Foundations of Aerodynamics, 5th ed. New York: John Wiley and sons inc.; 1998.

[10] Fox R W., McDonald A T, Introduction to Fluid Mechanics, 4th ed. New York: John Wiley and sons inc.; 1992.

[11] Streeter V L, Wylie E B, Fluid Mechanics, 8th ed. London: McGraw Hill Book Company; 1985.

[12] Massey B S, Mechanics of Fluid, 5th ed. Reinhold: Van Nostrand; 1983.

[13] Bertin J J, Smith M L, Aerodynamics for Engineers, 3rd. Upper Saddle River, New Jersey: Prentice Hall; 1998.

[14] Saravanamuttoo H, Rogers G, Cohen H, Gas Turbine Theory, 5th ed. Harlow: Pearson Prentice Hall; 2001.

[15] James J, Gas dynamics, 3rd ed. New Jersey: Prentice Hall; 2007.

[16] Liepmann H W, Roshko A, Elements of Gas Dynamics, New York: John Wiley and sons inc.; 1957.

[17] Saad M A, Compressible Fluid Flow, 2nd ed. New Jersey: Prentice Hall; 1993.

[18] Y-H Liu, "Experimental and numerical investigation of circularly lobed nozzle with/without central plug", International Journal of Heat and Mass Transfer, Vol. 45, 2002, 2577–2585.

.

[19] M. Geron, R. Paciorri, F. Nasuti, F. Sabetta, "Flow field analysis of a linear clustered plug nozzle with round-to-square modules", Aerospace Science and Technology, Vol. 11, 2007, 110–118

[20] T. Zebbiche, Z. Youbi, "Effect of Stagnation Temperature on the Supersonic Two-Dimensional Plug Nozzle Conception. Application for Air", Chinese Journal of Aeronautics, Vol. 20, 2007, 15-28.

[21] T. Zebbiche, Z. Youbi, "Supersonic Two-Dimensional Minimum Length Nozzle Design at High Temperature. Application for Air", Chinese Journal of Aeronautics, Vol. 20, 2007, 29-39.

[22] Houghton E L, Carpenter B W, Aerodynamics For Engineering Students, 4th ed. London: Edward Arnold; 1993.

Appendix A. Appendix Description of the software package:

The developed software package was implemented using the programming language Visual Basic (VB6). It consists of many standard forms like the splash screen, the log in dialog (password), the about dialog, the common dialogs (like open, save and color), introductory menu, and others. Figure 2 presents the main window of the software package. This window is one of the important interface windows throughout the software package. The type of this window is a multiple document interface (MID) and it is a parent window for the other windows. Through this window the designer can activate the following buttons that open the child windows

1. Air Properties.: to open the window to be used to enter the working fluid properties: e.g., the specific heats ratio, inlet pressure, and the inlet temperature.
2. Input data: to open the window to be used to enter the mass flow rate, the number of the nozzle and the required Mach number.
3. Calculations and Results: to open the window to initialize the calculations and to choose the type of the output. This is the most interactive window and will be described afterward in more detail.
4. References: to link with WinWord document that contains details about the references.
5. Exit: to terminate the package when needed.

Moreover, other buttons and menu items can be activated from this window. Figure 3 presents the Calculations and Results window. On this window, the user can start the calculation after the inspection of the inputs. The nozzle profile will be displayed as a plot using the most advanced plotting commands to add a dynamic axis, scale and a tracing point. The same information can be extracted in a listed form through a dynamic list box. This list box has been linked internally to the plot area. Clicking any value in the list box will be displayed directly in the plotting area as the tracing point. Other type of output can be obtained as a soft or hard copy of the results by importing data from the software into a document file (WinWord), text file (WordPad) or printed hard copy. In addition, the software package includes an error tracking system of messages. For example, it reminds the user of missing data, or illogical entries.

JJMIE

Volume 4, Number 3, June, 2010
ISSN 1995-6665
Pages 412 - 417

Jordan Journal of Mechanical and Industrial Engineering

Simulation and Modeling of Bubble Motion in an Electrolytic Bath of Soderberg Pot

C. Karuppannan, T.Kannadasan

CIT Sandwich Polytechnic College, Coimbatore-641 014, Tamilnadu, India

Abstract:

In Aluminium manufacturing the Soderberg pot is widely used. The study explains about the bubble motion in cryolite liquid in a Soderberg pot anode face using comprehensive VOF multiphase model in FLUENT, under the action of gravitation. The distribution of bubbles introduced under the anodes of an aluminum reduction cell at the initial time has fixed size. 2D simulation results are reported for four cases with different initial conditions for the bubbles, physics and geometries.

Keywords: Bubble analysis; Aluminium manufacturing;numerical simulation;VOF model.

1. Introduction

In aluminium manufacturing, formation of bubbles is a major problem. Soderberg pots are used for the manufacture of aluminium. In Soderberg pot, the bubbles are formed in the interpolar distance and deposited on the anode face due to the thermal and chemical reactions in the electrolytic bath. It reduces the input power and increases the energy consumption and reduces the current efficiency. Reduction in the formation of bubbles will increase the current efficiency of the pot and output of aluminium. From the previous studies, the temperature distribution is clearly studied and proved. It has been reported that formation of bubbles is from the anode surface. Hence, a model of the anode surface is taken for the analysis. Initial distributions of bubbles and diameters of the bubbles are taken at random. Bubbles considered are having a non-zero density and deformable body; therefore having an appropriate mass (depending on the volume), hence providing a more accurate mathematical model. With the aid of comprehensive **Volume Of Fluid** (VOF) model in FLUENT under the action of gravitation, the formed bubbles are coalescence and collapsed. The result is compared with the mathematical model. The above work proves that the bubbles are collapsed with the increase in pressure in the feeding of Alumina. In this we can achieve the result accurately and enhance the current efficiency and quality of Aluminium production.

2. Governing Equations

To solve the given cryolite and bubble phase flow, field employs the conservation equations for mass and momentum for incompressible fluid.

$$\nabla \cdot u \tag{1}$$

$$\frac{\partial(\rho u_j)}{\partial t} + \nabla \cdot (\rho u_i u_j) = -\nabla p + \rho g_j + \nabla \cdot \mu\{(\nabla \bar{u}) + (\nabla \bar{u})^T\} + F_j; \text{where j = cryolite} \tag{2}$$

Momentum equations are solved for both cryolite and fluid. Continuum surface model (CSF) is used to describe the interfacial surface tension.

$$\frac{(\alpha_q^n \rho_q^n - \alpha_q^{n-1} \rho_q^{n-1})}{\Delta t} + \sum_{nof} (\rho_q U_{nof}^{n-1} \alpha_{q,nof}^{n-1}) = \sum_{p=1}^{2} (\dot{m}_{pq} - \dot{m}_{\text{p}} \tag{3}$$

Equation (3) represents the VOF model governing equation for the cryolite-bubble phase model, where density and viscosity are defined

$$\rho\_mix = \alpha\_air\ \rho\_air + (1 - \alpha\_air)\ \rho\_cryolite$$

and

$$\mu_{mix} = \alpha_{air} \mu_{air} + (1 - \alpha_{air}) \mu_{cryolite}$$

Primary volume fraction will be computed based on

$$\alpha_{cryolite} + \alpha_{air} \tag{4}$$

3. Numerical Solution

Properties of cryolite and bubble used for the analysis are shown in Table 1. Model and meshing are done in GAMBIT.

Table 1 Properties of Cryolite and Bubble

Property	Cryolite	Air (Bubble)
Density	2567 kg/m^3	1.225 kg/m^3
Viscosity	1.57 cP	0.017894 cP
Surface Tension	0.05 N/m	

The model presented in this paper used VOF model (2).

$$\alpha_{air}(x, y, t), \text{volume fraction} = \begin{cases} 0, \textit{cell filled with fully cryolite} \\ 1, \textit{cell filled with fully air} \\ > 0 \ \textit{and} < 1, \textit{mixture of cryolite and} \end{cases} \tag{5}$$

For interpolation of cryolite-bubble interface cell region, Geometric Reconstruction Scheme is used. The geometric reconstruction scheme represents the interface between fluids using a piecewise-linear approach. When the cell is near the interface between two phases, the geometric reconstruction scheme is used to obtain the face fluxes. It assumes that the interface between two fluids has a linear slope within each cell, and uses this linear shape

 © 2010 Jordan Journal of Mechanical and Industrial Engineering. All rights reserved – Volume4, Number 3 (ISSN 1995-6665)

for calculation of the advection of fluid through the cell faces. The first step in this reconstruction scheme is calculating the position of the linear interface relative to the center of each partially-filled cell, based on information about the volume fraction and its derivatives in the cell. The second step is calculating the amount of fluid through each face normally using the computed linear interface representation and information about the normal and tangential velocity distribution on the face. The third step is calculating the volume fraction in each cell using the balance of fluxes calculated during the previous step.

Body force weighted scheme for differencing, Explicit scheme for temporal and PISO for pressure velocity coupling is used for solving.

4. Results & Discussions

4.1. Case 1: Coalescence with Gravity: Small Bubble and Big Bubble Below

Domain dimensions are 20 mm x 10 mm surface. Geometry with three fluid zones is modelled viz., Cryolite, Bigger bubble and smaller bubble. Bubble walls are marked as interior. Results at time steps 0s, 0.03s, 0.033s, 0.036s are shown.

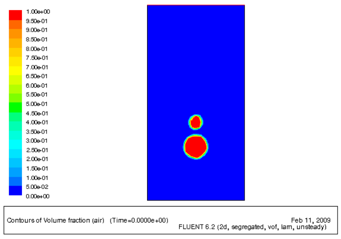

a) initial configuration at t = 0s

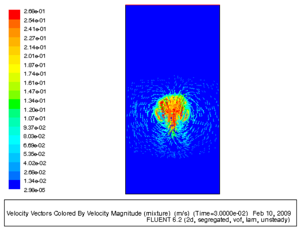

b) t = 0.03s

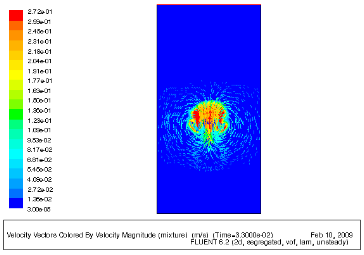

t = 0.033s

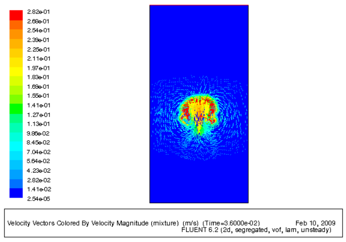

t = 0.036s

Figure 4-1. Coalescence of two rigid circular bubbles. The contours of the bubbles as well as the fluid velocity vectors are shown.

The above results show that the bubbles move through the cryolite medium towards upwards under the action of buoyancy since the system is in the gravitational field. The bubbles having a lower density than the surrounding liquid medium displace the liquid, volume equivalent to their own volume and this displaced liquid wants to push the bubble upwards so as to occupy its volume. This is in accordance with the Archimedes' principle. Also, bigger bubble moves faster than the smaller bubble due to different buoyant force exerted depending on their volume. This phenomenon therefore contributes to the different velocities of the bubbles.

The coalescence occurs already at time 0.03 seconds as opposed to the results depicted in the paper (3). This can be just due to different densities of the continuous fluid (in our case cryolite) which causes different speeds being attained by the bubble, hence decreasing the time to coalesce. The animation also shows the bigger bubble attaining a protruded shape in the beginning owing to being in the wake of the smaller bubble due to which it is in a low pressure region and gets specially pulled into the smaller bubble before coalescence occurs. These findings can be verified by the paper (3).

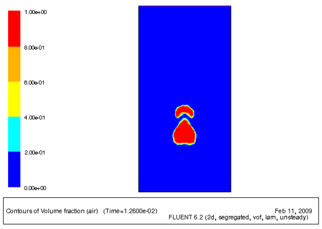

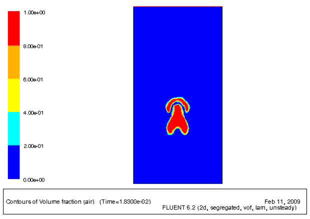

Figure 4-2. Typical C-shape morphology attained by the smaller bubble. Protruding shape of the bigger bubble, caught in the wake of the rising smaller bubble

4.2. Case 2: Surface Tension Effect: Single Elliptical Bubble with Different Surface Tension Values of the Fluid

Domain dimensions are 20 mm x 12 mm. Normal bubble rising problem with constant surface tension specification (0.05 N/m). Results at time steps t = 0.1s, t = 0.1s, t = 0.05s are shown.

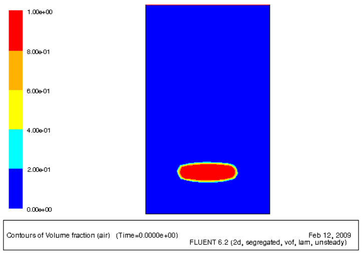
a) initial configuration, t=0s

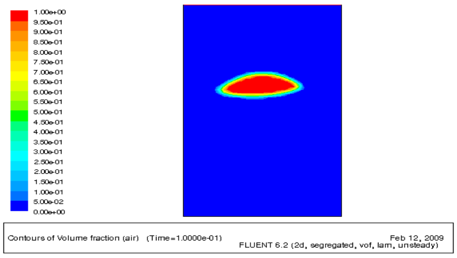
b) bubble configuration at t = 0.1s, α_s = 0.05 N/m

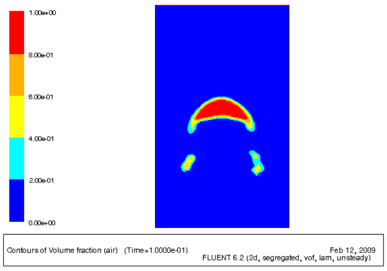
c) t = 0.1s, α_s = 0.005 N/m

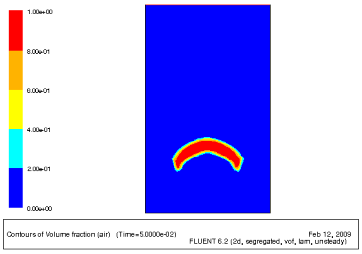
d) time 0.05s, α_s = 0.0005 N/m

Figure 4-3. Influence of the surface tension coefficient α_s

The above results match with the results of the publication qualitatively, although the more intricate details like bubble break-up owing to lower surface tension (figure 2.1(c)) have not been captured in the paper. Besides, the C-shape morphology attained due to the low pressure region in the wake of the rising bubble has been captured much better in the FLUENT simulation. The velocity vector plots overlaid on the bubble images for the four situations explain these phenomena.

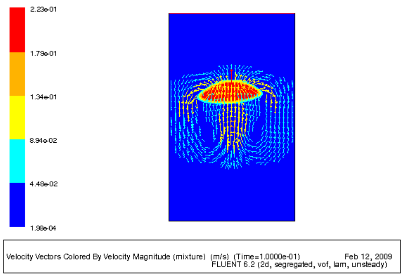
Bubble configurations at a) t = 0.1s, α_s = 0.05 N/m

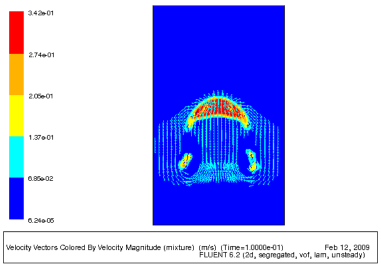
b) t = 0.1s, α_s = 0.005 N/m;

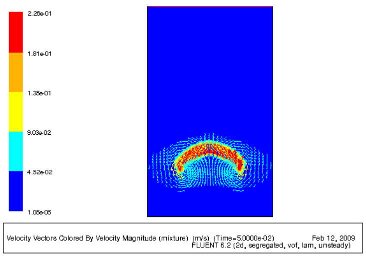
c) time 0.05s, α_s = 0.0005 N/m

Figure 4-4. Rising bubbles attaining different shapes owing to the recirculation zone below them

These results are in perfect harmony with the simulation results of the independent group which was mentioned earlier (3).

4.3. Case 3: Rigid Ellipsoidal Bubble Rising Around an Angular Wall

Domain dimensions are 2 x 2 cm with two angled walls Normal bubble rising problem with constant surface tension specification (0.05 N/m). Surface tension was included to come closer to the case description. Due to surface tension, the bubble tends to attain minimum surface area as the liquid has a phobia towards it. As the surface tension value is quite high in our case, the bubble should not undergo easy break-up.

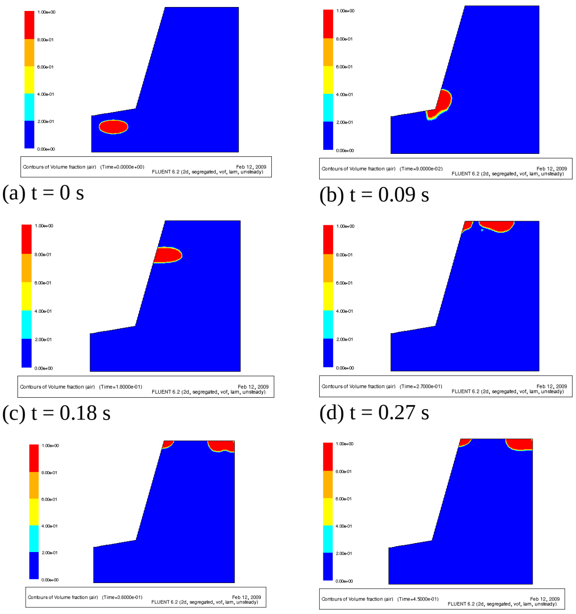

(a) t = 0 s (b) t = 0.09 s

(c) t = 0.18 s (d) t = 0.27 s

(e) t = 0.36 s (f) t = 0.45 s

Figure 4-5. Air bubble position at different times under stronger surface tension effects

The bubble is at different positions compared to the literature values. This must be due to different densities being taken for the liquid phase (our liquid is cryolite). As the surface tension effects are considerable, the bubble tends to avoid contact with the liquid (and rather prefers contact with the wall) while moving up under the action of buoyancy. The following images show the bubble behaviour for weaker surface tension effects of the liquid, where the bubble does not necessarily oppose contact with the liquid while moving up due to buoyancy

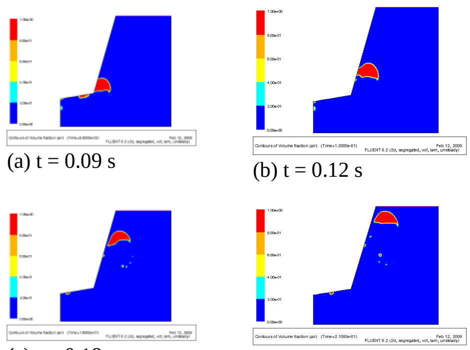

(a) t = 0.09 s (b) t = 0.12 s

(c) t = 0.18 s (d) t = 0.21 s

Figure 4-6. Air bubble position at different times under weaker surface tension effects

4.4. Case 4: Around 20 Bubbles with Random Distribution Rising in a Column

Domain dimensions are 8 cm x 4 cm. 20 numbers of bubbles are taken for the analysis. Analysis is done for 27 time steps

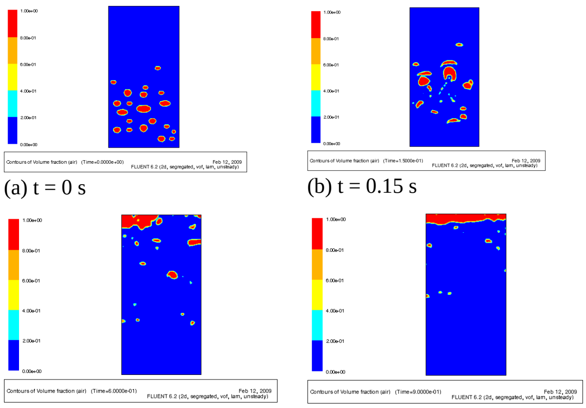

(a) t = 0 s (b) t = 0.15 s

(c) t = 0.6 s (d) t = 0.9 s

Figure 4-7 .Twenty air bubbles coalescing and rising under strong surface tension and buoyancy effect

The results show that the buoyant force acts on all of the bubbles and pushes them upwards. It is also visible that the bubbles below are caught up in the wake of the ones above them and are pulled towards such low pressure areas due to which they end up moving even in a zigzag fashion. The surface tension value being high, results in the bubbles coalescing as the liquid would prefer to minimize the surface contact area with the bubbles. As a result, the number of bubbles reduces drastically and ultimately there is an air column formed in the top region of the column. Some of the small bubbles are caught up in the eddies and tend to remain for relatively longer period within the liquid as they easily give-in to the fluid behavior due to their own lower inertia

5. Conclusion:

Since the results obtained by the VOF multiphase model of FLUENT demonstrate the typical C-shape morphology of the bubbles as they rise up the column (as evident from the animation), the FLUENT results are much more accurate compared to the simplified mathematical model applied in the publication. Multi bubble analysis shows the real effect of bubble in the bottom of the anode plate in soderberg pot. The formed bubbles are collapsed with the aid of increasing the pressure in the feeding of Alumina and prevent the bubbles deposited on the anode surface. Hence, we can obtain the minimum energy consumption and enhance the current efficiency in the soderberg pot.

References

[1] A New Study On Bubble Behavior On Carbon Anode In Aluminum Electrolysis. Gao, Bingliang, et al. [ed.] Halvor Kvande. s.l. : TMS (The Minerals, Metals & Materials Society), Light Metals 2005.

[2] Numerical Simulation Of Bubble Coalescence Using A Volume Of Fluid (Vof) Model. Delnoij, E, Kuipers, J.A.M. and Van Swaaij, W. P. Lyon : s.n., 1998. Third International Conference on Multiphase Flow, ICMF'98.

[3] A New Modelling For Simulating Bubble Motions In A Smelter. Michel, V. Romerio, Alexei, Lozinski and Jacques, Rappaz. [ed.] Halvor Kvande. s.l. : The Minerals, Metals & Materials Society), Light Metals 2005.

[4] B. Glorieux et al., "Density of Superheated and Undercooled Liquid Alumina by a Contactless Method", Int. J. Thermophys., Vol. 20, No. 4, 1999, 1085 – 1094.

[6] M.Dupuis, "Computation of Aluminum reduction Cell Energy Balance Using ANSYS® Finite Element Models", TMS Light Metals, 1998, 409 – 417.

[7] M. Dupuis and al., "Cathode Shell Stress Modelling", TMS Light Metals, 1991, 427 – 430.

[8] M. Dupuis, " Computation of Accurate Horizontal Current Density on Metal Pad Using a Full Quarter Cell Thermo-electric Model", CIM Light Metals, 2001, 3-11.

[9] M. Dupuis and I. Tabsh, "Thermo-Electro-Magnetic Modeling of a Hall-Heroult Cell", Proceeding of the ANSYS ® Magnetic Symposium, 1994, 9.3 – 9.13.

[10] M. Segatz and D.Vogelsang, "Effect of Steel Parts on Magnetic Fields in Aluminum Reduction Cells", TMS Light Metals, 1991, 393 – 398.

[11] D.Richard and al., "Thermo-electro-mechanical Modelling of the Contact between Steel and Carbon Cylinders using the Finite Element Method", TMS Light Metals, 2000, 523-528.

[5] T.J.Chung, Computational Fluid Dynamics, Cambridge, UK, Cambridge University Press, 2002.

[12] I.Eick and D.Vogelsang, "Dimensioning of Cooling Fins for High – Amperage Reduction Cells", TMS Light Metals, 1999, 339 – 345.

[13] C.Vanvoren and al., "AP 50: The Pechiney 500 kA cell", TMS Light Metals, 2001, 221 -226.

[14] H.Kvande and W.Haupin, "Inert Anodes for AI Smelters: Energy Balance and Environmental Impact" JOM, Vol. 53, No. 5, 2001, 29-33.

[15] Bruggeman and D.J.Danka, "Two-Dimensional Thermal Modelling of the Hall-Heroult Cell", Light Metals, 1990, 203-209.

[16] Schmidt-Hatting and al., "Heat Losses of Different Pots". Light Metals, 1985, 609-624.

[17] Antille and al., "Effects of Current Increase of Aluminium Reduction Cells", Light Metals, 1995, 315-321.

JJMIE

Volume 4, Number 3, June, 2010
ISSN 1995-6665
Pages 418 - 423

Jordan Journal of Mechanical and Industrial Engineering

A Mathematical Study for Investigation the Problems of Soft Shells Materials

N.Al-Kloub[a] ,M. A. Nawafleh[*,b], M. Tarawneh[c] and F. Al-Ghathian[a]

[a]Department of Mechanical Engineering, Al-Balqa' Applied University, Amman, Jordan

[b]Department of Civil Engineering, Al-Hussein Bin Talal University, Ma'an, Jordan

[c] Department of Mechanical Engineering, Mutah University, Karak, Jordan

Abstract

The current study investigates the problems of soft shells theory for manufacturing composite products by superimposition on each 2D layers. Analytical and numerical methods are considered to study the layers imposing winding around the half-finished materials or pulling some additional shells on the surface of materials which are partly made. Based on this, the smoothness of layers, and the criteria of the absence of wrinkles and folds are obtained. Methods for calculation the deformations and residual stresses of the textile structure of used materials were established. The results obtained by the analytical and numerical methods indicated that it is possible to establish mathematical equations which can be applied to find the strains and stresses developed in the shells and bands and their pressure on the surfaces of covered solid. The results of the present work can also be implemented for manufacturing composite materials having complex geometric forms.

Key words: Soft Shell, Band; Deformation; Numerical Method;Strain and Stress.

1. Introduction

There are various processes to manufacturing the composite products by successive superimposition on each 2D layers that are glued mutually by some adhesive substance [1, 2]. In this study the problems of the capacity bands of the layer and shells that slightly resist bending forces (soft shells or membranes) are investigated. The production of these layers imposes on the surface of the materials during the forming process may be winding around the half-finished materials or pulling some additional shells on the surface of mistrials which are partly made. The composites may also be produced by successive inflating soft shells inside of some half-finished materials.

Whatever the methods are considered, some common problems of the theory of soft shells are appeared. Some of these problems are investigated in the present work, those that concern the changes undergone by textile structures of the bands or the shells as these bands and shells are fastened to the surfaces of the materials during the production stage . To predict the changes, it is necessary to develop methods for investigations of stress and strain distributions in the soft shells [2, 3]. The methods based on the mathematical study of stress-strain conditions of the soft shells [4] will be discussed in this paper. These studies include static equilibrium equations of the theory of the soft shell, the deformation equations of 2D materials as well as boundary conditions. The boundary value problems of various technologies for producing the composites are considered in connection with these equations. Solutions of these problems can be obtained by asymptotic analytical and numerical methods. Methods of small segment are also investigated when the problems of winding 2D bands around the solids of revolution which only in small measure differ from cylindrical ones. The bands of various textile structures and width are considered at different conditions of supplying band by feeding devises which determine the forms of cross sections of bands at different distances of the section to the solid surface.

Numerical methods are developed for investigation the interaction of the soft shells when they cover a solid. For calculations, the finite element method was used. By assuming that the strain energy density of the shell material is known, function of the shell strain measured in this method leads to minimization the potential energy of the whole shell. Problems of the minimization were reduced to the solution of non-linear algebraic equations sets. A certain methods with respect to the loading parameter are used to find the solutions of such equations.

2. Equilibrium Equations of the Theory of the Soft Shell

To derive the equilibrium equation two cylindrical shapes are suggested. The shape of R, φ, ζ is used to describe the form of the shell (see Figure 1) which is not subjected to any stress. This form can be defined by the equation:

[*] Corresponding author. Tel.: m_nawafleh@ahu.edu.jo.

$$R = R_0\left(\varphi, \zeta\right) \tag{1}$$

The variables φ and ζ are considered as the Lagrange coordinates on the shell. In the other (spatial) system of cylindrical coordinates R, ψ, z (see Figure2) the form of the stressed shell is defined by the equation:

$$r = r\left(\psi, z\right) \tag{2}$$

where the axis z coincides with the axis ζ, r = the radius of the feeding cylinder

According to [5,6], the stress components σ_{11},

$\sigma_{12} = \sigma_{21}$ and σ_{22} are defined by the formulas

$$\boldsymbol{\sigma}_1 = \mathbf{e}_1\sigma_{11} + \mathbf{e}_2\sigma_{12} \tag{3}$$

$$\boldsymbol{\sigma}_2 = \mathbf{e}_1\sigma_{21} + \mathbf{e}_2\sigma_{22} \tag{4}$$

$$\mathbf{e}_1 = \frac{\partial r}{\partial \varphi} / \left|\frac{\partial r}{\partial \varphi}\right| \tag{5}$$

$$\mathbf{e}_2 = \frac{\partial r}{\partial \zeta} / \left|\frac{\partial r}{\partial \zeta}\right| \tag{6}$$

Where, $\boldsymbol{\sigma}_1$ and $\boldsymbol{\sigma}_2$ are the stress vectors on coordinate lines $\zeta = const$ and $\varphi = const$, respectively.

in this case the equilibrium equation for the shell is taken in the vector form [7]:

$$\frac{\partial}{\partial\varphi}\left(\boldsymbol{\sigma}_1\left|\frac{\partial \mathbf{r}}{\partial\zeta}\right|\right) + \frac{\partial}{\partial\zeta}\left(\boldsymbol{\sigma}_2\left|\frac{\partial \mathbf{r}}{\partial\varphi}\right|\right) + \mathbf{q}\sqrt{g_{11}^0 g_{22}^0 - \left(g_{12}^0\right)^2} = 0 \tag{7}$$

Where the vector $\mathbf{q}$ is the intensity of the external forces acting on the shells surface and g_{ij}^0 and g_{ij} (i,j=1,2) are metric coefficients of the shell corresponding to unstressed and stressed state respectively.

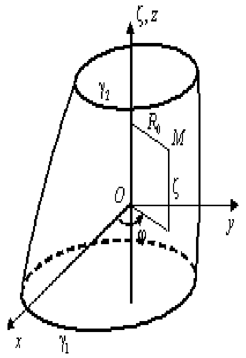

Figure 1.The shell in unstressed state

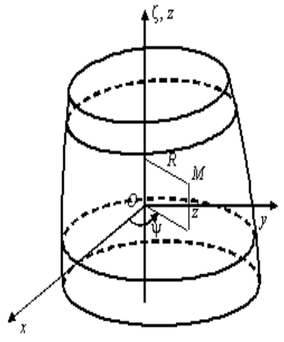

Figure 2. The shell on the solid's surface

3. Established equations of shell material

By considering the macroscopically measures of the shell deformation, the magnitude of the extension strains of coordinate lines are:

$$\varepsilon_1 = \lambda_1 - 1 \tag{8}$$

$$\varepsilon_2 = \lambda_2 - 1 \tag{9}$$

Where λ_1 and λ_2 are the elongation rates of coordinate lines.

The magnitude of the angle between these lines χ is determined by the equation:

$$g_{12} = \sqrt{g_{11}^0 g_{22}^0}\lambda_1\lambda_2 \sin\chi \cdot \tag{10}$$

λ_1 and λ_2 can be determined by formulas:

$$\lambda_1 = \sqrt{\frac{g_{11}}{g_{11}^0}} \tag{11}$$

$$\lambda_2 = \sqrt{\frac{g_{22}}{g_{22}^0}} \tag{12}$$

The established equations are obtained for deformation shells which allow the introduction of the potential strain energy. In previous works [5, 9], the equations are given in the following form:

$$\sigma_{11} = \frac{1}{\lambda_2\sqrt{g_{11}^0 g_{22}^0}}\left(\frac{\partial u}{\partial\lambda_1} + \frac{ctg\chi}{\lambda_1}\frac{\partial u}{\partial\chi}\right) \tag{13}$$

$$\sigma_{22} = \frac{1}{\lambda_1\sqrt{g_{11}^0 g_{22}^0}}\left(\frac{\partial u}{\partial\lambda_2} + \frac{ctg\chi}{\lambda_2}\frac{\partial u}{\partial\chi}\right) \tag{14}$$

$$\sigma_{12} = \sigma_{21} = -\frac{1}{\lambda_1\lambda_2\sin\chi\sqrt{g_{11}^0 g_{22}^0}}\frac{\partial u}{\partial\chi} \tag{15}$$

Where u is the density of the strain energy, related to the unit of the area of the unstressed shell.

In [5] u was calculated as a function of $\chi, \varepsilon_1, \varepsilon_2$ for some various textile structures. This study will concentrate by considering the shell is made of nets with rectangular meshes.

4. Investigation of The Variation Principle of Pulled Shell on The Solid Surface

The surface of the solid on which the shell will be pulled (see Figure 2), can be defined by the following equation:

$$R = R\left(\mu, \psi, z\right) \tag{16}$$

where, μ is an artificially introduced parameter variation which leads to the changing of the solids form.

The radius-vector of any particle M of the shell when it is pulled on the solid surface can be presented as follows:

$$\mathbf{r} = \left(R_0(\varphi,\zeta) + \rho(\mu,\varphi,\zeta)\right)\cos\left(\varphi + \theta(\mu,\varphi,\zeta)\right)\mathbf{i} + \left(R_0(\varphi,\zeta) + \rho(\mu,\varphi,\zeta)\right)\sin\left(\varphi + \theta(\mu,\varphi,\zeta)\right)\mathbf{j} + \left(\zeta + w(\mu,\varphi,\zeta)\right)\mathbf{k} \quad (17)$$

where $\theta(\mu,\varphi,\zeta)$ is the increment of the angular coordinate of the particle M, $\rho(\mu,\varphi,\zeta)$ and $w(\mu,\varphi,\zeta)$ are the radial and vertical displacements, respectively; $\mathbf{i}, \mathbf{j}, \mathbf{k}$ are unit vectors along the axes x, y and z respectively.

It is obvious that the following equations are true:

$$R\left(\mu, \varphi + \theta(\mu,\varphi,\zeta), \zeta + w(\mu,\varphi,\zeta)\right) = R_0(\varphi,\zeta) + \rho(\mu,\varphi,\zeta) \quad (18)$$

$$\psi = \varphi + \theta(\mu,\varphi,\zeta) \quad (19)$$

$$z = \zeta + w(\mu,\varphi,\zeta) \quad (20)$$

The equation (18) shows that to obtain the full description of shell deformation it is enough to know the functions $\theta(\mu,\varphi,\zeta)$ and $w(\mu,\varphi,\zeta)$.

To describe the deformation of the shell on the surface of the solid, the expressions for the metric coefficients can be written firstly, to initial unstressed state, and, secondly, to final deformed state. According to equations (1-6), these coefficients are given by the following equations:

$$g_{11}^0 = \left(\frac{\partial R_0}{\partial \varphi}\right)^2 + R_0^2 \quad (21)$$

$$g_{22}^0 = \left(\frac{\partial R_0}{\partial \zeta}\right)^2 + 1 \quad (22)$$

$$g_{12}^0 = g_{21}^0 = \frac{\partial R_0}{\partial \varphi}\frac{\partial R_0}{\partial \zeta} \quad (23)$$

$$g_{11} = \left(\frac{\partial \mathbf{r}}{\partial \varphi}\right)^2 \quad (24)$$

$$g_{22} = \left(\frac{\partial \mathbf{r}}{\partial \zeta}\right)^2 \quad (25)$$

$$g_{12} = g_{21} = \frac{\partial \mathbf{r}}{\partial \varphi}\frac{\partial \mathbf{r}}{\partial \zeta} \quad (26)$$

Where, $\mathbf{r}$ is defined by Eq. (17) and Eq. (18) which allow to eliminate $\rho(\mu,\varphi,\zeta)$.

By the computation, it was assumed that all points of the bottom edge γ_1 of the soft shell have coordinates $\zeta = 0$, and points of the top edge γ_2 – have coordinates $\zeta = H$. Thus the potential energy of the whole shell equals

$$U = \int_0^H \int_0^{2\pi} u\sqrt{g_{11}^0 g_{22}^0 - g_{12}^0}\, d\varphi d\zeta \quad (27)$$

Where, u is a function of Φ, depending on displacements $\theta(\mu,\varphi,\zeta)$ and $w(\mu,\varphi,\zeta)$ of the shell particles and the first derivatives of these displacements:

$$u = \Phi\left(\mu, \varphi, \zeta, \theta, w, \frac{\partial \theta}{\partial \varphi}, \frac{\partial \theta}{\partial \zeta}, \frac{\partial w}{\partial \varphi}, \frac{\partial w}{\partial \zeta}\right) \quad (28)$$

to investigate the displacements $\theta(\mu,\varphi,\zeta)$ and $w(\mu,\varphi,\zeta)$, which satisfy the boundary conditions of the clamped edges, the conditions are given by the following equations:

$$\theta(\mu,\varphi,0) = \theta_0(\varphi) + \mu\theta_0^*(\varphi) \quad (29)$$

$$\theta(\mu,\varphi,H) = \theta_1(\varphi) + \mu\theta_1^*(\varphi) \quad (30)$$

$$w(\mu,\varphi,0) = w_0(\varphi) + \mu w_0^*(\varphi) \quad (31)$$

$$w(\mu,\varphi,H) = w_1(\varphi) + \mu w_1^*(\varphi) \quad (32)$$

where, θ_0, θ_0^*, θ_1, θ_1^*, w_0, w_0^*, w_1 and w_1^* are arbitrary given functions.

The analysis of the deformed state of the shell is based on the variation principle of the minimum of the potential strain energy [8]. Based on this principle, the equilibrium state of the shell corresponds to the minimum of the energy

5. Finite Element Method for the Investigation of Pulled Shell on the Solids' Surface

Minimization of the functional U was accomplished by the finite element method and small parameter method [9,10]. To apply the finite element method, the definition domain of functions $\theta(\mu,\varphi,\zeta)$ and $w(\mu,\varphi,\zeta)$ is subjected to the triangulation. These functions are approximated as follows [4]:

$$\theta = \sum_k T_k p_k \quad (33)$$

$$w = \sum_k V_k p_k \quad (34)$$

Where, p_k is shape functions, T_k and V_k are nodal magnitudes of $\theta(\mu,\varphi,\zeta)$ and $w(\mu,\varphi,\zeta)$ respectively, k =1,…, and r is the node number (number of coefficients X_k).

When using such approximations of U by the formula (14), U can be appeared as a function of coefficients T_k and V_k. By equating the partial derivatives of this function with respect to mentioned coefficients to zero, a group of algebraic equations is obtained. The solution provides the nodal displacements.

At the topmost and bottommost strings of nodes (their quantities will be denoted by $2m$) in accordance to Eqs. (21-26). The values of T_i and V_i may be given arbitrary. Thus, the following designations can be given:

$$X_{2k-1} = T_{k+m},\ X_{2k} = V_{k+m} \quad (35)$$

In this case U transforms into the function of X_k.

To derive equations for the calculation of the coefficients X_k, the conditions of minimum energy U can be represented by the following equation:

$$\frac{\partial U}{\partial X_k} = 0 \quad (36)$$

In order to analyze the results of nonlinear equation, the differentiation can be taken for all equations with respect to the parameter μ. As a result, a linear equation in regarding to derivatives $\frac{dX_k}{d\mu}$ can be obtained.

The last equation set may be represented in the following form:

$$C(\mu, X(\mu))\frac{dX}{d\mu} = B(\mu, X(\mu)) \quad (37)$$

Where, C is a matrix of the format $r \times r$, B is a vector of length r, X is a required vector of the length. Thus, the equation (37) represents a group of the ordinary differential equations from which $T_k(\mu)$ and $V_k(\mu)$ should be found. The solution of this group leads to the Cauchy problem if $T_k(0)$ and $V_k(0)$, or more definitely $X_k(0)$, are known values. By rewriting Eq. (37) in the form of:

$$\frac{dX}{d\mu} = C^{-1}(\mu, X(\mu))B(\mu, X(\mu)) \quad (38)$$

the required solution can be achieved by the following method:

$$\left.\begin{aligned} &X(\Delta\mu) = X(0) + \left.\frac{dX}{d\mu}\right|_{\mu=0} \\ &\Delta\mu = X(0) + C^{-1}(0, X(0))B(0, X(0))\Delta\mu \end{aligned}\right\} \quad (39)$$

$$\left.\begin{aligned} &X(\mu_k + \Delta\mu) = X(\mu_k) + \left.\frac{dX}{d\mu}\right|_{\mu=\mu_k} \\ &\Delta\mu = X(\mu_k) + C^{-1}(\mu_k, X(\mu_k))B(\mu_k, X(\mu_k))\Delta\mu \end{aligned}\right\} \quad (40)$$

Thus, the deformation of the shell can be calculated at any given value of μ. If the solution of this problem is known at $\mu = 0$, i.e. if initial conditions are known for Cauchy problem, this can be related to equation (38).

It is possible to specify various methods to establish such initial conditions. The elementary method consists one-parametrical group of solids with the parameter μ. There is an obvious trivial solution at $X = 0$, and if the group remains the same at $\mu = \mu_*$, therefore, the surface of a body will have the demanded form, and at $\mu = 0$ this surface coincides with a surface of no deformed shell.

By considering the position of a cylindrical shell with the radius R_0 and length H on the solid surface, mathematically, this can be represented by the following equation [11]:

$$R(z) = R_0 + \mu z + A\mu\sin\psi \quad (41)$$

Where, μ is the above mentioned parameter and A is some arbitrary chosen parameter.

In this case of zero value of the parameter μ it is possible to subject to such position of the shell on the solid surface, then this shell would not be deformed. This exact solution can be used as initial condition in the investigation of Cauchy problem for calculation of the state of the shell. Boundary conditions will be chosen so that one edge of the shell corresponds to the coordinate $z = 0$, and another to the coordinate $z = H$. In this case metric coefficients corresponding to the unstressed state of the shell are as follows:

$$g_{11}^0 = R_0^2,\ g_{12}^0 = g_{21}^0 = 0,\ g_{22}^0 = 1 \quad (42)$$

By referring to equations (13) and (23) the metric coefficients corresponding to the deformed state of the shell are given by:

$$g_{11} = \mu^2\left(A\cos\psi\left(1 + \frac{\partial\theta}{\partial\varphi}\right) + \frac{\partial w}{\partial\varphi}\right)^2 + (R_0 + \mu z + A\mu\sin\psi)^2\left(1 + \frac{\partial\theta}{\partial\varphi}\right)^2 + \left(\frac{\partial w}{\partial\varphi}\right)^2 \quad (43)$$

$$g_{22} = \mu^2\left(A\cos\psi\frac{\partial\theta}{\partial\zeta} + \left(1 + \frac{\partial w}{\partial\zeta}\right)\right)^2 + (R_0 + \mu z + A\mu\sin\psi)^2\left(\frac{\partial\theta}{\partial\zeta}\right)^2 + \left(1 + \frac{\partial w}{\partial\zeta}\right)^2 \quad (44)$$

If $\mu = 0$ then it is easy to notice that equations (42), (43) and (44) coincide

6. Analytical Method of Small Segment for Investigation of Shell Pulled on the Solid Surface

There are many difficulties in interpretation of above mentioned cases when numerical methods fail. As a rule, it is insignificant modification of boundary conditions to reach smoothness of shell and destroy convergence of computation process. For this reason the applying of analytical methods may give substantial contribution in development of numerical methods. Thus, the analytical investigations can be used under the assumption that the shell is made of linearly elastic net with rectangular infinitely small cells. In this case and referring to Eq. (27), the potential energy functional U can be written in the form:

$$U = \int_0^H\int_0^{2\pi}\left(k_1\varepsilon_1^2 + k_2\varepsilon_2^2\right)\sqrt{g_{11}^0 g_{22}^0 - g_{12}^0}\,d\varphi d\zeta \quad (45)$$

Where, k_1 and k_2 the coefficients describing elastic properties of the threads that are disposed along coordinate lines and confine meshes of the net.

The limitation of the analysis by axisymmetric problems of interaction between cylindrical shell that has radius R_0 and the solid obtained by the rotation around axis z of line given by the following equation:

$$R(z) = R_0 + \Delta + R_0\mu\cos\frac{\pi z}{2l} \quad (46)$$

where, Δ and l are arbitrary chosen quantities.

Because of axial symmetry the shell angular displacements $\theta(\mu, \varphi, \zeta)$ are zero and all the deformations are defined by axial displacements w, which do not depend on φ, and may be presented as follows:

$$w(\mu, \zeta) = u_0(\zeta) + \mu u(\zeta) + \ldots. \quad (47)$$

At zero and first order approximation of Euler's equation for extreme problem concerning U can be given in the following form [6]:

$$\frac{d^2u_0}{d\zeta^2}=0, \quad \frac{d^2u_1}{d\zeta^2}+\frac{k_2}{k_1}\frac{\pi}{2l}\frac{\Delta}{R_0}\sin\frac{\pi(\zeta+u_0(\zeta))}{2l}=0, \quad .... \qquad (48)$$

The solutions of various boundary values, problems for equations (48) can be obtained easily. For example, the formula for calculation of pressure exerted by shell with free edges on the solid surface can be represented by:

$$q=-\frac{k_2}{R_0}\left(\frac{\Delta}{R_0}\pm\mu\cos\frac{\pi\zeta}{2l}\right) \qquad (49)$$

7. Influence of the Deformation Properties of the Textile Materials

The influence of the deformation properties of the textile materials that are used during the production of composite products is certainly significant but not easy to be taken into account. Now, consider the deformations of structures of reinforcing textile tapes for manufacturing of composite products by winding process, the production of such composite materials shows increased requirements to uniformity of structures of tapes. Heterogeneity of the structures can be developed due to the deformations of winding process. By assuming that the tape has a structure of a plain weave and its basic strings go along a tape and have the visco-elastic properties. The deformations of these strings during winding process can be studied with reference to Figure3. From this figure, V_C is the vertical velocity of the cylinder on which the tape is reeled up, Ω and R are the angular velocity and the radius of the cylinder, ω and r are the angular velocity and the radius of the feeding cylinder; φ is the angle of geodetic lines along which the basic strings are settled down, L is the length of the bottom string part which is located between the cylinders.

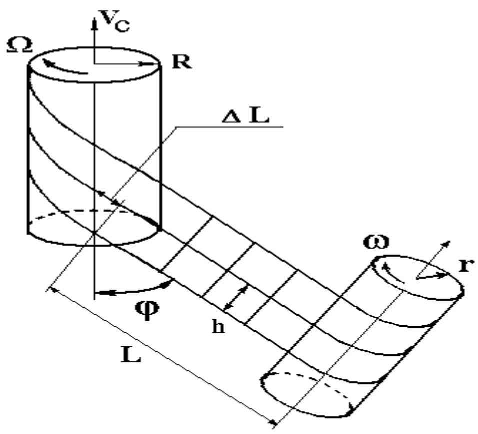

Figure 3. The winding of the tape

By considering that the axis of feeding cylinder is perpendicular to these strings, the following equation for calculation of the tension of string can be applied:

$$T=E\varepsilon_A+\frac{\mu}{L+\Delta L}(1+\varepsilon_A)(V_B-V_A) \qquad (50)$$

Where ε_A deformation of basic strings on the feeding cylinder:

$$V_A=r\omega, \quad V_B=R\Omega/\cos\varphi \qquad (51)$$

By referring to Eq. (50) the tension of strings are non-uniform and depends on their place in a tape and the elimination of this non-uniformity is possible by various methods.

8. Conclusion

1. A mathematical study of the stress-strain curve (behavior) based on the static equilibrium and established equations of membranes were developed to evaluate the problems of the manufacturing of composite materials.
2. The study considered that the little capacity of the layers assumed to be membranes with a small resistance to the bending moments.
3. To predict the changes in the textile structure of the layer materials, the stress-strain behavior of the layers (membranes or soft shells) was investigated.
4. By asymptotic analytical methods of small segment, the strain energy and finite elements methods were used to evaluate the boundary problems and textile structural changes of the layers.
5. A criterion of smoothness of layers was developed and a method of calculating the deformations of the textile structure of the layers was proposed.

References

[1] Bernadou, M., Ciarlet P G, Miara B. Existence theorems for tow-dimensional linear shell theorems. J. Elasticity, Vol. 34, 1994, 111-138.

[2] Zendehudi, G., Kazemi, A., The accuracy of thin-shell in estimation of aneurysm rupture. Journal of Biomechanics, Vol. 40, No. 14, 2007, 3230-3235.

[3] Carnaby, G.A., and Pan, N., Theory of the Compression Hysteresis of Fibrous Assemblies, Textile Res. J., Vol. 59, No. 5, 1989, 275-284.

[4] Berdichevsky, V., Some forms of the equation of shell theory. Soviet Physics-Doklady, Vol. 22, No. 4, 1996, 1-233.

[5] Chaikin, V. A., Applied problems of threads mechanics. Journal of SPSUTD, 2005: 144-148(In Russian).

[6] Pan, N., Development of a Constitutive Theory for Short-fiber Yarns .4. The Mechanics of Blended Fibrous Structures, J. Textile Inst., Vol. 87, No. 3, 1996, 467–483.

[7] Ugural, A. C., Stresses in plates and shell. New York 2nd edn., McGraw-Hill, 1994.

[8] Dneprov, I.V., Ponomarev, A.T., and Radchenko, A.V.: The Stress-Strain State of Soft Shells of Arbitrary Shape. Journal of Mathematical Sciences, Vol. 72, No.5, 1994, 3293-3298.

[9] Schlebusch, R., Zastrau, B., Variational formulation of a three-dimensional surface-related solid-shell finite element. Archive of Applied Mechanics (Ingenierur Archive), 2008: Accepted for publication.

[10] Zienkiewicz, O., Finite Element Method in Engineering Science, McGraw-Hill, New York, 1971

[11] Sheng Zhang, A linear shell theory based on variational principles. Pennsylvania: Pennsylvania state University, 2001.

المملكة الأردنية الهاشمية

الجامعة الهاشمية

المجلة الأردنية
للهندسة الميكانيكية والصناعية

JJMIE

مجلة علمية عالمية محكمة

http://jjmie.hu.edu.jo/

ISSN 1995-6665

المجلة الأردنية للهندسة الميكانيكية والصناعية
مجلة علمية عالمية محكمة

المجلة الأردنية للهندسة الميكانيكية والصناعية: مجلة علمية عالمية محكمة أسستها اللجنة العليا للبحث العلمي، وزارة التعليم العالي والبحث العلمي، الأردن، وتصدر عن عمادة البحث العلمي والدراسات العليا، الجامعة الهاشمية، الزرقاء، الأردن.

ترسل البحوث إلى العنوان التالي :

رئيس تحرير المجلة الأردنية للهندسة الميكانيكية والصناعية
عمادة البحث العلمي والدراسات العليا
الجامعة الهاشمية
الزرقاء - الأردن
هاتف :٠٩٦٢-٠٥-٣٩٠٣٣٣٣ فرعي ٤١٤٧
Email: jjmie@hu.edu.jo
Website: www.jjmie.hu.edu.jo